NANOSCALE IONIC MATERIALS: SYNTHESIS AND PROPERTIES

A Dissertation

Presented to the Faculty of the Graduate School

of Cornell University

In Partial Fulfillment of the Requirements for the Degree of

Doctor of Philosophy

by

Robert Rodriguez

February 2010

NANOSCALE IONIC MATERIALS: SYNTHESIS AND PROPERTIES

Robert Rodriguez, Ph.D.

Cornell University, 2010

Nanoscale Ionic Materials (NIMs) are hybrid organic-inorganic materials which consist of a core nanoparticle, a covalently grafted charged corona, and an associated canopy with a charge opposite that of the canopy. In this thesis the synthesis and properties of NIMs are discussed. NIMs are synthesized by covalently grafting a sulfonic acid terminated silane to the surface of a silica nanoparticle. This sulfonic acid group is then reacted with an amine terminated poly(ethylene glycol) in a simple acid-base reaction. By measuring the titration curve of this reaction the NIMs transition, where there is a one-to-one ratio of sulfonic acid groups to canopy molecules, can be experimentally determined. The effects of core volume fraction and amine topology on the structure and rheology of NIMs is also presented. It is found that NIMs rheology can be tuned to show behavior ranging from simple Newtonian, to non-Newtonian in the form of shear thinning by varying core volume fraction. Upon further analysis, a hypothetical NIMs model is presented and consists of the core, covalently grafted corona, and the associated canopy molecules organizing in layers around each particle. Small-angle x-ray scattering studies reveal that the core microstructure is not the single parameter which is controlling NIMs rheological behavior. These studies instead show that NIMs retain an amorphous structure and that there is a complex interplay between all NIMs components which is controlling the rheological behavior.

BIOGRAPHICAL SKETCH

Robert Rodriguez was born to parents Domingo and Silvia Rodriguez in Hemet, CA on August 12, 1980. After completing high school, he attended the University of California at Riverside (UCR) where he received his B.S. in Physics. During his time at UCR, Robert participated in several outreach programs and undergraduate research where he studied and synthesized magnetic nanoparticles for use in cancer detection. After graduating from UCR, Robert married Ellen Kong who he had met during his undergraduate studies. In 2003, Robert was accepted into the Physics Ph.D. program at Cornell University. After a thorough search for a research group, he decided to join the research group of Prof. Emmanuel P. Giannelis. During his time in the group, Robert focused his studies on the synthesis and development of Nanoscale Ionic Materials. After two years in the Giannelis group, Robert changed fields and joined the Materials Science and Engineering department. During his time at Cornell, Robert has had the privilege of working with several talented scientists and engineers.

To Ellen, Esther, and my parents.

ACKNOWLEDGMENTS

I would like to thank Prof. Emmanuel P. Giannelis and Prof. Lynden A. Archer for their guidance and support. Not only did I learn a great deal from them, but they have also helped me develop my professional career. A special thanks goes to Dr. Rafael Herrera for his patience and training when I first joined the group. I also want to thank my fellow lab mates for their help and support, in particular Dr. Chia-Chen Fang, Dr. Dongyan Wang, Dr. Loan Vo, Dr. Markos Trikeriotis, Dr. Antonios Kelarakis, Dr. Haris Retsos, Luis Estevez, Michelle Wu, Nikhil Fernandes, and the rest of the Giannelis group. I also want to thank Hiroaki Sai, Gilman Toombes, Ruipeng Li, Prof. Aram Amassian, and Prof. Sol Gruner for their assistance with x-ray characterizations. With respect to training on several rheometers, I also want to thank Haibo Qi and Prof. Lynden Archer. I also want to thank the Cornell Center for Materials Research facility managers for their support, in particular Anthony Condo and John Grazul. I also want to thank the entire Nanobiotechnology Center staff, especially Magnus Bergkvist, Teresa Porri, and Penny Burke. I also want to thank the KAUST-CU for funding and the staff: Dr. David Jung, Celia Szczepura, and Angela Yontz.

I have also benefited from the important friendships I have made during my time at Cornell. They helped make graduate school and life in Ithaca a time in my life that I will never forget and will cherish forever. A special thanks also goes to my family for the love and support. Despite the long distance, they always pushed me and helped me succeed. Finally, I want to especially thank my wife, Ellen. Without her support, patience, and love I do not think that I would have made it through graduate school. I want to thank her for putting up with me all these years and for always believing in me.

TABLE OF CONTENTS

LIST OF FIGURES

LIST OF TABLES

INTRODUCTION

Nanoparticles

Nanoparticles have been the focus of intense research in both academia and industry because of the unique properties and features associated with their small sizes. Nanoparticles, with sizes in the range of 1-100nm, lie on scales between atomic and bulk dimensions. Nanoparticles have very large surface areas, and hence, tend to have large surface energies as well[1]. A simple calculation of the specific surface area of a substance illustrates its dependence on size:

$$\begin{aligned} A_{sp} &= \frac{A_{particle}}{M_{particle}} \\ &= \frac{4\pi R^2}{\rho\left({}^{4}/_{3}\right)\pi R^3} \\ A_{sp} &= \frac{3}{\rho R} \end{aligned} \qquad \text{(I.1)}$$

As can be seen from equation (I.1), the surface area of an object is inversely proportional to its radius, so as the dimensions of an object are reduced down to the nanometer size range, its surface to volume ratio significantly increases. This effect results in the majority of the atoms making up the nanoparticle to lie on its surface as opposed to residing in the bulk. Because of this feature, the properties of nanoparticles are dominated by aspects associated with their surface. An example is the color of gold nanoparticles as compared to its appearance in bulk. Bulk gold tends to have a shiny, yellow color, while suspensions of gold nanoparticles can show colors ranging from violet to a red color. This phenomenon is due to the interaction of electromagnetic radiation with the surface of gold nanoparticles producing surface plasmons, an effect called surface plasmon resonance[2, 3].

The discovery of materials with sizes in the nanometer range has fueled intense research on understanding their synthesis and possible applications. Nanostructures of various sizes and morphologies have been synthesized for use in various applications and also because of their interesting scientific potential. A previous editorial reported that more than 14,000 papers on nanoparticles were published in 2007, roughly 200 times the quantity of papers published just 10 years prior[4]. This large wave of publications on the subject has vastly expanded the synthetic methodologies used to produce nanostructured materials. Nanoparticles based on metallic, semiconductor, and magnetic starting materials have been synthesized with a variety of functionalities. The applications for such materials seem limitless and have already found uses in many consumer, industrial, and medical applications. As the field moves forward, the trends that will push forward the research and development of nanostructured materials will be toward finding practical applications and uses for such systems. Nanoscale systems have already become an integral part of everyday living and will continue to define the future possibilities of technological advancements.

The addition of nanoparticles into a polymer matrix (polymer nanocomposites) can greatly enhance the properties, of the host polymer[5-19]. Such promising results have led to a large amount of interest in these systems[6, 8-10, 12-14, 20]. This has been fueled by the promise of unprecedented performance, design flexibility, and lower unit and life-cycle costs. Current market forecasts estimate the use of nanocomposites to reach 100 million pounds in 2011 , at an astonishing annual growth rate of 24%[21]. Another important technological application of nanoparticles has been their use in colloidal suspensions where nanoparticles are dispersed in a liquid. Such suspensions have found many uses such as in paints, toothpaste, inks, coatings, food, and pharmaceutical applications. Such applications require that the materials meet certain requirements, so that there has been a great deal of work to understand the rheological

and microstructural properties of such suspensions and how they affect their possible uses[22-36].

The Structure and Rheology of Colloidal Suspensions

Colloidal systems are by far one of the most heavily studied systems using both rheology[25, 26, 29, 32, 34-67] and various scattering methods[22, 23, 27, 45, 51, 59, 68-102]. The strong emphasis in studying these systems is due to their prevalence in modern society, being important in many applications from construction to healthcare. The rheology of dilute and semidilute suspensions are well understood and were first studied by Einstein and Batchelor[24, 103-105]. Einstein showed that for a dilute dispersion of spheres, the viscosity increase of the system will be in proportion to the volume fraction occupied by the spheres[103],

$$\eta/\mu = 1 + 2.5\varphi \tag{I.2}$$

where η is the viscosity of the suspension, μ is the viscosity of the solvent, and φ is the volume fraction of the spheres. Equation (I.2) shows that the only parameter which determines the viscosity of a suspension of spheres is the volume fraction of the solids; the size of the particles should therefore have no effect. Although this equation appears very simple it is only useful for very dilute concentrations of spheres. For higher concentrations the formula must be modified to take into account the increase in viscosity associated with the changing volume fraction of the particles. The change in viscosity with volume fraction can be written as[106]

$$\delta\eta = \eta 2.5\delta\varphi \tag{I.3}$$

In reality, the viscosity will diverge at a maximum packing fraction, φ_m so equation (I.3) must be modified

(I.4) $$\mathrm{d}\eta = \frac{\eta 2.5\mathrm{d}\varphi}{1 - {\varphi}/{\varphi_m}}$$

where φ_m is the maximum packing fraction of the spheres. Integrating equation (I.4) yields to the Krieger-Dougherty equation

(I.5) $$\eta/\mu = \left(1 - \frac{\varphi}{\varphi_m}\right)^{2.5\varphi_m}.$$

The Krieger-Dougherty equation only adequately describes in the increase in the zero-shear viscosity with volume fraction.

Subsequent experimental studies involving model systems showed that the rheology of colloidal suspensions is quite rich, showing a wide range of non-Newtonian effects such as yield stress, shear thinning and thickening, and even time dependent effects such as thixotropy. For example, Figure I.1 shows features which may be present in the flow curves for suspensions. This figure shows four different regimes which may be present in any system. Whether or not a certain suspension will show these features depends on several parameters to be discussed below. The first region occurs at low shear rates where the viscosity has no dependence on the shear rate. This region is known at the Newtonian part of the curve and the viscosity is called the zero-shear viscosity. The next part of the curve shows the viscosity decreasing with increasing shear rate and is known as shear thinning. Finally, there may also be a region where the viscosity increases with shear rate and is known as shear thickening. Understanding how and why colloidal suspensions show these behaviors is critical for any application.

Past studies have shown that the observed rheology for a colloidal suspension is ultimately determined by the microstructure of the suspension. The microstructure of the suspension is in turn dominated by the types of interactions that exist between

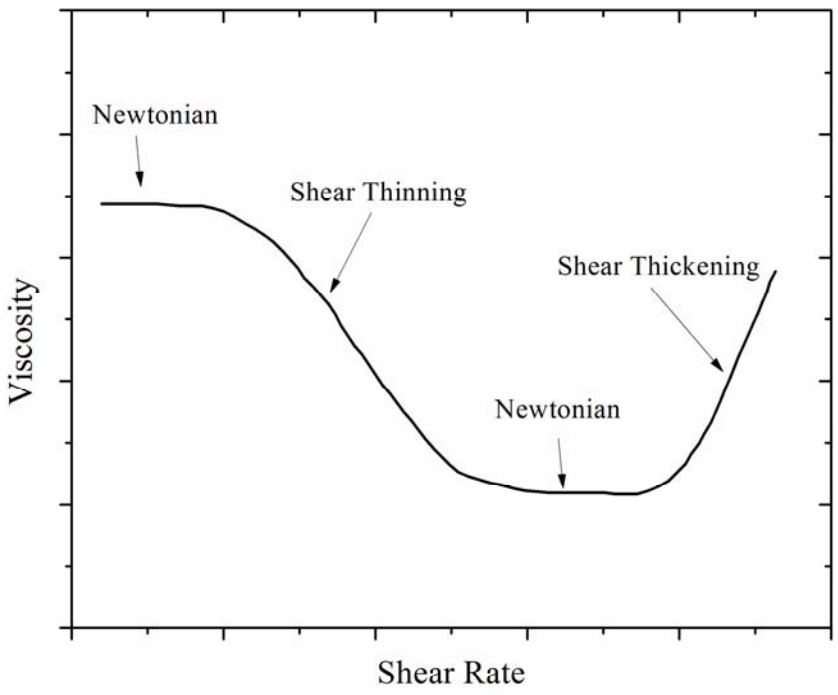

Figure I.1 Diagram of a flow curve showing the different behavior which colloidal suspension display. There are generally three different behaviors, a shear rate independent Newtonian one, and two shear rate dependent regions called shear thinning where the viscosity decreases and shear thickening where the viscosity increases with shear rate.

the colloidal particles. For this reason rheology and scattering studies were combined to study these systems. By understanding the types of interactions that exist between particles, it is then theoretically possible to predict the microstructure of the system and hence the type of observed rheology. In reality, this is a challenging task which is why colloidal systems are still under investigation.

Several studies have shown that the observed rheology can be correlated to the microstructure of the suspension before and during shear[22, 45, 51, 59, 68-70, 76, 80]. For example, at low shear rates, the deformation is not strong enough to perturb the particle structure from its equilibrium organization[107]. As a result, the viscosity does not change with increasing shear rate and it corresponds to the Newtonian region. Many dilute suspensions and semi-dilute suspensions will yield a shear rate independent viscosity at low shear rates. Shear thinning can also be correlated to the microstructure of the particles with both simulations and experiments showing the formation of a different structure amongst the particles during shear[22, 45, 51, 59, 69]. In all these experimental studies and simulations, it is observed that the particles organize into lines parallel to the flow direction. Scattering studies on planes perpendicular to these lines show that the particles form a regular hexagonal lattice, allowing the different layers to easily slide past one another, thereby reducing the resistance to flow and hence, the viscosity, resulting in shear thinning[22, 32, 108]. Simulations and scattering studies have also shown that shear thickening is the result of a different type of structure in the suspension. At large shear rates and high particle volume fractions, it has been shown that particles can actually be driven together to form dynamic clusters which result in observed increases in the viscosity[32, 109].

In all these studies it has been shown that the observed rheology of a colloidal suspension is directly related to the microstructure of the suspension. The microstructure, in turn is related to the interactions that exist between the colloidal

particles themselves. The strength and range of interactions between the particles depends on several parameters such as the chemical composition of the particles, the suspending medium, and the surface chemistry of the particles themselves. A great deal of work has focused on model systems of hard sphere colloidal suspensions where no interaction exists except an infinite repulsion upon contact. The only parameter which determines the microstructure and rheology of hard spheres is their volume fraction while in suspension. This simple system was the subject of a great deal of experimental and theoretical work, since the hard sphere potential can be solved analytically to obtain theoretical structure factors and their rheological response simulated through Brownian dynamics simulations[22, 26, 30, 32-35, 38, 40, 42-46, 52-55, 81, 110-113]. On the other end hard spheres, which have very short range interactions, are charged colloids. Charged suspensions can have very long-range interactions that can be manipulated by varying the ionic strength of the solution. Because the strength and range of interactions strongly depend on the solution and ions present, charged colloidal suspensions cannot be considered as model systems. Despite this challenge, their microstructure and rheology can be tuned by varying the chemistry of the particles themselves and the ions present in solution. Because charged colloidal suspensions are characterized by longer-range interactions, it has been observed that these systems can display non-Newtonian rheology at lower volume fractions than that observed for hard spheres[29, 58, 95, 114-117]. The structure and rheology of colloidal suspension are two features which are intimately related, where one can affect the other. This brief summary is only a small fraction of the current and past work on the subject. These systems are still of great interest and the focus of a great deal of research around the world as they are important in our everyday lives. Chapters 2 and 3 of this thesis focus on the rheology and structure of a new set of fluids composed of charged nanoparticles, called Nanoscale Ionic Materials (NIMs).

Nanoscale Ionic Materials

NIMs are organic-inorganic hybrids typically composed of a nanometer sized core, surface functionalized with a charged corona. An oppositely charged canopy consisting of a low molecular weight polymer is introduced to balance the charge[118, 119]. Because of the hybrid character of NIMs, their physical properties can be tailored by varying the size, shape and composition of the core, corona, and canopy as well as external parameters such as temperature, mechanical deformation, electric and magnetic fields. For example, previous work at Cornell has shown that by varying the molecular weight and grafting density of the canopy, materials which can range in flow properties from liquid-like to waxy solids can be synthesized[120, 121]. The canopy, which serves as the effective fluidization medium in NIMs, is tethered to the cores by ionic bonds leading to a low vapor pressure and yielding low VOC fluids with an unusual combination of properties.

The first example of NIMs, called the first generation of NIMs, involved covalently grafting a cationic amine such as $(CH_3O)_3Si(CH_2)_3N^+(CH_3)(C_{10}H_{21})_2Cl^-$ to the surface of the nanoparticle core, resulting in a positively charged corona around the core particle[118, 120-125]. To maintain charge neutrality, a counter-ion must always be present. If the counter anion is Cl^-, solid powders are obtained with no phase transitions observed even when the material is heated to temperatures above the decomposition temperature of the corona. Exchanging the Cl^- ions with a larger organic counter-ion such as $R(OCH_2CH_2)_7O(CH_2)_3SO^-_3$ (R = alkyl chain) or any other appropriate anionic oligomer results in liquid-like materials which can flow at room temperature.

This thesis will focus on the second generation of NIMs, which involves a complementary approach, where the sign of the charges on the corona and canopy is opposite to that of first generation systems. Core particles are surface modified by

covalently grafting 3-(trihydroxysilyl)-1-propane sulfonic acid (SIT), resulting in a net negative charge on the surface[119]. A proton is present to maintain the charge neutrality of the system. As was observed in the first generation NIMs, these particles appear as powders and show no visible fluid behavior in the absence of a solvent. These acidic particles are then reacted with a PEG-substituted amine in a simple acid-base reaction. During the reaction, the acidic groups on the cores protonate the amine on the canopy leading to opposite charges on the corona and canopy and an electrostatic interaction between the two, which has the effect of stabilizing the particles.

This thesis will focus on a system which consists of silica as the core particle, but the NIMs platform can be extended beyond a simple oxide as the core. Previous work based on other cores will be presented below to show the generality of this approach. One of the original materials previously published involved iron oxide as the core, which provided the first example of a magnetically responsive NIMs system, where the iron oxide cores retain their super paramagnetic nature[118]. This approach has also been applied to a class of protonic solid conductors called polyoxometalates (POMs)[124] where POMs consist of nanometer sized clusters of early transition metal ions octahedrally coordinated to oxygen[126]. POMs have been considered as potential candidates for electrolytes in fuel cell applications[127-132]. NIMs based on POMs as their cores were obtained by a partial exchange of the surface protons in the core cluster by PEG-containing quaternary ammonium cation[124]. This reaction formed fluid proton conductors with conductivities about 3-4 orders of magnitude higher than their solid-state analogs. Additionally, by applying the Walden rule, $\Lambda\eta$ = constant, where Λ is the equivalent conductivity and η is the viscosity of the liquid[133, 134], it was found that POM-based NIMs behave like super-ionic liquids with more efficient conduction mechanisms such as superionic slip of ions or the Grothhus mechanism.

NIMs based on other oxide cores, including TiO_2[120], ZnO[125] nanoparticles and even layered organosilicate nanoparticles[121], have been reported. An interesting feature manifested by NIMs based on ZnO is their high quantum yield photoluminescence, a property that holds promise for nanoscale hybrid materials in optics and photonics. It may even be possible to dope with different chemical species to tune the emission towards the UV, opening up the possibility for lasing in ZnO nanoparticles.

The first case of a solvent-free plasmonic fluid was reported by synthesizing NIMs with metal cores, such as gold nanorods (GNRs)[135]. The localized surface plasmon resonance (LSPR) of metal nanoparticles is highly sensitive to the local environment of nanoparticles and to interparticle interactions. Interesting features manifested by plasmonic fluids containing GNR clusters include the reversible color changes and plasmonic responses of the fluid in response to external stimuli such as mechanical shearing. NIMs based on other metal cores such as Pt and Pd have also been reported[136].

Previous work has also shown that NIMs based organic cores are possible. Meltable, amphiphilic NIMs based on carbon nanotubes were synthesized using a two step process where first, the nanotubes are acid oxidized to create polar hydrophilic groups (-COOH) then reacted with a poly(ethylene glycol)- substituted tertiary amine[122]. The resulting material is solid at room temperature but undergoes a solid-liquid transition at 35°C and is dispersible in both organic and aqueous solvents. Biological molecules are also possible cores for NIMs. In one example, fluid DNA was be synthesized in the absence of any solvents by replacing the sodium counter-ions of DNA with a quaternary ammonium[120]. A recent report by Perriman et. al. shows the first example of a solvent-free liquid protein based on a ferritin-polymer construct[137]. In this work, cationic ferritin was electrostatically bound with a

stoichiometric amount of anionic polymer surfactant to produce a single component liquid protein nanostructure. These examples show that NIMs are not limited to inorganic cores, but can be synthesized using various organic, biological and hybrid compositions. The versatility of the chemistry therefore allows the synthesis of materials with a variety of compositions and properties, opening several new avenues of research and potential applications.

This thesis is divided into three chapters. The first chapter will discuss the synthesis of second generation NIMs and locating the NIMs transition where there is a one-to-one correspondence of surface charged groups to counterions. The second chapter will focus on the rheology of NIMs. In it, the effects of canopy architecture and core volume fraction will be presented. NIMs scattering studies will presented in the final chapter and combined with the observed rheology. Using the information from these two methods, a hypothesis will be developed and presented in an attempt to correlate the observed rheological and structural behavior of NIMs.

REFERENCES

[1] P. C. Hiemenz, R. Rajagopalan, *Principles of colloid and surface chemistry*, Marcel Dekker, Inc, New York **1997**.

[2] J. M. Pitarke, V. M. Silkin, E. V. Chulkov, P. M. Echenique, *Rep. Prog. Phys.* **2007**, *70*, 1.

[3] B. Schaffer, K. Riegler, G. Kothleitner, W. Grogger, F. Hofer, *Micron* **2009**, *40*, 269.

[4] N. A. Kotov, F. Stellacci, *Adv. Mater.* **2008**, *20*, 4221.

[5] E. P. Giannelis, *Adv. Mater.* **1996**, *8*, 29.

[6] E. P. Giannelis, *Appl. Organomet. Chem.* **1998**, *12*, 675.

[7] S. N. Bhattacharya, M. R. Kamal, R. K. Gupta, *Polymeric nanocomposites: theory and practice*, Carl Hanser Verlag, Munich **2008**.

[8] R. Gangopadhyay, A. De, *Chem. Mat.* **2000**, *12*, 608.

[9] F. Hussain, M. Hojjati, M. Okamoto, R. E. Gorga, *J. Compos Mater.* **2006**, *40*, 1511.

[10] J. Jordan, K. I. Jacob, R. Tannenbaum, M. A. Sharaf, I. Jasiuk, *Mater. Sci. Eng. A-Struct. Mater. Prop. Microstruct. Process.* **2005**, *393*, 1.

[11] T. Kairn, P. J. Daivis, I. Ivanov, S. N. Bhattacharya, *J. Chem. Phys.* **2005**, *123*, 7.

[12] R. Krishnamoorti, R. A. Vaia, E. P. Giannelis, *Chem. Mat.* **1996**, *8*, 1728.

[13] E. Manias, A. Touny, L. Wu, K. Strawhecker, B. Lu, T. C. Chung, *Chem. Mat.* **2001**, *13*, 3516.

[14] S. S. Ray, M. Okamoto, *Prog. Polym. Sci.* **2003**, *28*, 1539.

[15] K. Park, R. A. Vaia, *Adv. Mater.* **2008**, *20*, 3882.

[16] F. M. Du, R. C. Scogna, W. Zhou, S. Brand, J. E. Fischer, K. I. Winey, *Macromolecules* **2004**, *37*, 9048.

[17] J. W. Gilman, *Applied Clay Science* **1999**, *15*, 31.

[18] J. W. Gilman, C. L. Jackson, A. B. Morgan, R. Harris, E. Manias, E. P. Giannelis, M. Wuthenow, D. Hilton, S. H. Phillips, *Chem. Mat.* **2000**, *12*, 1866.

[19] B. Serge, B. Michel Le, D. François, W. G. Jeffrey, K. Takashi, *Fire and Materials* **2000**, *24*, 201.

[20] R. Krishnamoorti, R. A. Vaia, *J. Polym. Sci. Pt. B-Polym. Phys.* **2007**, *45*, 3252.

[21] K. I. Winey, R. A. Vaia, *Mrs Bulletin* **2007**, *32*, 314.

[22] B. J. Ackerson, P. N. Pusey, *Phys Rev Lett* **1988**, *61*, 1033.

[23] M. Ballauff, *Curr Opin Colloid In* **2001**, *6*, 132.

[24] G. K. Batchelor, *J. Fluid Mech.* **1977**, *83*, 97.

[25] J. Bergenholtz, J. F. Brady, M. Vicic, *J. Fluid Mech.* **2002**, *456*, 239.

[26] J. F. Brady, *Journal of Chemical Physics* **1993**, *99*, 567.

[27] M. Chen, W. B. Russel, *J Colloid Interf Sci* **1991**, *141*, 564.

[28] J. K. G. Dhont, G. Nagele, *Phys. Rev. E* **1998**, *58*, 7710.

[29] M. E. Fagan, C. F. Zukoski, *J. Rheol.* **1997**, *41*, 373.

[30] D. R. Foss, J. F. Brady, *J. Rheol.* **2000**, *44*, 629.

[31] H. M. Lindsay, P. M. Chaikin, *Journal of Chemical Physics* **1982**, *76*, 3774.

[32] T. N. Phung, J. F. Brady, G. Bossis, *J. Fluid Mech.* **1996**, *313*, 181.

[33] T. Shikata, D. S. Pearson, *J. Rheol.* **1994**, *38*, 601.

[34] J. C. Vanderwerff, C. G. Dekruif, *J. Rheol.* **1989**, *33*, 421.

[35] J. C. Vanderwerff, C. G. Dekruif, C. Blom, J. Mellema, *Physical Review A* **1989**, *39*, 795.

[36] H. Watanabe, M. L. Yao, K. Osaki, T. Shikata, H. Niwa, Y. Morishima, *Rheol. Acta* **1997**, *36*, 524.

[37] H. A. Baghdadi, H. Sardinha, S. R. Bhatia, *J. Polym. Sci. Pt. B-Polym. Phys.* **2005**, *43*, 233.

[38] J. Bergenholtz, *Curr. Opin. Colloid Interface Sci.* **2001**, *6*, 484.

[39] G. Bossis, J. F. Brady, *Journal of Chemical Physics* **1987**, *87*, 5437.

[40] G. Bossis, J. F. Brady, *Journal of Chemical Physics* **1989**, *91*, 1866.

[41] J. F. Brady, *Journal of Chemical Physics* **1993**, *98*, 3335.

[42] J. F. Brady, *Curr. Opin. Colloid Interface Sci.* **1996**, *1*, 472.

[43] J. F. Brady, *Chemical Engineering Science* **2001**, *56*, 2921.

[44] J. F. Brady, A. S. Khair, M. Swaroop, *J. Fluid Mech.* **2006**, *554*, 109.

[45] J. F. Brady, J. F. Morris, *J. Fluid Mech.* **1997**, *348*, 103.

[46] J. F. Brady, M. Vicic, *J. Rheol.* **1995**, *39*, 545.

[47] R. Buscall, *Journal of the Chemical Society-Faraday Transactions* **1991**, *87*, 1365.

[48] R. Buscall, J. I. Mcgowan, A. J. Mortonjones, *J. Rheol.* **1993**, *37*, 621.

[49] L. B. Chen, B. J. Ackerson, C. F. Zukoski, *J. Rheol.* **1994**, *38*, 193.

[50] L. B. Chen, M. K. Chow, B. J. Ackerson, C. F. Zukoski, *Langmuir* **1994**, *10*, 2817.

[51] L. B. Chen, C. F. Zukoski, B. J. Ackerson, H. J. M. Hanley, G. C. Straty, J. Barker, C. J. Glinka, *Phys Rev Lett* **1992**, *69*, 688.

[52] E. G. D. Cohen, R. Verberg, I. M. de Schepper, *Physica a-Statistical Mechanics and Its Applications* **1998**, *251*, 251.

[53] I. M. Deschepper, H. E. Smorenburg, E. G. D. Cohen, *Phys. Rev. Lett.* **1993**, *70*, 2178.

[54] J. Mellema, *Curr. Opin. Colloid Interface Sci.* **1997**, *2*, 411.

[55] J. Mellema, C. G. Dekruif, C. Blom, A. Vrij, *Rheol. Acta* **1987**, *26*, 40.

[56] J. Mewis, W. J. Frith, T. A. Strivens, W. B. Russel, *Aiche J.* **1989**, *35*, 415.

[57] J. Mewis, J. Vermant, *Progress in Organic Coatings* **2000**, *40*, 111.

[58] W. B. Russel, *J. Fluid Mech.* **1978**, *85*, 209.

[59] A. Sierou, J. F. Brady, *J Rheol* **2002**, *46*, 1031.

[60] J. J. Stickel, R. L. Powell, *Annual Review of Fluid Mechanics* **2005**, *37*, 129.

[61] B. Vandervorst, D. Vandenende, J. Mellema, *J. Rheol.* **1995**, *39*, 1183.

[62] R. Verberg, I. M. deSchepper, E. G. D. Cohen, *Phys. Rev. E* **1997**, *55*, 3143.

[63] K. Vondermassen, J. Bongers, A. Mueller, H. Versmold, *Langmuir* **1994**, *10*, 1351.

[64] H. Watanabe, M. L. Yao, K. Osaki, T. Shikata, H. Niwa, Y. Morishima, *Rheol. Acta* **1999**, *38*, 2.

[65] H. Watanabe, M. L. Yao, K. Osaki, T. Shikata, H. Niwa, Y. Morishima, N. P. Balsara, H. Wang, *Rheol. Acta* **1998**, *37*, 1.

[66] H. Watanabe, M. L. Yao, A. Yamagishi, K. Osaki, T. Shitata, H. Niwa, Y. Morishima, *Rheol. Acta* **1996**, *35*, 433.

[67] A. T. J. M. Woutersen, C. G. Dekruif, *Journal of Chemical Physics* **1991**, *94*, 5739.

[68] B. J. Ackerson, N. A. Clark, *Phys. Rev. A* **1984**, *30*, 906.

[69] B. J. Ackerson, J. B. Hayter, N. A. Clark, L. Cotter, *J Chem Phys* **1986**, *84*, 2344.

[70] Z. Adamczyk, B. Jachimska, M. Kolasinska, *J Colloid Interf Sci* **2004**, *273*, 668.

[71] N. W. Ashcroft, J. Lekner, *Phys Rev* **1966**, *145*, 83.

[72] C. G. Dekruif, W. J. Briels, R. P. May, A. Vrij, *Langmuir* **1988**, *4*, 668.

[73] L. A. Feigin, D. I. Svergun, *Structure Analysis by Small-Angle X-Ray and Neutron Scattering*, Plenum Press, New York **1986**.

[74] U. Gasser, E. R. Weeks, A. Schofield, P. N. Pusey, D. A. Weitz, *Science* **2001**, *292*, 258.

[75] W. L. Griffith, R. Triolo, A. L. Compere, *Phys. Rev. A* **1987**, *35*, 2200.

[76] M. D. Haw, W. C. K. Poon, P. N. Pusey, *Phys Rev E* **1998**, *57*, 6859.

[77] E. W. Kaler, *Modern Aspects of Small-Angle Scattering*, Kluwer Academic, Boston **1993**.

[78] W. K. Kegel, A. van Blaaderen, *Science* **2000**, *287*, 290.

[79] S. R. Kline, *J. Appl. Crystallogr.* **2006**, *39*, 895.

[80] H. M. Laun, R. Bung, S. Hess, W. Loose, O. Hess, K. Hahn, E. Hadicke, R. Hingmann, F. Schmidt, P. Lindner, *J Rheol* **1992**, *36*, 743.

[81] D. A. McQuarrie, *Statistical Mechanics*, Harper & Row, New York **1975**.

[82] M. Megens, C. M. vanKats, P. Bosecke, W. L. Vos, *Langmuir* **1997**, *13*, 6120.

[83] J. Moonen, C. Dekruif, A. Vrij, *Colloid Polym Sci* **1988**, *266*, 1068.

[84] J. Moonen, A. Vrij, *Colloid Polym Sci* **1988**, *266*, 1140.

[85] R. H. Ottewill, A. R. Rennie, G. D. W. Johnson, *Adv Colloid Interfac* **2003**, *100*, 585.

[86] R. H. Ottewill, R. A. Richardson, *Colloid Polym Sci* **1982**, *260*, 708.

[87] D. Pontoni, S. Finet, T. Narayanan, A. R. Rennie, *J Chem Phys* **2003**, *119*, 6157.

[88] W. Poon, *Science* **2004**, *304*, 830.

[89] P. N. Pusey, P. N. Segre, O. P. Behrend, S. P. Meeker, W. C. K. Poon, *Physica A* **1997**, *235*, 1.

[90] D. Qiu, T. Cosgrove, A. M. Howe, *Langmuir* **2006**, *22*, 6060.

[91] D. Qiu, T. Cosgrove, A. M. Howe, U. A. Dreiss, *Langmuir* **2006**, *22*, 546.

[92] D. Qiu, C. A. Dreiss, T. Cosgrove, A. M. Howe, *Langmuir* **2005**, *21*, 9964.

[93] S. K. Rhodes, J. A. Lewis, *J Am Ceram Soc* **2006**, *89*, 1840.

[94] D. O. Riese, G. H. Wegdam, W. L. Vos, R. Sprik, D. Fenistein, J. H. H. Bongaerts, G. Grubel, *Phys Rev Lett* **2000**, *85*, 5460.

[95] E. B. Sirota, H. D. Ouyang, S. K. Sinha, P. M. Chaikin, J. D. Axe, Y. Fujii, *Phys Rev Lett* **1989**, *62*, 1524.

[96] P. Vanbeurten, A. Vrij, *J Chem Phys* **1981**, *74*, 2744.

[97] A. Vanblaaderen, P. Wiltzius, *Science* **1995**, *270*, 1177.

[98] W. Vanmegen, P. N. Pusey, *Phys. Rev. A* **1991**, *43*, 5429.

[99] N. J. Wagner, R. Krause, A. R. Rennie, B. D'Aguanno, J. Goodwin, *The Journal of Chemical Physics* **1991**, *95*, 494.

[100] A. Weiss, N. Dingenouts, M. Ballauff, H. Senff, W. Richtering, *Langmuir* **1998**, *14*, 5083.

[101] M. Zackrisson, A. Stradner, P. Schurtenberger, J. Bergenholtz, *Langmuir* **2005**, *21*, 10835.

[102] M. Zackrisson, A. Stradner, P. Schurtenberger, J. Bergenholtz, *Phys Rev E* **2006**, *73*, 8.

[103] A. Einstein, *Investigations on the Theory of the Brownian Movement*, Dover Publications, New York **1956**.

[104] Batchelo.Gk, *J. Fluid Mech.* **1970**, *41*, 545.

[105] Batchelo.Gk, J. T. Green, *J. Fluid Mech.* **1972**, *56*, 401.

[106] R. J. Hunter, *Introduction to Modern Colloid Science*, Oxford University Press, New York **1993**.

[107] R. G. Larson, *The Structure and Rheology of Complex Fluids*, Oxford University Press, New York **1999**.

[108] P. N. Pusey, W. Vanmegen, *Phys. Rev. Lett.* **1987**, *59*, 2083.

[109] P. Dhaene, J. Mewis, G. G. Fuller, *J. Colloid Interface Sci.* **1993**, *156*, 350.

[110] D. R. Foss, J. F. Brady, *J. Fluid Mech.* **2000**, *407*, 167.

[111] J.-P. Hansen, I. R. McDonald, *Theory of Simple Liquids*, Academic Press, New York **2006**.

[112] S. E. Phan, W. B. Russel, Z. D. Cheng, J. X. Zhu, P. M. Chaikin, J. H. Dunsmuir, R. H. Ottewill, *Phys. Rev. E* **1996**, *54*, 6633.

[113] P. N. Segre, S. P. Meeker, P. N. Pusey, W. C. K. Poon, *Phys. Rev. Lett.* **1995**, *75*, 958.

[114] B. Beresfordsmith, D. Y. C. Chan, *Faraday Discussions* **1983**, 65.

[115] G. Fritz, V. Schadler, N. Willenbacher, N. J. Wagner, *Langmuir* **2002**, *18*, 6381.

[116] G. Nagele, *Physics Reports-Review Section of Physics Letters* **1996**, *272*, 216.

[117] J. Z. Wu, D. Bratko, J. M. Prausnitz, *Proceedings of the National Academy of Sciences of the United States of America* **1998**, *95*, 15169.

[118] A. B. Bourlinos, R. Herrera, N. Chalkias, D. D. Jiang, Q. Zhang, L. A. Archer, E. P. Giannelis, *Adv. Mater.* **2005**, *17*, 234.

[119] R. Rodriguez, R. Herrera, L. A. Archer, E. P. Giannelis, *Adv. Mater.* **2008**, *20*, 4353.

[120] A. B. Bourlinos, S. R. Chowdhury, R. Herrera, D. D. Jiang, Q. Zhang, L. A. Archer, E. P. Giannelis, *Advanced Functional Materials* **2005**, *15*, 1285.

[121] A. B. Bourlinos, S. R. Chowdhury, D. D. Jiang, Y. U. An, Q. Zhang, L. A. Archer, E. R. Giannelis, *Small* **2005**, *1*, 80.

[122] A. B. Bourlinos, V. Georgakilas, V. Tzitzios, N. Boukos, R. Herrera, E. R. Giannelis, *Small* **2006**, *2*, 1188.

[123] A. B. Bourlinos, E. P. Giannelis, Q. Zhang, L. A. Archer, G. Floudas, G. Fytas, *European Physical Journal E* **2006**, *20*, 109.

[124] A. B. Bourlinos, K. Raman, R. Herrera, Q. Zhang, L. A. Archer, E. P. Giannelis, *Journal of the American Chemical Society* **2004**, *126*, 15358.

[125] A. B. Bourlinos, A. Stassinopoulos, D. Anglos, R. Herrera, S. H. Anastasiadis, D. Petridis, E. P. Giannelis, *Small* **2006**, *2*, 513.

[126] D. E. Katsoulis, *Chem. Rev.* **1998**, *98*, 359.

[127] Q. F. Li, R. H. He, J. O. Jensen, N. J. Bjerrum, *Chem Mater* **2003**, *15*, 4896.

[128] S. M. Haile, D. A. Boysen, C. R. I. Chisholm, R. B. Merle, *Nature* **2001**, *410*, 910.

[129] Y. S. Kim, F. Wang, M. Hickner, T. A. Zawodzinski, J. E. McGrath, *J. Membr. Sci.* **2003**, *212*, 263.

[130] O. Nakamura, I. Ogino, T. Kodama, *Solid State Ion.* **1981**, *3-4*, 347.

[131] A. J. Appleby, "FUEL-CELL ELECTROLYTES - EVOLUTION, PROPERTIES AND FUTURE-PROSPECTS", **1994**.

[132] M. Susan, A. Noda, S. Mitsushima, M. Watanabe, *Chem. Commun.* **2003**, 938.

[133] W. Xu, C. A. Angell, *Science* **2003**, *302*, 422.

[134] W. Xu, E. I. Cooper, C. A. Angell, *J. Phys. Chem. B* **2003**, *107*, 6170.

[135] R. R. Bhattacharjee, R. Li, L. Estevez, D.-M. Smilgies, A. Amassian, E. P. Giannelis, *J. Mater. Chem.* **2009**.

[136] S. C. Warren, M. J. Banholzer, L. S. Slaughter, E. P. Giannelis, F. J. DiSalvo, U. B. Wiesner, *Journal of the American Chemical Society* **2006**, *128*, 12074.

[137] A. W. Perriman, H. Colfen, R. W. Hughes, C. L. Barrie, S. Mann, *Angew. Chem.-Int. Edit.* **2009**, *48*, 6242.

CHAPTER 1: NIMs SYNTHESIS AND THE NIMs TRANSITION

Introduction

Use of nanoparticles in many applications requires careful manipulation of the interparticle interactions to prevent aggregation. How the interparticle interactions are modified strongly depend on the suspending medium used. For example, a suspension of nanoparticles in an aqueous solvent will only be stable, if the particles are modified with a hydrophilic group such as an acid or polymer chain such as polyethylene oxide, or imparting the particles with a net charge so as to repel each other in solution[1, 2]. To suspend nanoparticles in organic solvents requires a hydrophobic functionality, such as the long alkyl chains used to disperse silica in solvents such as hexanes[3]. There is a great deal of literature studying the effects of interparticle interactions on the stability of particles in a solvent and how they affect the rheology[1, 2, 4-38] and structure of such materials[4-7, 16, 22, 35, 37, 39-71]. The key in any application that requires monodisperse particles is to compatibalize the nanoparticles with its surroundings as opposed to with themselves. This leads to attractive interactions between the particle surface and the suspending medium to dominate over attractive interactions between the nanoparticles themselves, thereby preventing aggregation of the particles and hence, a phase separation where the particles actually come out of the suspending medium.

The literature is full of examples for dispersing nanoparticles in almost any desired matrix[72-83]. Whether the particles are modified during the synthesis or afterwards, they all involve some type of surface modification. Depending on the material used to synthesize the nanoparticles, different types of chemical bonds will be used to graft the modifying agent to the nanoparticle surface. For example, gold nanoparticles and systems based on semiconductors require a thiol capping agent[84, 85].

The main drawback of all these systems is the requirement of a stable fluid phase. If the suspending medium of a suspension of nanoparticles is dried out, only a dry powder of nanoparticles will remain. This has the potential of becoming a health hazard for particles with diameters less than 100nm since they can easily aerosolize and be inhaled which may lead to respiratory and other related health problems. Another key to stability is the concentration at which particles can be loaded into a medium, after some maximum amount, there will be a phase separation with the particles falling out of the suspension. For almost any application involving nanoparticles to be feasible, the nanoparticles must remain stable, without the particles aggregating while in the fluid matrix.

One way to overcome such difficulties was introduced by Bourlinos et. al. using a materials platform called nanoscale ionic materials (NIMs)[79, 80]. As discussed in Introduction, NIMs are organic-inorganic nanohybrids composed of three constituents: (1) the core nanoparticle, (2) the charged corona, and (3) the canopy. Figure 1.1a shows a schematic of the procedure used to synthesize first generation NIMs. The cores used for the original work consisted of SiO_2 and γ-Fe_2O_3 nanoparticles. As shown in Figure 1.1a, the surface of the nanoparticles are first modified by covalently grafting a cationic organosilane consisting of a propyl quaternary ammonium salt, thereby serving as the corona on the nanoparticles. Grafting this silane renders the nanoparticles cationic with a small Cl^- counter-ion present to balance the charge now on the surface. NIMs are readily obtained by ion-exchanging the Cl^- anion for a larger, bulky counter-ion to serve as the canopy, as shown in Figure 1.1b. For this original work two anionic canopy materials were selected, the first consisted of a poly(ethylene) glycol (PEG) substituted sulfonate counter-ion ($R(OCH_2CH_2)_7O(CH_2)_3SO_3H$, R=alkyl chain) and the second was an

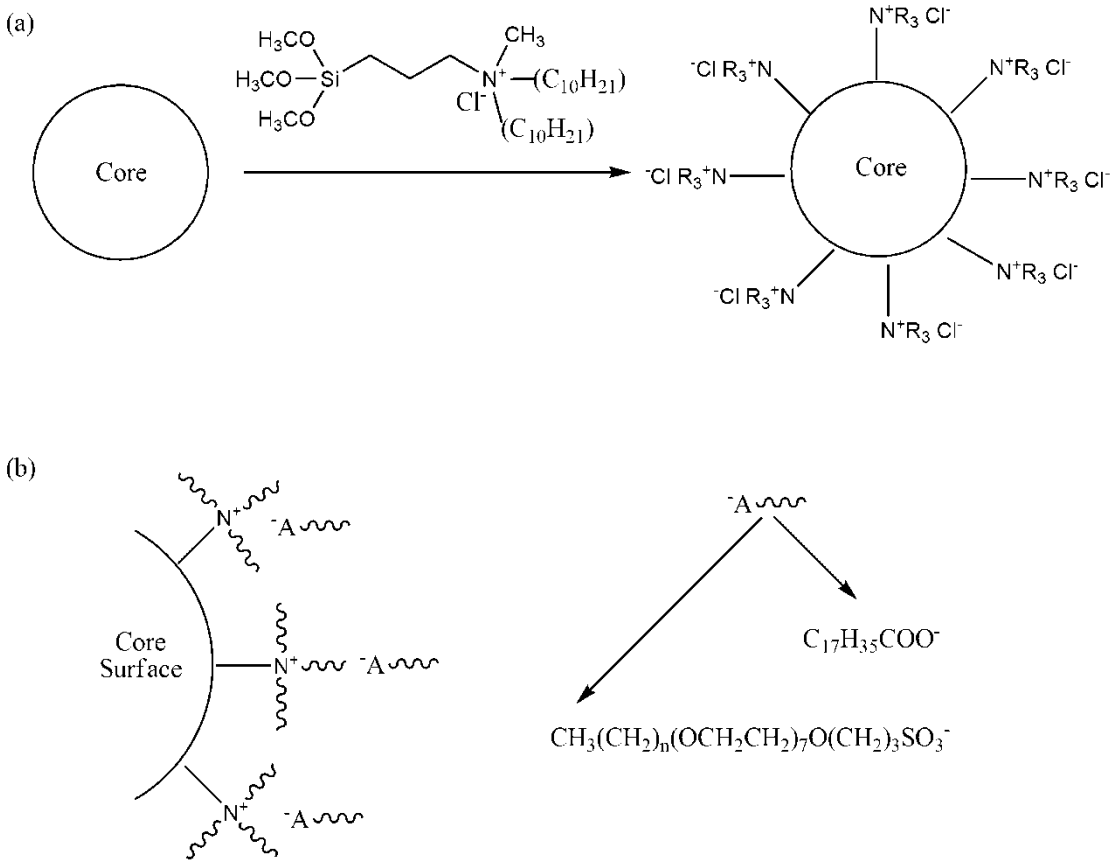

Figure 1.1 Schematic showing synthesis of first generation NIMs. (a) The nanoparticles are first surface functionalized by covalently grafting a cationic organosilane. Cl- ions serve as the counter-ion to positively charged quaternary ammonium. (b) The Cl- ions are exchanged with a larger organic anion. Two different anions were used in the first generation NIMs were used, an isostearate ($C_{17}H_{35}COOH$) and sulfonic ($R(OCH_2CH_2)_7O(CH_2)_3SO_3H$, R=alkyl chain).

isostearate counter-ion ($C_{17}H_{35}COOH$). Using this procedure, the first example of a solvent-free nanoparticle fluid was synthesized where the material flowed without the need of a solvent.

A complementary approach called second generation NIMs is presented in this chapter. This second generation NIMs approach involves changing the sign of the charge on the corona and canopy. The new method results in an acid-base neutralization reaction to create an ionic attraction between the charged corona on the nanoparticle surface and the associated counter-ions. A few advantages of this new approach over the first generation method are the ease with which the core volume fraction and canopy composition can be varied to prepare a broad range of NIMs compositions and properties.

Experimental

NIMs Synthesis

Figure 1.2a shows that in the first step the core nanoparticles are modified by the reaction with 3-(trihydroxylsilyl)-1-propane sulfonic acid (SIT, 40 wt. %, Gelest), giving the particles a negatively charged sulfonic acid group and thereby forming the corona[86]. During this first stage of the synthesis, the nanoparticle solution (Ludox colloidal silica HS30, Sigma Aldrich) was diluted with deionized water to a concentration of 3.0% wt/wt. In a separate flask, 3-(trihydroxylsilyl)-1-propane sulfonic acid (Gelest) was diluted with deionized water to a concentration of 5% wt/wt, where a 10x molar excess of the silane was used for the reaction. The diluted silica suspension was added dropwise to the SIT solution while vigorously stirring. To this mixture, a solution of sodium hydroxide (NaOH, 1M, Sigma Aldrich) was added dropwise until the reaction pH was about 5. The entire solution was then heated to 70°C and stirred vigorously for 24h. Upon completion of the reaction, the solution

was allowed to cool to room temperature. The solution was then placed into Spectra/Por 14kD dialysis membranes (Spectrum Labs) and dialyzed against deionized water for three days to remove any remaining salts and unreacted silane molecules. The water was replaced every 12h during the dialysis to maintain a concentration gradient across the membrane and ensure removal of any undesired species. After dialyzing the suspension, the nanoparticles were then run through an ion exchange column packed with Dowex HCR-W2 ion exchange resin (Sigma Aldrich) to remove the Na^+ ions and protonate the sulfonic acid groups. Upon completion of this last step, the pH of the modified nanoparticle solution was decreased from about pH = 5 down to pH = 1.8. In the final step, the sulfonic acid groups present on the nanoparticle surface are then reacted with an amine which serves as the canopy (Figure 1.2b). Two amine architectures are used for this study, the first is a primary amine (Huntsman, Jeffamine®, $NH_2(CH_2CH_2O)_nCH_3$) and the second is a a tertiary amine (Akzo Nobel, Ethomeen® C/25, $(C_{18}H_{37})N[(CH_2CH_20)_mH][(CH_2CH_2O)_nH]$, $m + n = 25$). The amine molecules are first dispersed in deionized water at a concentration of 5% wt/wt and are then added dropwise to the solution of acidic nanoparticles. This step involves and acid-base neutralization reaction where the sulfonic acid groups protonate the amines, resulting in a negative charge on the corona molecules and a positive charge on the amine: $R'SO_3H + NH_2R \rightarrow R'SO_3^-NH_3^+R$. These opposite charges lead to an ionic attraction between the corona and canopy groups, thereby stabilizing the system.Once the acid and amine groups have reacted, the water was slowly removed by placing the solution in a vacuum oven and slowly drying at 35°C. Dry samples appear clear with an amber color.

Instrumentation

Organic content present on the modified nanoparticles and in the final NIMs

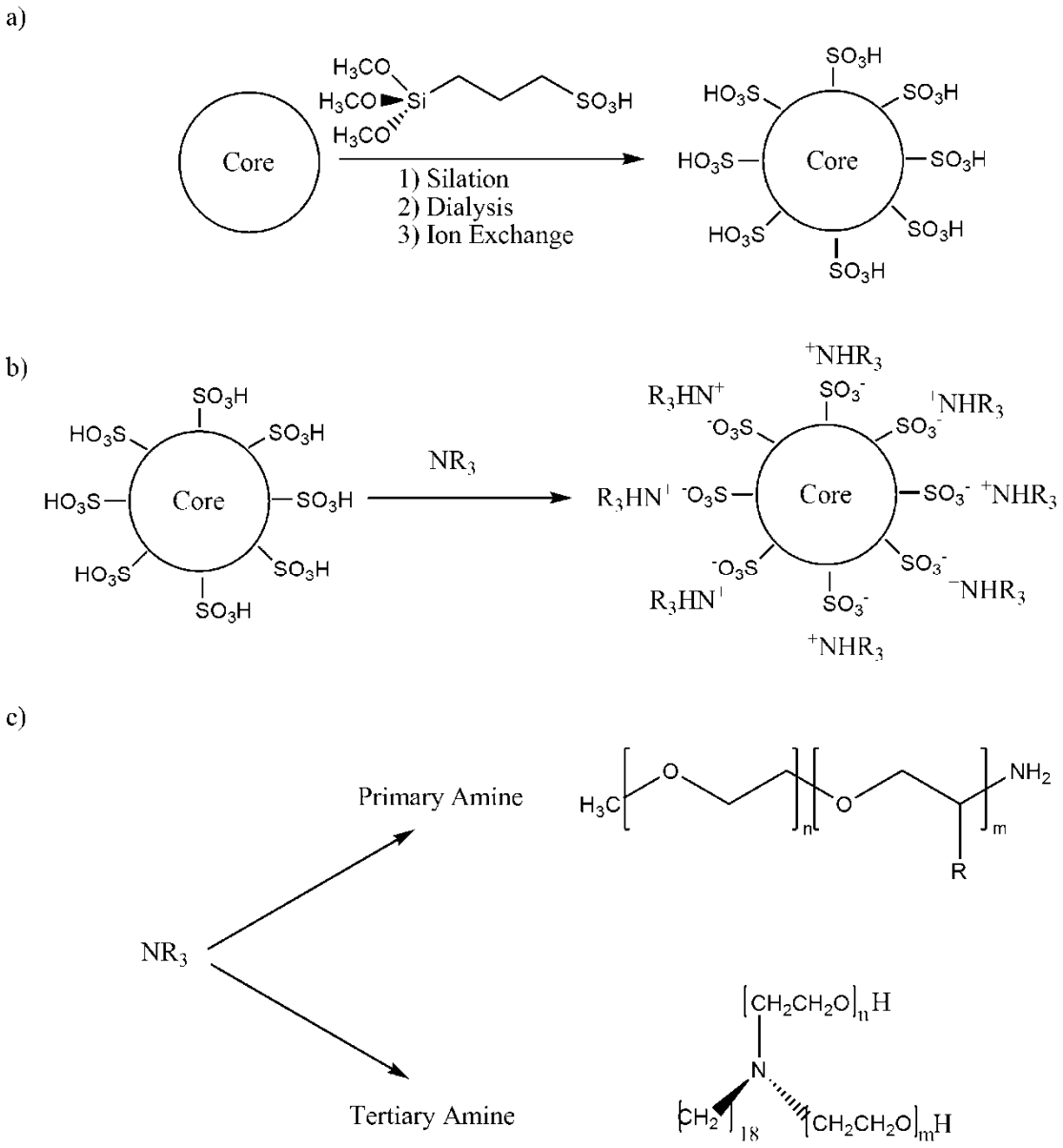

Figure 1.2 (a) Nanoparticle surface functionalization involves covalently grafting a propyl sulfonic acid silane. Subsequent purification steps involve dialyzing the nanoparticle solution against 18MΩ-cm deionized water for three days followed by an ion exchange to protonate the sulfonic acid groups. (b) NIMs are formed by reacting the acidic corona with an amine through an acid base neutralization. This results in an ionic attraction between the anionic corona and cationic canopy. (c) Two amine architectures were used for this study, a primary amine (Huntsman, Jeffamine®, $NH_2(CH_2CH_2O)_nCH_3$) and a tertiary amine (Akzo Nobel, Ethomeen® C/25, $((C_{18}H_{37})N[(CH_2CH_20)_mH][(CH_2CH_2O)_nH]$, $m + n = 15$).

state were measured by Thermo-gravimetric analysis (TGA) on a TA Q500 TGA. Small quantities of dried silica or NIMs were placed into a platinum TGA pan that was previously tarred. All samples were heated at a rate of 10°C/min up to a temperature of 550°C. The amount of weight loss measured corresponds to the organic concentration of each sample. Bright field TEM images were obtained at 120 kV with a FEI Tecnai T12 Spirit Twin TEM/STEM. The TEM images were taken by dissolving NIMs in acetone, placing a 5μL drop of the dispersion on a copper grid and evaporating the solvent.

Titration Experiments

For stoichiometric NIMs state there is a one-to-one ratio of sulfonic acid groups to amine molecules. In order to determine the nanoparticle concentration at which the equivalence point occurs, an acid-base titration measurement was performed. The modified silica suspension served as the acid while the amine solution the base. The concentration of silica particles in solution was first measured by drying out a measured quantity of solution and weighing the amount of solid leftover. For the base, the amine molecules were dispersed in 18MΩ-cm deionized water at a concentration of 3.5 % wt/wt. The base solution was placed into a buret and slowly added 1ml at a time to the nanoparticle solution while stirring. The pH of the mixture was monitored with a Fisher Scientific accumet Excel XL25 pH/mV/Temperature/ISE Meter which was calibrated every 15 minutes using buffer solutions of pH 4, 7, and 10. After every 1ml of base solution added to the nanoparticles, the solution was given a few minutes for the pH to equilibrate before it was recorded. The pH of the solution was recorded until all of the base solution had been added to the silica solution.

Results and Discussion

The Theoretical NIMS Transition

The theoretical NIMs transition can be calculated by considering the mass that the core, corona, and canopy each take up at the NIMs transition. The NIMs transition is defined as the state where each sulfonic acid corona group present on the nanoparticle surface has reacted with an amine molecule, leading to a state where there is a one-to-one correspondence of acid to base. This point can be calculated theoretically by measuring or calculating the number of sulfonic acid groups present on the nanoparticle. From a measurement of the organic content present on a nanoparticle surface from a TGA test (Figure 1.3), the number of silane molecules, n_{SIT} can be calculated from weight loss. At the equivalence point, the number of amine molecules, n_{canopy} will be equal to n_{SIT}. Once these values have been calculated, the concentration of cores at the NIMs point can be calculated using the following equation,

$$\text{NIMS } \left(\%\frac{wt}{wt}\right) = \frac{M_{core}}{M_{core} + M_{SIT} + M_{canopy}} \tag{1.1}$$

where the mass of each component can be calculated using the following relations:

$$M_{core} = \frac{4}{3}\pi R_{core}^3 \rho_{core}$$

$$M_{SIT} = n_{SIT} MW_{SIT}/N_A$$

$$M_{canopy} = n_{canopy} MW_{canopy}/N_A$$

where ρ_{core}=1.8 g/cm^3 is the density of silica, MW_{SIT} is the molecular weight of the corona molecule, MW_{canopy} is the molecular weight of the canopy, and

N_A=6.02×$10^{23}$$mol^{-1}$ is Avogadro's number. Table 1.1 shows the results of a few of these calculations based on Equation (1.1). As can be seen from these results, the NIMs transition is strongly dependent on the molecular weight of the canopy used. As an example, the HS30-SIT particles will require the same number of amine molecules to reach the NIMs state regardless of amine molecular weight. The difference in NIMs transition is therefore due to the size difference of the amine molecules, the larger the molecular weight the more mass each amine molecule will take up. This results in a NIMs transition which gets pushed to lower core concentrations as the size of the amine molecule increases.

The Experimental NIMs Transition

The NIMs transition for each system can be measured by performing an acid base titration experiment. In a typical acid-base neutralization experiment, an acid and a base are mixed while continuously monitoring the solution pH. As base is slowly added to the acid solution, the pH will rise from a low to a high value. As the two species approach the neutralization concentration, the total pH of the mixture rises rapidly from a low acidic value to a higher basic one. For a typical reaction between a strong acid and strong base,

$$HSA + SB \rightleftharpoons SA + HSB$$

where HSA is a strong acid and SB the strong base, the neutralization point will occur at pH = 7. This is due to the fact that the both the acid and base completely dissociate to produce water and salt during the neutralization. A second example involves the reaction between a strong acid and a weak base,

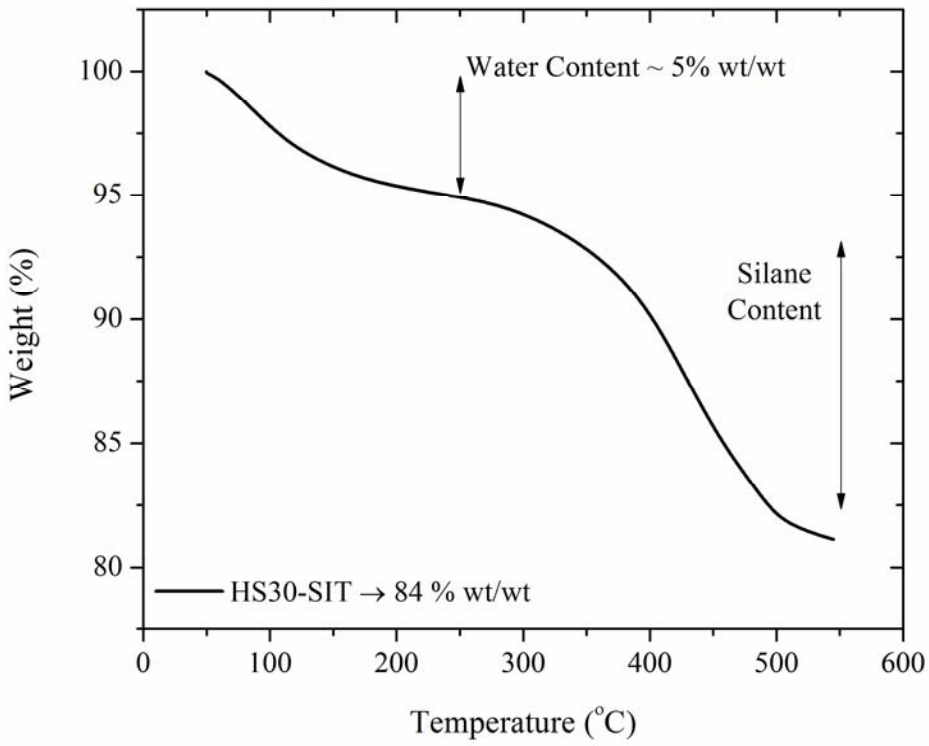

Figure 1.3 TGA weight loss graph for surface modified HS30-SIT silica nanoparticles with a core radius of 8.9nm. The first observed weight loss is due to the evaporation of water while the second (starting at ~350°C) is due to the decomposition of the silane.

Table 1.1 Theoretical NIMs transitions calculated using equation (2.1) for HS30-SIT cores with a radius of 8.9nm.

Canopy MW (g/mol)	NIMs Transition (SiO_2 content, % wt/wt)
1000	41
2000	27
3000	17.8

$$HSA + WB \rightleftharpoons SA + HWB$$

$$HWB + H_2O \rightleftharpoons WB + H_3O^+$$

The reaction of the strong acid with the weak base, WB, results in the formation of a weak acid, HWB. Next, the weak base behaves like a strong conjugate acid in water and further dissociates producing more hydronium ions. These excess hydronium ions lead to an equivalence point which occurs at a pH < 7. The final case involves the reaction between a weak acid, HWA, and a strong base,

$$HWA + SB \rightleftharpoons WA + HSB$$

$$WA + H_2O \rightleftharpoons HWA + OH^-$$

This reaction leads to the formation of a weak conjugate base, WA, which further reacts in water forming extra OH^- groups. These excess hydroxide ions lead to an equivalence point with a pH > 7.

For the NIMs systems discussed here, the reaction involves a strong acid (sulfonate groups on the core) with a weak base (the amine canopy). As shown previously, the sulfonic acid groups protonate the amine, giving it a net positive charge and creating a net ionic attraction between these two components. We therefore expect the equivalence point of this reaction to occur at pH < 7.

Figure 1.4 shows the titration curves for systems based on the HS30-SIT SiO_2 nanoparticles (R = 8.9nm) reacted with primary amines of various molecular weights. This plot shows that the NIMs transition depends on the molecular weight of the canopy. First, the pH for neutralization for this reaction is about pH = 6 for the HS30-SIT cores for every amine studied. The pH at which the equivalence point occurs is directly related to the concentration of sulfonic acid groups present on the nanoparticles. Another feature is the fact that the NIMs transition also depends on the molecular weight of the canopy. For example, Figure 1.4 shows that for systems based on HS30-SIT cores, the NIMs transition can vary from 40 % wt/wt for a 1000g/mol canopy down to 16 % wt/wt for a system based on 3000g/mol. For HS30-SIT cores, the number of sulfonic acid groups present is the same for all three titration curves shown in Figure 1.4, since the particle size is the same. Because of this the number of canopy molecules required to reach the equivalence point is the same for all three experiments as indicated by the same measured neutralization point at pH = 6.

The difference in the equivalence point is therefore due to the mass of the canopy, the larger the mass the lower the mass fraction taken up by the particle in the NIMs state. This can also be seen through equation (1.1) which shows that the mass fraction of silica nanoparticles at the NIMs transition is inversely proportional to the mass of the canopy, consistent with observed trends in Figure 1.4.

Table 1.2 lists the values of the NIMs transition for the HS30-SIT cores obtained from Figure 1.4. Also listed in Table 1.2 are the theoretical NIMs transition values obtained from calculations using equation (1.1). Upon comparison, both the experimental and theoretical values for the location of the NIMs transition are in good agreement. By using the equivalence point approach, the NIMs transition for any type of core, corona, and canopy can be located making the selection of appropriate materials for use in any desired application fairly straightforward.

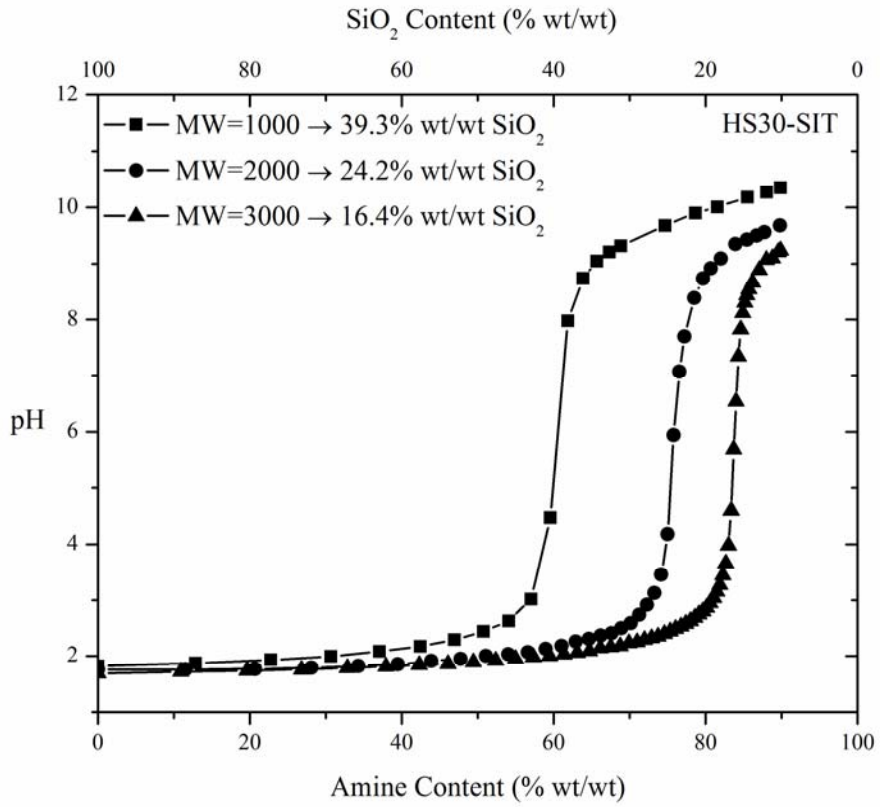

Figure 1.4 Titration curves for systems based on HS30-SIT cores and three primary amines of varying molecular weights. The equivalence point of each amine occurs at pH ~ 6, but the core concentration at the equivalence point strongly depends on the amine molecular weight.

Table 1.2 NIMs transition for HS30-SIT cores reacted with primary amines of various molecular weights with experimental and theoretical values in good agreement.

Canopy MW (g/mol)	NIMs Transition Theory (SiO_2 Content, % wt/wt)	NIMs Transition Experimental (% wt/wt)
1000	41	39.3
2000	27	24.2
3000	17.8	16.4

Upon complete removal of all the solvent, the final NIMs state resembles a molten polymer in appearance (clear, amber colored liquid) with a viscosity that depends on both the volume fraction of nanoparticles cores present as well as the molecular weight and architecture of the canopy. The polydispersity of the nanoparticles cores is also not affected during the NIMs synthesis. Light scattering studies show that stock nanoparticle solutions have inherent polydispersities on the order of ~ 14%. The polydispersity of the particles after the surface functionalization and NIMs synthesis is virtually identical with a value of about ~ 14%. Figure 1.5 shows TEM images for NIMs based on a 2000g/mol primary amine as the canopy and the HS30-SIT cores. From both TEM plots it is apparent that the cores do not aggregate and remained as single units as a result of the chemistry. The number average particle size obtained from TEM analysis is $R_{HS30\text{-}SIT} = 8.9$nm. The small spacing between particles is believed to be the organic layer which includes both the corona and canopy surrounding each core.

The hybrid nature of NIMs allows for a wide range of materials to be selected for use as the core, corona, and canopy. It is therefore critical to select a model system to characterize the basic properties of NIMs. The subsequent chapters will present data on NIMs based on 18nm diameter silica nanoparticles as the core. For the corona, a

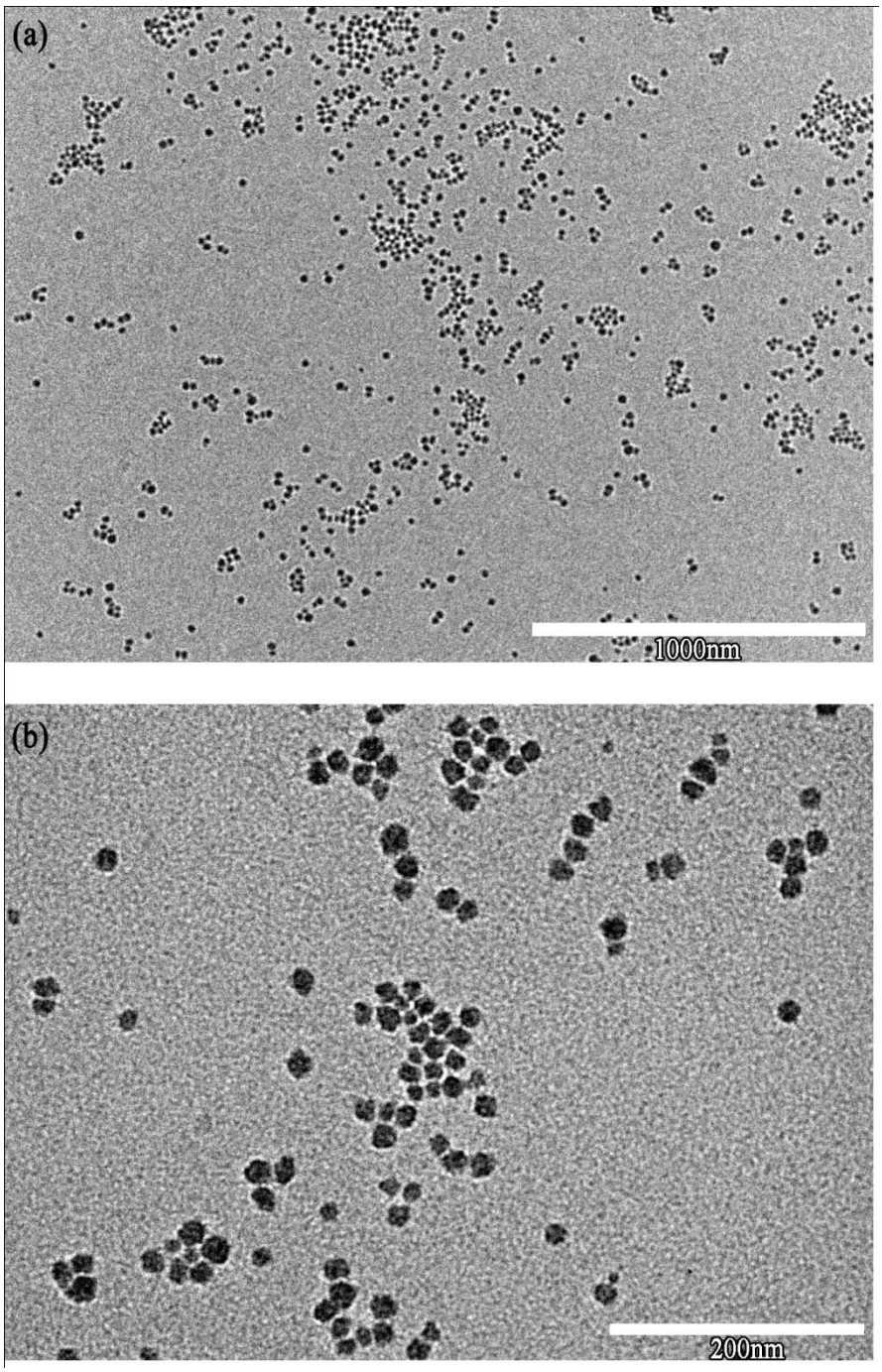

Figure 1.5 TEM images of NIMs systems based on HS30-SIT cores and a 2000g/mol primary amine as the canopy.

Table 1.3 List of canopy molecules used in this thesis.

Canopy	Canopy Geometry	Canopy MW (g/mol)	NIMs Transition (% wt/wt SiO_2)
M2070	Primary, Linear	2000	24.2
L300	Primary, Linear	3000	16.2
EM C/25	Tertiary, Star	900	42

propyl sulfonic acid silane (Figure 1.2a) was selected. Three different amines were selected to serve as the canopy for this study. Table 1.3 lists the amines used, their architecture, molecular weight, and the NIMs transition when cores with a radius of 8.9nm are used in the synthesis. This thesis will probe the effects of core volume fraction, and canopy architecture on the overall structural and rheological properties of NIMs.

Conclusion

Second generation NIMs were synthesized using a complementary approach developed for first generation NIMs. In the second generation systems the signs of the charge on the corona and canopy were reversed, with a anionic corona and cationic canopy. The cores were first modified by attaching a charged organosilane terminated by a sulfonic acid group. After purification and ion exchange, the nanoparticles were then reacted with an amine molecule which serves as the base in the acid-base reaction. This step involves the sulfonic acid groups protonating the amine molecules, giving them a net positive charge leading to a strong ionic attraction to the negatively charged sulfonic acid groups on the surface of the particles. Upon removal of the solvent, clear, amber colored materials were obtained.

The second generation procedure is a more versatile route to NIMs since systems with varying core volume fractions, canopy architectures, and physical

properties can be synthesized. Since the reaction between the core and corona involves an acid-base neutralization, the equivalence point for any desired system can be obtained through an acid-base titration experiment. Once knowledge of the NIMs equivalence point is known, then systems with an over-equivalence or sub-equivalence of cores can be synthesized. The fluidity of any sample can therefore easily be controlled by simply varying the core concentration present. Samples with very low viscosities can be obtained by adding extra amine, and samples resembling solids can be obtained by increasing the concentration of cores. TEM images show that NIMs is a synthetic route which does not perturb the core polydispersity, yielding unaggregated nanoparticles which can have a wide variety of flow behavior.

REFERENCES

[1] B. Beresfordsmith, D. Y. C. Chan, *Faraday Discussions* **1983**, 65.

[2] R. Buscall, *Journal of the Chemical Society-Faraday Transactions* **1991**, *87*, 1365.

[3] J. R. Fox, P. C. Kokoropoulos, G. H. Wiseman, H. K. Bowen, *J. Mater. Sci.* **1987**, *22*, 4528.

[4] B. J. Ackerson, N. A. Clark, *Physical Review A* **1984**, *30*, 906.

[5] B. J. Ackerson, J. B. Hayter, N. A. Clark, L. Cotter, *Journal of Chemical Physics* **1986**, *84*, 2344.

[6] B. J. Ackerson, P. N. Pusey, *Phys. Rev. Lett.* **1988**, *61*, 1033.

[7] Z. Adamczyk, B. Jachimska, M. Kolasinska, *J. Colloid Interface Sci.* **2004**, *273*, 668.

[8] H. A. Baghdadi, H. Sardinha, S. R. Bhatia, *J. Polym. Sci. Pt. B-Polym. Phys.* **2005**, *43*, 233.

[9] G. K. Batchelor, *J. Fluid Mech.* **1977**, *83*, 97.

[10] J. W. Bender, N. J. Wagner, *J. Colloid Interface Sci.* **1995**, *172*, 171.

[11] J. Bergenholtz, *Curr. Opin. Colloid Interface Sci.* **2001**, *6*, 484.

[12] G. Bossis, J. F. Brady, *Journal of Chemical Physics* **1987**, *87*, 5437.

[13] J. F. Brady, *Journal of Chemical Physics* **1993**, *99*, 567.

[14] J. F. Brady, *Journal of Chemical Physics* **1993**, *98*, 3335.

[15] J. F. Brady, *Curr. Opin. Colloid Interface Sci.* **1996**, *1*, 472.

[16] J. F. Brady, J. F. Morris, *J. Fluid Mech.* **1997**, *348*, 103.

[17] R. Buscall, *Colloids and Surfaces a-Physicochemical and Engineering Aspects* **1994**, *83*, 33.

[18] R. Buscall, J. I. Mcgowan, A. J. Mortonjones, *J. Rheol.* **1993**, *37*, 621.

[19] B. Cabane, K. Wong, P. Lindner, F. Lafuma, *J. Rheol.* **1997**, *41*, 531.

[20] L. B. Chen, B. J. Ackerson, C. F. Zukoski, *J. Rheol.* **1994**, *38*, 193.

[21] L. B. Chen, M. K. Chow, B. J. Ackerson, C. F. Zukoski, *Langmuir* **1994**, *10*, 2817.

[22] M. Chen, W. B. Russel, *J Colloid Interf Sci* **1991**, *141*, 564.

[23] E. G. D. Cohen, R. Verberg, I. M. de Schepper, *Physica a-Statistical Mechanics and Its Applications* **1998**, *251*, 251.

[24] M. E. Fagan, C. F. Zukoski, *J. Rheol.* **1997**, *41*, 373.

[25] D. R. Foss, J. F. Brady, *J. Fluid Mech.* **2000**, *407*, 167.

[26] G. Fritz, V. Schadler, N. Willenbacher, N. J. Wagner, *Langmuir* **2002**, *18*, 6381.

[27] A. Imhof, A. Vanblaaderen, J. K. G. Dhont, *Langmuir* **1994**, *10*, 3477.

[28] R. B. Jones, P. N. Pusey, *Annual Review of Physical Chemistry* **1991**, *42*, 137.

[29] P. F. Luckham, M. A. Ukeje, *J. Colloid Interface Sci.* **1999**, *220*, 347.

[30] J. Mellema, *Curr. Opin. Colloid Interface Sci.* **1997**, *2*, 411.

[31] J. Mewis, W. J. Frith, T. A. Strivens, W. B. Russel, *Aiche J.* **1989**, *35*, 415.

[32] J. Mewis, J. Vermant, *Progress in Organic Coatings* **2000**, *40*, 111.

[33] G. Nagele, *Physics Reports-Review Section of Physics Letters* **1996**, *272*, 216.

[34] T. N. Phung, J. F. Brady, G. Bossis, *J. Fluid Mech.* **1996**, *313*, 181.

[35] W. Poon, *Science* **2004**, *304*, 830.

[36] W. B. Russel, *J. Fluid Mech.* **1978**, *85*, 209.

[37] A. Sierou, J. F. Brady, *J Rheol* **2002**, *46*, 1031.

[38] A. T. J. M. Woutersen, C. G. Dekruif, *Journal of Chemical Physics* **1991**, *94*, 5739.

[39] N. W. Ashcroft, J. Lekner, *Phys Rev* **1966**, *145*, 83.

[40] M. Ballauff, *Curr Opin Colloid In* **2001**, *6*, 132.

[41] L. B. Chen, C. F. Zukoski, B. J. Ackerson, H. J. M. Hanley, G. C. Straty, J. Barker, C. J. Glinka, *Phys Rev Lett* **1992**, *69*, 688.

[42] C. G. Dekruif, W. J. Briels, R. P. May, A. Vrij, *Langmuir* **1988**, *4*, 668.

[43] L. A. Feigin, D. I. Svergun, *Structure Analysis by Small-Angle X-Ray and Neutron Scattering*, Plenum Press, New York **1986**.

[44] U. Gasser, E. R. Weeks, A. Schofield, P. N. Pusey, D. A. Weitz, *Science* **2001**, *292*, 258.

[45] W. L. Griffith, R. Triolo, A. L. Compere, *Phys. Rev. A* **1987**, *35*, 2200.

[46] M. D. Haw, W. C. K. Poon, P. N. Pusey, *Phys Rev E* **1998**, *57*, 6859.

[47] E. W. Kaler, *Modern Aspects of Small-Angle Scattering*, Kluwer Academic, Boston **1993**.

[48] W. K. Kegel, A. van Blaaderen, *Science* **2000**, *287*, 290.

[49] S. R. Kline, *J. Appl. Crystallogr.* **2006**, *39*, 895.

[50] H. M. Laun, R. Bung, S. Hess, W. Loose, O. Hess, K. Hahn, E. Hadicke, R. Hingmann, F. Schmidt, P. Lindner, *J Rheol* **1992**, *36*, 743.

[51] D. A. McQuarrie, *Statistical Mechanics*, Harper & Row, New York **1975**.

[52] M. Megens, C. M. vanKats, P. Bosecke, W. L. Vos, *Langmuir* **1997**, *13*, 6120.

[53] J. Moonen, C. Dekruif, A. Vrij, *Colloid Polym Sci* **1988**, *266*, 1068.

[54] J. Moonen, A. Vrij, *Colloid Polym Sci* **1988**, *266*, 1140.

[55] R. H. Ottewill, A. R. Rennie, G. D. W. Johnson, *Adv Colloid Interfac* **2003**, *100*, 585.

[56] R. H. Ottewill, R. A. Richardson, *Colloid Polym Sci* **1982**, *260*, 708.

[57] D. Pontoni, S. Finet, T. Narayanan, A. R. Rennie, *J Chem Phys* **2003**, *119*, 6157.

[58] P. N. Pusey, P. N. Segre, O. P. Behrend, S. P. Meeker, W. C. K. Poon, *Physica A* **1997**, *235*, 1.

[59] D. Qiu, T. Cosgrove, A. M. Howe, *Langmuir* **2006**, *22*, 6060.

[60] D. Qiu, T. Cosgrove, A. M. Howe, U. A. Dreiss, *Langmuir* **2006**, *22*, 546.

[61] D. Qiu, C. A. Dreiss, T. Cosgrove, A. M. Howe, *Langmuir* **2005**, *21*, 9964.

[62] S. K. Rhodes, J. A. Lewis, *J Am Ceram Soc* **2006**, *89*, 1840.

[63] D. O. Riese, G. H. Wegdam, W. L. Vos, R. Sprik, D. Fenistein, J. H. H. Bongaerts, G. Grubel, *Phys Rev Lett* **2000**, *85*, 5460.

[64] E. B. Sirota, H. D. Ouyang, S. K. Sinha, P. M. Chaikin, J. D. Axe, Y. Fujii, *Phys Rev Lett* **1989**, *62*, 1524.

[65] P. Vanbeurten, A. Vrij, *J Chem Phys* **1981**, *74*, 2744.

[66] A. Vanblaaderen, P. Wiltzius, *Science* **1995**, *270*, 1177.

[67] W. Vanmegen, P. N. Pusey, *Phys. Rev. A* **1991**, *43*, 5429.

[68] N. J. Wagner, R. Krause, A. R. Rennie, B. D'Aguanno, J. Goodwin, *The Journal of Chemical Physics* **1991**, *95*, 494.

[69] A. Weiss, N. Dingenouts, M. Ballauff, H. Senff, W. Richtering, *Langmuir* **1998**, *14*, 5083.

[70] M. Zackrisson, A. Stradner, P. Schurtenberger, J. Bergenholtz, *Langmuir* **2005**, *21*, 10835.

[71] M. Zackrisson, A. Stradner, P. Schurtenberger, J. Bergenholtz, *Phys Rev E* **2006**, *73*, 8.

[72] N. A. Kotov, F. Stellacci, *Adv. Mater.* **2008**, *20*, 4221.

[73] H. Y. Hao, X. Yao, M. Q. Wang, *Opt. Mater.* **2007**, *29*, 573.

[74] B. P. Binks, A. K. F. Dyab, P. D. I. Fletcher, *Chemical Communications* **2003**, 2540.

[75] A. B. Bourlinos, S. R. Chowdhury, R. Herrera, D. D. Jiang, Q. Zhang, L. A. Archer, E. P. Giannelis, *Advanced Functional Materials* **2005**, *15*, 1285.

[76] A. B. Bourlinos, S. R. Chowdhury, D. D. Jiang, Y. U. An, Q. Zhang, L. A. Archer, E. R. Giannelis, *Small* **2005**, *1*, 80.

[77] A. B. Bourlinos, V. Georgakilas, V. Tzitzios, N. Boukos, R. Herrera, E. R. Giannelis, *Small* **2006**, *2*, 1188.

[78] A. B. Bourlinos, E. P. Giannelis, Q. Zhang, L. A. Archer, G. Floudas, G. Fytas, *European Physical Journal E* **2006**, *20*, 109.

[79] A. B. Bourlinos, R. Herrera, N. Chalkias, D. D. Jiang, Q. Zhang, L. A. Archer, E. P. Giannelis, *Adv. Mater.* **2005**, *17*, 234.

[80] A. B. Bourlinos, K. Raman, R. Herrera, Q. Zhang, L. A. Archer, E. P. Giannelis, *Journal of the American Chemical Society* **2004**, *126*, 15358.

[81] A. B. Bourlinos, A. Stassinopoulos, D. Anglos, R. Herrera, S. H. Anastasiadis, D. Petridis, E. P. Giannelis, *Small* **2006**, *2*, 513.

[82] S. C. Warren, M. J. Banholzer, L. S. Slaughter, E. P. Giannelis, F. J. DiSalvo, U. B. Wiesner, *Journal of the American Chemical Society* **2006**, *128*, 12074.

[83] D. T. Wasan, A. D. Nikolov, *Nature* **2003**, *423*, 156.

[84] S. H. Sun, *Adv. Mater.* **2006**, *18*, 393.

[85] X. G. Peng, T. E. Wilson, A. P. Alivisatos, P. G. Schultz, *Angew. Chem.-Int. Edit. Engl.* **1997**, *36*, 145.

[86] R. Rodriguez, R. Herrera, L. A. Archer, E. P. Giannelis, *Adv. Mater.* **2008**, *20*, 4353.

CHAPTER 2: THE RHEOLOGY OF NIMs

Introduction

Suspensions of particles in a fluid matrix are important in everyday life, with examples including the blood in our bodies, and several home products including toothpaste and paint. For these suspensions to be useful, it is important to understand how they respond to deformation and how they flow. Because of this, a great deal of effort has been focused on understanding the rheological properties of particle filled systems. Colloidal systems, being so important, have been the subject of intense theoretical and experimental rheological characterization[1-48]. Not only are such systems interesting from a scientific perspective, but understanding how they flow and why they display certain flow characteristics is very important in the formulation of systems for commercial applications. A useful example is the flow behavior of paints[10, 37, 43]; they must be easy to brush on a surface, but must not flow down the wall on their own. This requires a balanced interplay of forces between the paint pigments, pigments and solvent, and the solvent-solvent interactions.

The rheological characterization of colloidal suspensions is now relatively well understood. This has benefited from the development of model systems used to study the effects of repulsive and attractive forces present in such suspensions. A great deal of attention has been focused on Brownian hard spheres[9, 10, 12, 14, 21, 49], where the only interaction between the particles in solution is that due to an infinitely repulsive interaction upon contact,

$$u(r) = \begin{cases} \infty, & r < d \\ 0, & r < d \end{cases} \tag{2.1}$$

where d is the diameter of the core. The hard sphere model is the simplest to solve analytically through the use of integral equations such as the Ornstein-Zernike

equation[50]. Because analytical expressions for the viscosity and stress of a suspension can be expressed for hard spheres[10], it was the focus of much research in the early days of colloid science.

Complicated expressions begin to form once other types of interactions are introduced between the particles. One example is electrostatic repulsion between particles which results from charged species on particle surfaces,

$$u(r) = \frac{4\pi\varepsilon\psi_o^2\left(r - {}^{d}/_{2}\right)}{r} \; ln\left[1 + \frac{{}^{d}/_{2}}{r - {}^{d}/_{2}} exp[-\kappa(r-d)]\right] \tag{2.2}$$

where ε is dielectric constant of the medium and ψ is the surface potential of the particles. This leads to a longer ranged interaction forming between particle species, so they can in essence "see each other" from longer distances. This complicated expression of the interaction potential does not allow the use of analytical expressions for the stress in a system of electrostatically repulsive particles, leaving only numerical calculations. There is also no real universal behavior for the rheology of electrostatically repulsive systems because as equation (2.2) shows, the potential depends on the surface charge and dielectric constant of the medium. Unlike hard spheres, the flow characteristics of such suspensions will be strongly dependent on what solvent is used, as well as the pH and salt concentration. On the other hand, these interactions do provide extra handles to fine tune the flow behavior of such systems.

Other systems which have been the focus of a great deal of rheological and theoretical study are polymer nanocomposites, where particles of various shapes, sizes, and compositions are introduced into the polymer matrix[3, 51-78]. Almost every consumer product contains components derived from some type of polymer such as

the obvious plastic grocery bags, to the more sophisticated polymeric materials used in the fabrication of modern electronic devices. Some advances in polymer derived materials are the result of introducing fillers into the polymer matrix which result in improved physical and chemical properties of the host polymer [51, 53, 58, 79-90]. There has been a strong emphasis on the development and characterization of polymer nanocomposites for the past 20 years, where nanometer sized fillers are introduced into the polymer matrix[82]. This has benefitted from changes in physical properties that occur from changing from micron-sized fillers to nanometer-sized fillers. Nanometer sized fillers tend to have very large surface-to-volume ratios, resulting in interactions which mostly take place on the surface. These interfacial interactions between the nanometer filler and polymers are then what leads to some of the improved properties that have been observed in composite materials.

In this chapter the rheological properties of NIMS are discussed. The dynamic and steady shear flow characteristics of these systems were studied as a function of particle concentration, canopy molecular weight and canopy architecture. A complete understanding of the flow properties of NIMS is crucial in developing a theoretical understanding of their behavior as well to better develop potential applications for such materials.

Experimental

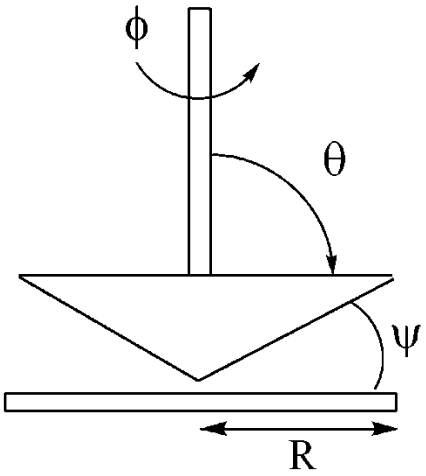

Figure 2.1 Cone and plate geometry used in rheological characterizations.

Rheological Characterization

The viscoelastic properties of NIMS were studied using a Paar Physica Modular Compact Rheometer 501 (MCR 501) equipped with 25mm diameter stainless steel cone and plate attachments with a cone angle of 1° and a Rheometrics Scientific ARES rheometer with 25mm diameter stainless steel cone and plate attachments with a cone angle of 4°. On the ARES rheometer, measurements were performed in oscillatory shear and steady shear configurations at fixed temperatures. On the Physica rheometer, measurements were performed in oscillatory shear and in steady stress creep mode at fixed temperatures above the melting temperatures of each NIMS system. Figure 2.1 shows the geometry for a cone and plate rheometer. The following expressions show the relationship between the thrust and torque measured by the rheometer and the constants used to describe the flow behavior of a material:

$$\text{Shear Stress} = \sigma_{\theta\phi} = \frac{\text{Torque}}{\frac{2}{3}\pi R^3} \tag{2.3}$$

$$\text{Shear Rate} = \dot{\gamma}_{\theta\phi} = \frac{\omega}{\psi} \tag{2.4}$$

(2.5) $$\text{Viscosity} = \eta = {}^{\sigma_{\theta\phi}}\Big/_{\dot{\gamma}_{\theta\phi}}$$

(2.6) $$N_1 = \sigma_{\phi\phi} - \sigma_{\theta\theta} = -\frac{2 * \text{Thrust}}{\pi R^2}$$

where ω is angular deformation rate. This shows that all parameters can be extracted from the resulting torque, applied deformation rate, thrust on the upper cone, and the geometrical constants of the cone and plate measurement system. Together, equations (2.3-6) can describe the rheological characteristics of a broad range of materials.

Before each measurement, all samples were dried in a vacuum oven at 35°C for 24h prior to any measurements to remove residual water. Once loaded into the rheometer, all samples were left to equilibrate in the rheometer for 2h before any measurements were performed.

Measurements in the linear viscoelastic region (LVE) were performed for all systems in oscillatory shear mode. Amplitude sweeps at a fixed temperature and fixed angular frequency of ω = 10rad/s were performed on each sample to determine the strain range of the LVE. A strain in the middle of the LVE range was then selected for oscillatory shear experiments which were performed in a frequency range of 0.01rad/s > ω > 100rad/s. During the oscillatory shear experiments, a sinusoidal shear strain is imposed,

(2.7) $$\gamma(t) = \gamma_o \sin(\omega t)$$

This deformation results in a stress that also oscillates with a phase lag,

(2.8) $$\tau(t) = \tau_o \sin(\omega t + \phi)$$

where ϕ is the phase angle. Oscillatory shear data are analyzed by decomposing the stress into two components, one in-phase with the imposed strain and one out-of-phase,

$$\tau(t) = \tau' + \tau'' = \tau_o' \sin(\omega t) + \tau_o'' \cos(\omega t) \tag{2.9}$$

Dividing through equation (2.9) by the amplitude of the strain, γ_o, yields the storage and loss modulus, where the storage modulus, *G'*, is the in phase elastic modulus and the loss modulus, *G''*, is the out of phase viscous modulus.

$$G' = {}^{\tau_o'}/_{\gamma_o} \tag{2.10}$$

$$G'' = {}^{\tau_o''}/_{\gamma_o} \tag{2.11}$$

Flow curves were obtained under steady shear and creep mode. Under steady shear, a constant shear rate was applied while the shear stress, viscosity, and first normal stress difference were monitored as a function of time. Only steady state values for all parameters were used. The flow curves are all related by equation (2.5) which states that the shear stress is directly proportional to the applied shear rate with the viscosity as the proportionality constant. Under creep, a constant stress was applied and the strain was monitored as a function of time. Once steady state creep was achieved, the shear rate was calculated by measuring the slope of the curve,

$$\dot{\gamma} = \frac{d\gamma}{dt} \tag{2.12}$$

Once the shear rate is known, the viscosity can be calculated through equation (2.5).

Results and Discussion

Oscillatory Shear Rheology

Amplitude sweeps were performed on NIMs systems to find the linear viscoelastic region for each sample. For all systems the range of accessible strain is determined by minimum and maximum torques that result from the strain. For samples with high fluidity, minimum torque requirements prevent the use of small strains, while for highly viscous samples the maximum torque that the rheometer transducer can withstand places an upper limit on the maximum accessible strain.

Figure 2.2 shows the amplitude sweeps for selected core volume fractions for systems based on the M2070 canopy. The pure M2070 canopy shows no strain dependence and only yields a measurable loss modulus with a constant value of G'' = 2.93Pa. Increasing the core concentration leads to further increases in G'' and the appearance of G' at $\varphi > 0.10$. The increase in moduli with core volume fraction is expected and has also been observed in the effect of filler concentration on nanocomposites[69, 70]. The strain sweeps for these samples do not appear to show strain dependence even for core volume fractions up to $\varphi = 0.15$ and it is only at the highest volume fraction of $\varphi = 0.192$, where weak strain softening appears. Figure 2.3 shows that increasing the molecular weight of the canopy up to 3000g/mol does not seem to change the observed strain behavior. The pure L300 canopy shows a G'' with a very similar value as observed in the M2070 amine. Further increasing the core volume fraction also leads to increases in G'' as well as the appearance of G'. The linear amine-based systems therefore show no significant structure formation which can be detected by these strain tests. For all core concentrations studied it was also found that $G'' > G'$ indicating that these systems are dissipation dominated up to the maximum volume fraction of $\varphi = 0.19$ which could be measured. Considering the low

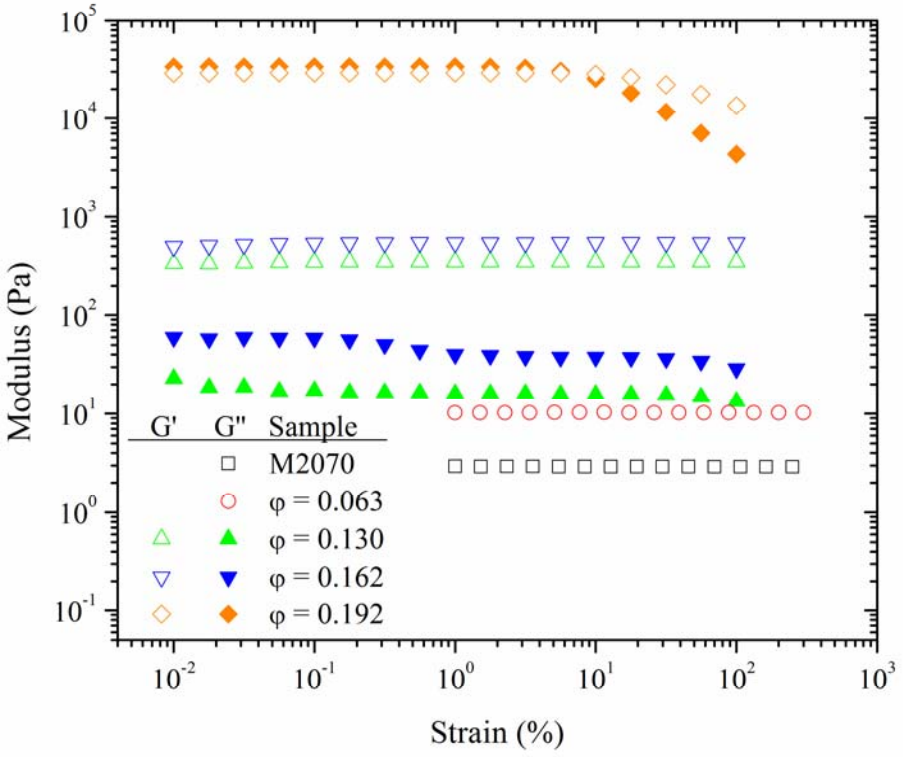

Figure 2.2 Amplitude sweeps for NIMs based on the linear M2070 canopy. Closed symbols represent the storage modulus (*G'*) and the open symbols represent the loss modulus (*G''*).

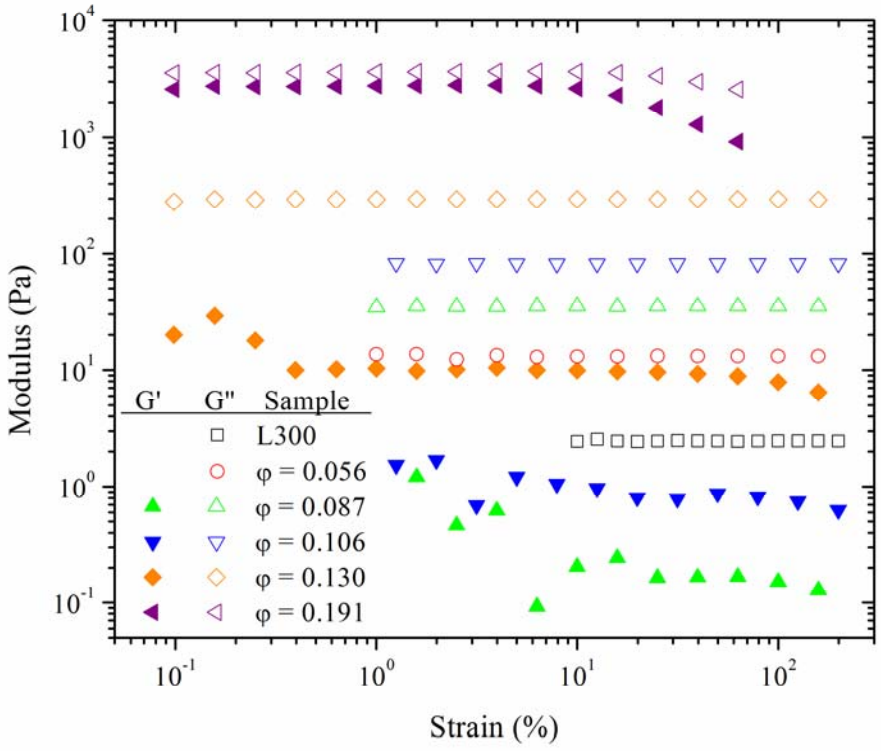

Figure 2.3 Amplitude sweeps for NIMs based on the linear L300 canopy. Closed symbols represent the storage modulus (*G'*) and the open symbols represent the loss modulus (*G''*).

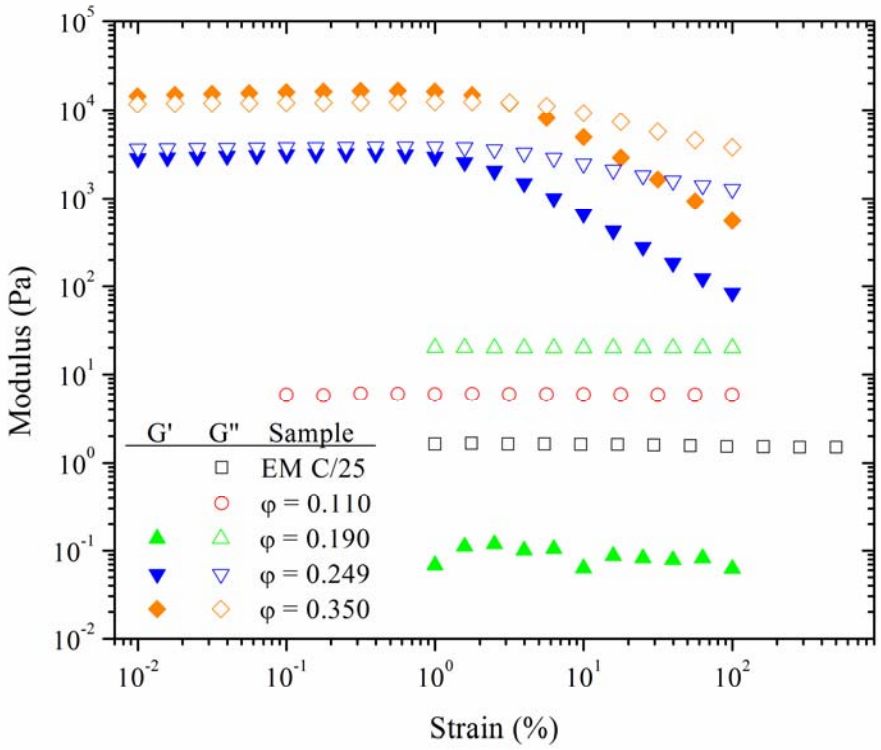

Figure 2.4 Amplitude sweeps for NIMs based on the tertiary EM C/25 canopy. Closed symbols represent the storage modulus (*G'*) and the open symbols represent the loss modulus (*G''*).

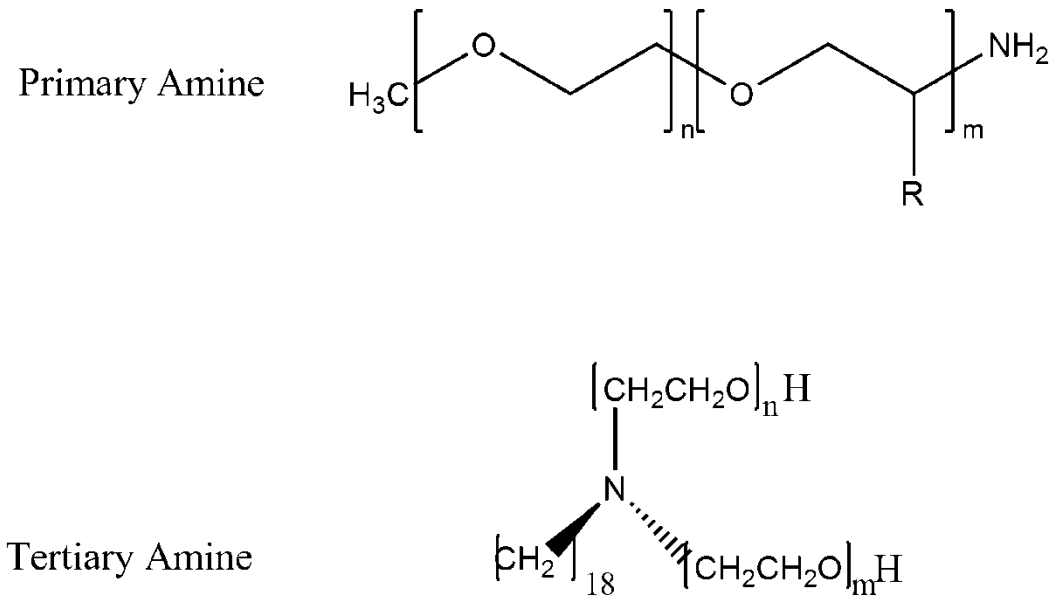

Figure 2.5 Geometry of the primary and tertiary amines used in this study.

values of the core volume fractions it is feasible that these systems tend to behave more fluid like as shown in Figure 2.2 and 2.3.

Figure 2.4 shows strain sweep results for systems based on the tertiary amine, EM C/25. The pure canopy again shows similar behavior as was observed in both linear amines (M2070 and L300). The amine seems to have no strain dependence and yields a *G''* with a very similar magnitude as the other amines studied. Again, increasing the core volume fraction leads to an increase in the measured loss and storage modulus. A few significant differences do arise by changing the shape of the canopy used. The first is the range of accessible core volume fractions. For the both the L300 and M2070 amines, the highest core volume fraction that could be studied was $\varphi = 0.19$, whereas for the EM C/25 amine, samples with core volume fractions as high as $\varphi = 0.35$ were measurable. This difference may not be due to the molecular weight differences since all the amines have molecular weights residing in the narrow molecular weight range of 900-3000g/mol. The difference must therefore be due to the different topologies of the amines, as shown in Figure 2.5. Both M2070 and L300 are linear, primary amines with a long poly(ethylene) glycol (PEG) chain. These

PEG-substituted amines are very hydrophilic when compared to EM C/25, which is a tertiary amine resembling a star polymer. A unique characteristic of EM C/25 and one which distinguishes it from the primary amines are the side groups present. EM C/25 has two PEG chains (both hydrophilic), and one alkyl chain (hydrophobic) present, resembling a surfactant. This architecture may affect the way that the amine molecules and corona molecules interact with each other

Figure 2.6 is a schematic for a hypothetical organization of the canopy molecules around each core. For primary amine-based NIMs, we assume that the PEG chains can coil into a shape resembling a sphere which can then pack fairly tightly around each core. Because of the chemistry and structure of the tertiary amine, it is quite possible that there will be micellization-type organization because of the presence of both hydrophobic and hydrophilic components. Based on the different chemistry and architecture of this amine, it is theorized that the canopy molecules may have a stronger preference for how they are organized around each core than the linear amine-based NIMs. Assuming that the alkyl groups on EM C/25 will prefer to interact with each other (as will the PEG groups), then there is the possibility of some type of micelle formation within the NIMs systems. This strong interaction amongst the canopy molecules may then provide for a stronger lubrication layer around each particle, allowing them to slide past one another with greater ease allowing EM C/25-based NIMs to be loaded with higher concentrations of cores than primary amine-based NIMs.

Figure 2.7, Figure 2.8, and Figure 2.9 show the results of frequency sweeps for NIMs based on M2070, L300, and EM C/25 canopy materials, respectively. The frequency sweeps show qualitatively similar behavior for NIMs based on all amines,

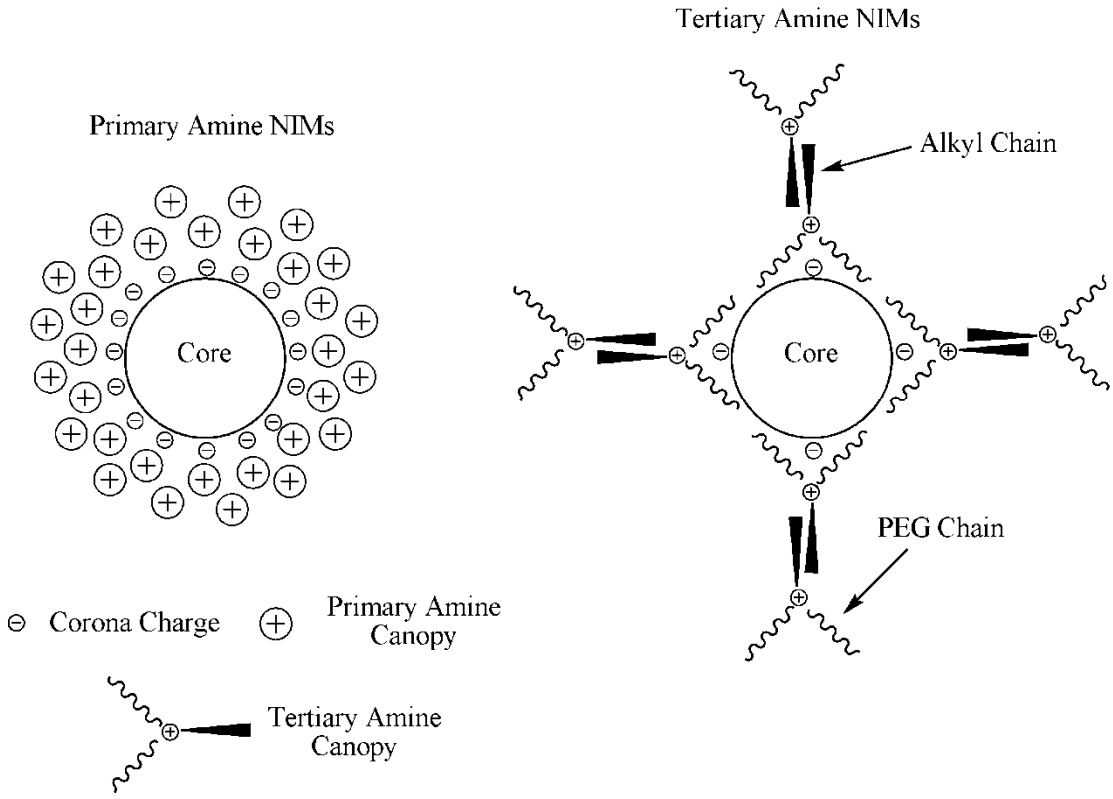

Figure 2.6 Schematic representations of how the canopy molecules organize around each core. In the case of the primary amines, it is assumed that the molecules coil up into spheres and pack as tightly as possible around the cores. Because the tertiary amine contains both hydrophobic and hydrophilic components, it is possible that they will retain their surfactant behavior in the NIMs state with the hydrophobic regions orienting towards each other.

just as was observed in the amplitude sweeps for these sets of materials. The plots show that the pure M2070, L300, and EM C/25 amines display typical fluid behavior with $G'' \sim \omega$ and a complex viscosity which follow a Newtonian behavior. All systems show that as the core concentration is increased, the magnitudes of the loss and storage modulus also increase. The dynamic behavior for NIMs based on both the M2070 and L300 show a gradual shift from simple fluid behavior at very low core concentrations ($\varphi < 0.06$) to a material resembling a solid where both G' and G'' are nearly parallel to each other and show a weak dependence on applied frequency. At core concentrations $\varphi < 0.19$, NIMs based on all amines show that $G'' > G'$ throughout the measured frequency range, indicating that these materials are viscous and show dynamical behavior similar to a liquid. At core concentrations greater than 0.19, all NIMs seem to shift to a material resembling a gel or solid where $G' \approx G''$. For M2070 and L300-based NIMs, this is the highest core concentration at which these systems can be studied using mechanical rheometry. The addition of any extra cores yields materials which are very stiff solids and do not flow under deformation or heating well above room temperature. The EM C/25-based NIMs on the other hand show very different behavior. These systems require core concentrations of about $\varphi = 0.350$ to show the same magnitude of moduli and material behavior as is observed in the primary amine-based NIMs at their maximum volume fraction. These effects were also observed in the amplitude sweeps of these systems and the explanation may be related to the structure of the amine, as discussed previously.

The plots of the complex viscosity, $|\eta^*|$, in Figure 2.7b , Figure 2.8b, and Figure 2.9b show results consistent with what is observed in the modulus plots. For volume fractions below $\varphi = 0.19$, only Newtonian behavior is observed, where the viscosity is independent of angular frequency. Once the core volume fraction is increased above this value, shear thinning manifests where the viscosity decreases

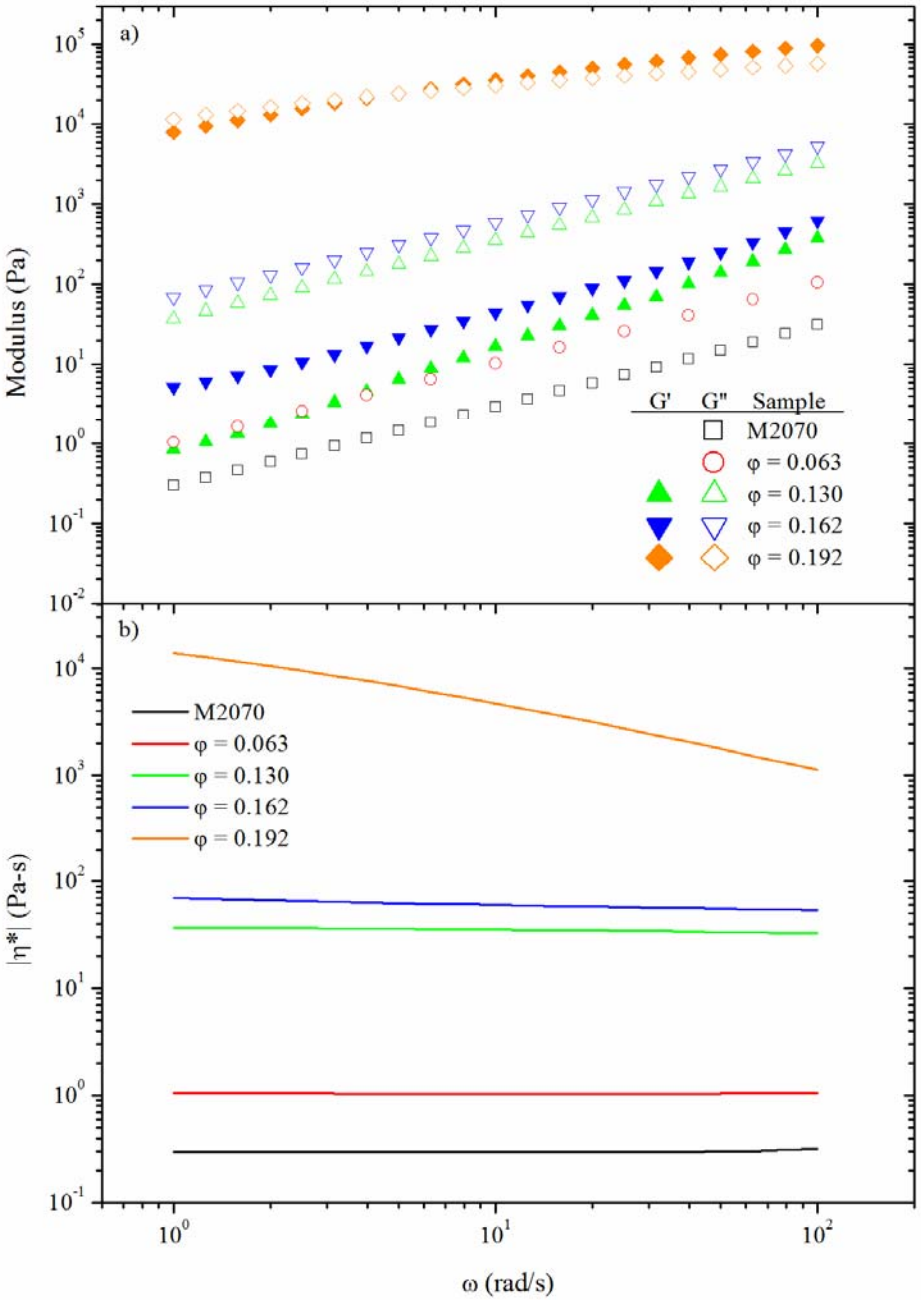

Figure 2.7 Results of oscillatory shear sweeps on M2070-based NIMs. a) Plot of storage modulus (*G'*, closed symbols) and loss modulus (*G''*, open symbols) as a function of angular frequency. b) Plots of complex viscosity as a function of angular frequency.

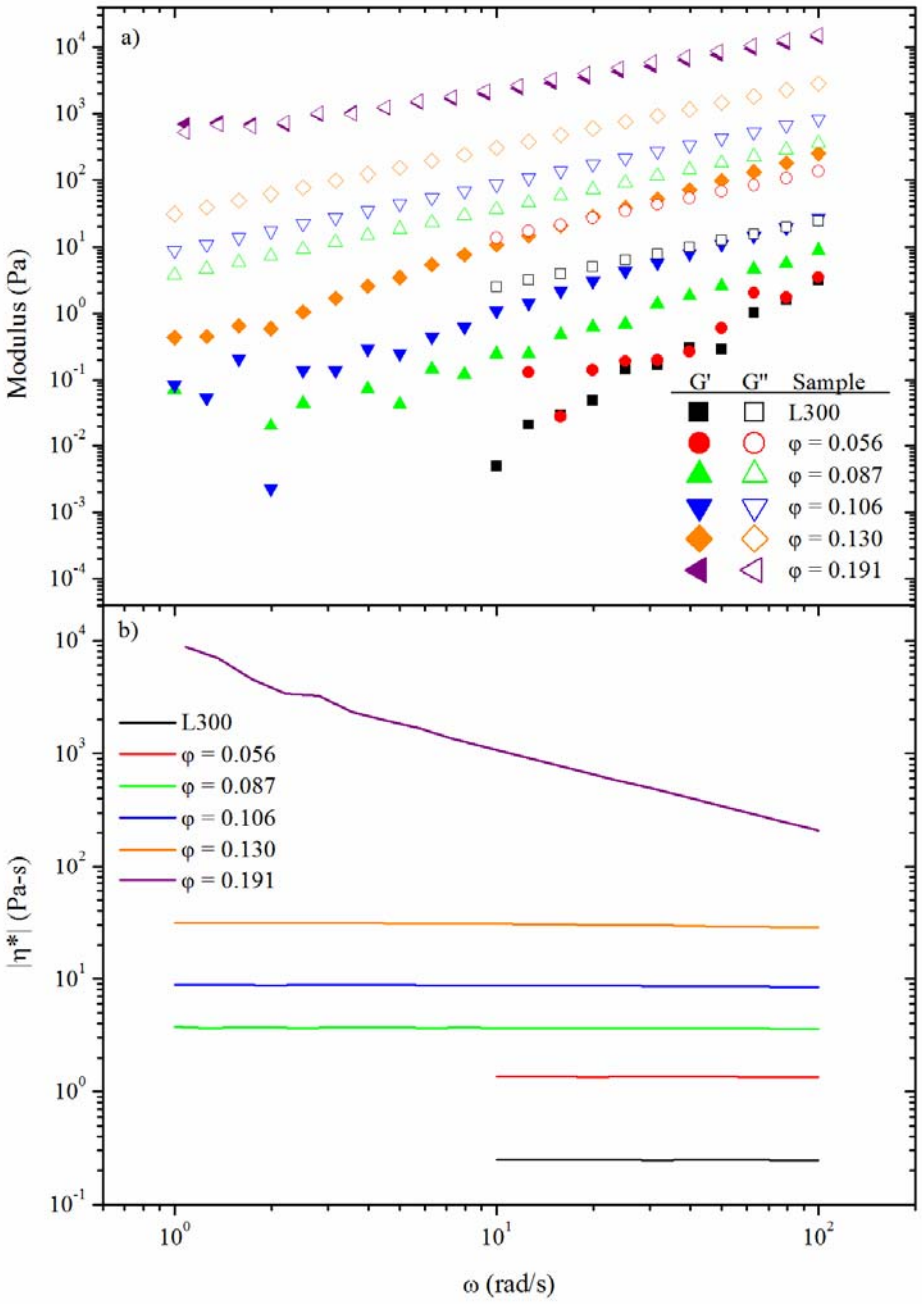

Figure 2.8 Results of oscillatory shear sweeps on L300-based NIMs. a) Plot of storage modulus (*G'*, closed symbols) and loss modulus (*G''*, open symbols) as a function of angular frequency. b) Plots of complex viscosity as a function of angular frequency.

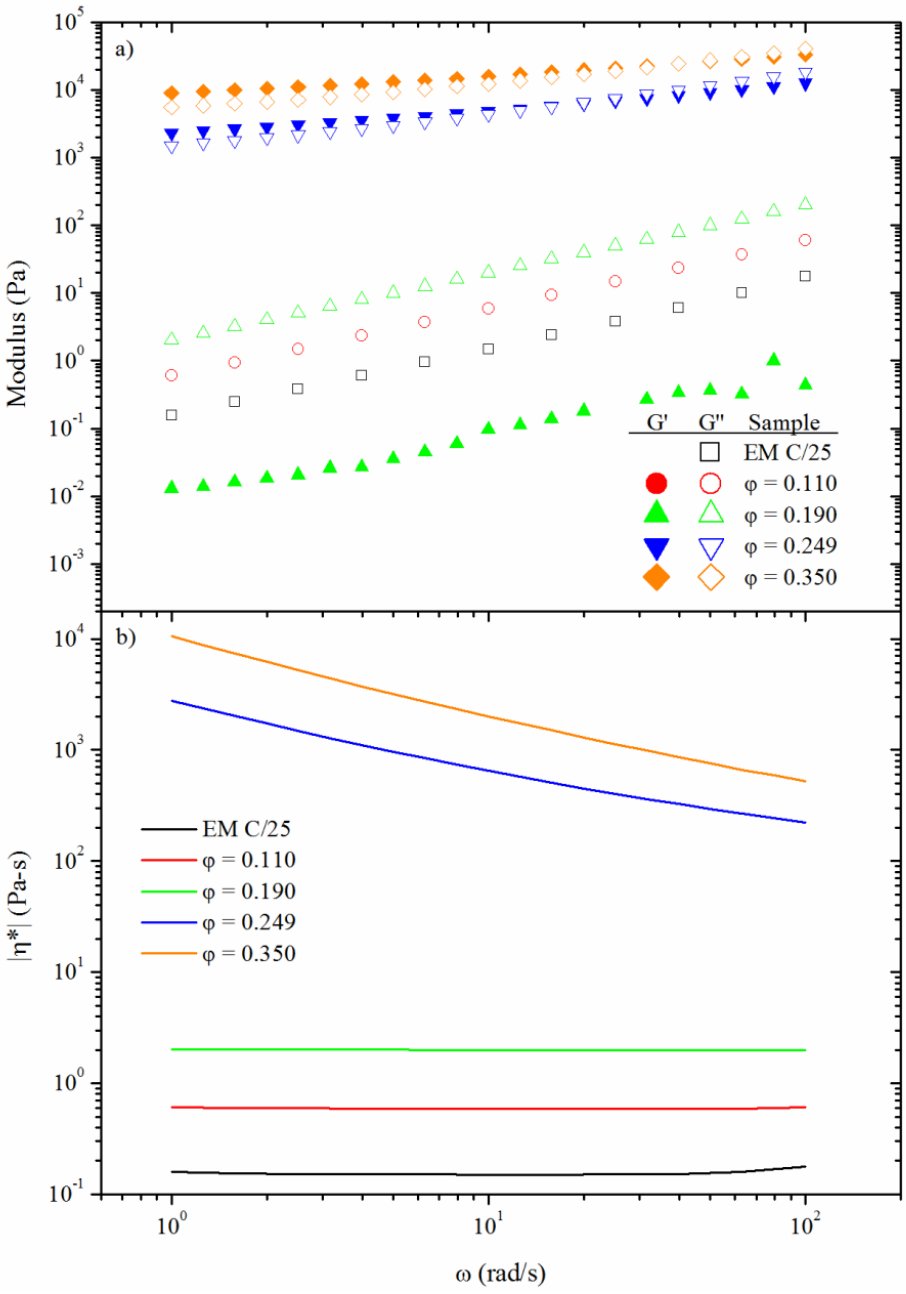

Figure 2.9 Results of oscillatory shear sweeps on EM C/25-based NIMs. a) Plot of storage modulus (*G'*, closed symbols) and loss modulus (*G''*, open symbols) as a function of angular frequency. b) Plots of complex viscosity as a function of angular frequency.

with increasing frequency. This non-Newtonian characteristic indicates that these systems are beginning to show some kind of network formation where energy storage is now possible. As the samples are deformed, this structure begins to break up and leads to a reduction in the observed viscosity.

Figure 2.10 shows frequency sweeps for two sets of samples based on both primary and tertiary amines for comparison. In this plot the differences in dynamical response and magnitude of the moduli for both canopies are more apparent. For example, by comparing the black circles (M2070-based NIMs) with the red circles (EM C/25-based NIMs) we see the dramatic differences in the values of *G'* and *G''*. For M2070 NIMs the values of *G'* and *G''* lie between 10^4-10^5Pa, while for EM C/25 NIMs *G'* and *G''* have values about 3-4 orders of magnitude smaller. The dynamical response of these two systems is also quite different, with M2070 NIMs behaving more like a highly viscous gel and EM C/25 NIMs like a viscous fluid.

Steady Shear Rheology

Flow Curves

The steady shear properties of NIMs were probed as a function of core volume fraction, canopy molecular weight and architecture. Varying these parameters gives an understanding as to how each component affects the overall rheological response of NIMs and might allow for a prediction of the behavior of future systems. When possible, the flow dynamics are compared to the vast literature already available for colloidal suspensions and polymer nanocomposites.

The flow curves for NIMs based on M2070, L300, and EM C/25 are shown in Figure 2.11, Figure 2.12, and Figure 2.13, respectively. All curves show that the magnitude of the viscosity is strongly dependent on the core volume fraction, a feature which is typical of polymer nanocomposites and colloidal suspensions[3, 10, 46, 67-69].

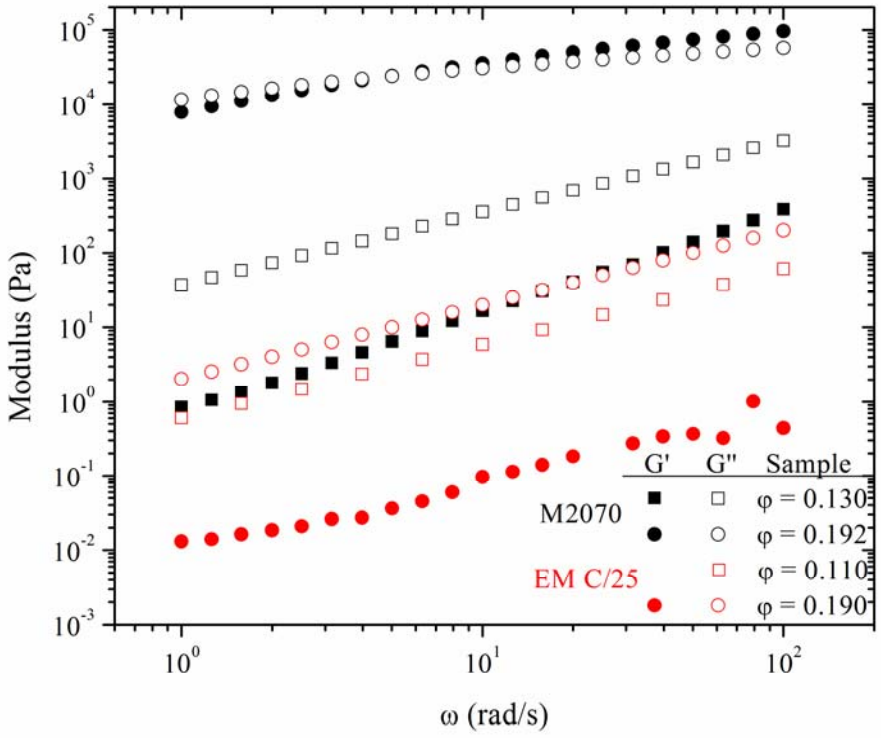

Figure 2.10 Comparison of frequency sweeps for M2070 and EM C/25-based NIMs at equivalent core volume fractions.

The reason for an increase in the viscosity can be explained schematically in Figure 2.14, which shows how the presence of a particle can increase the viscosity of a fluid. The left of Figure 2.14 shows the velocity profile of a liquid which is being pushed by an external force. The force and velocity gradient are related by[91]

$$\text{Force} \propto \text{Viscosity} \times \text{Velocity Gradient} \tag{2.13}$$

In the right of Figure 2.14, the velocity profile is perturbed by the presence of a sphere. The sphere actually reduces the velocity profile of the fluid, but because the applied force in both cases is the same, the decrease in the velocity profile must be offset by an increase in the viscosity as can be seen in equation (2.13). The more cores are present (and hence the more volume fraction they take up), the greater the increase in viscosity.

NIMs based on the M2070 amine appear to be quite Newtonian for core volume fractions up to $\varphi = 0.172$ as shown in Figure 2.11. Only at the highest measurable core volume fraction do strong non-Newtonian effects show up in the form of shear thinning. Increasing the core volume fraction only seems to increase the value of the zero-shear viscosity without introducing more complex effects. This result does seem to be consistent with the observed oscillatory shear tests where inclusion of the cores only increases the moduli and does not change the overall response. There does appear to be fairly weak shear thinning for core volume fractions greater than $\varphi = 0.162$ but the amount of viscosity decrease is very small when compared to the thinning behavior observed for the $\varphi = 0.192$ sample. Similar observations were made for NIMs based on the L300 canopy as shown in Figure 2.12. This system also shows similar behavior, where increasing the core volume fraction only leads to increases in the Newtonian viscosity of the system. Shear thinning is observed, but only at the highest core volume fractions measured and the degree of

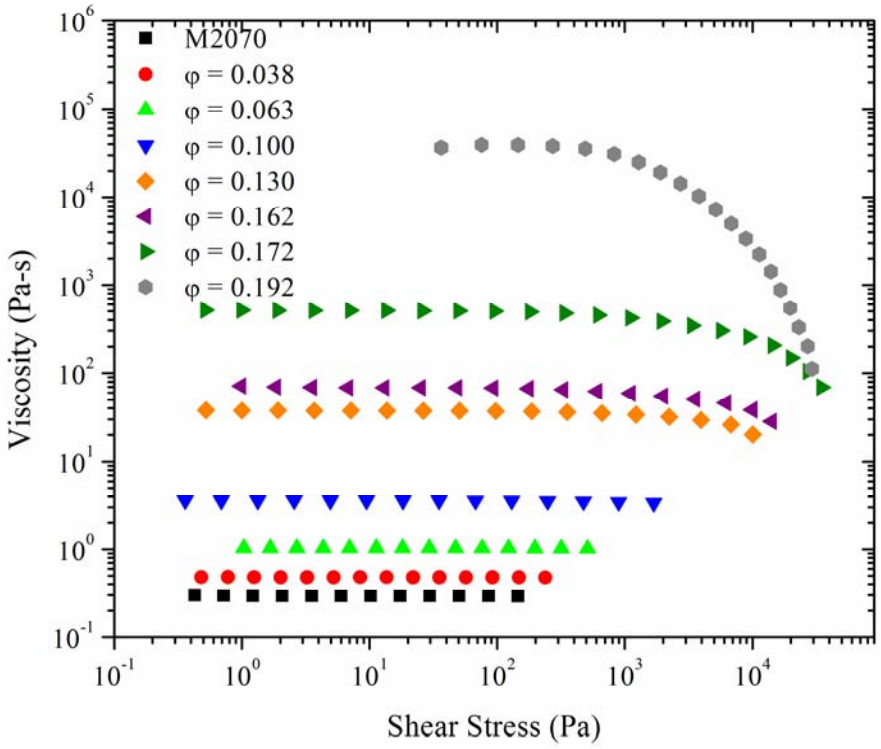

Figure 2.11 Flow curves for M2070-based NIMs at various core volume fractions. Plotted is the viscosity of the sample as a function of applied shear stress.

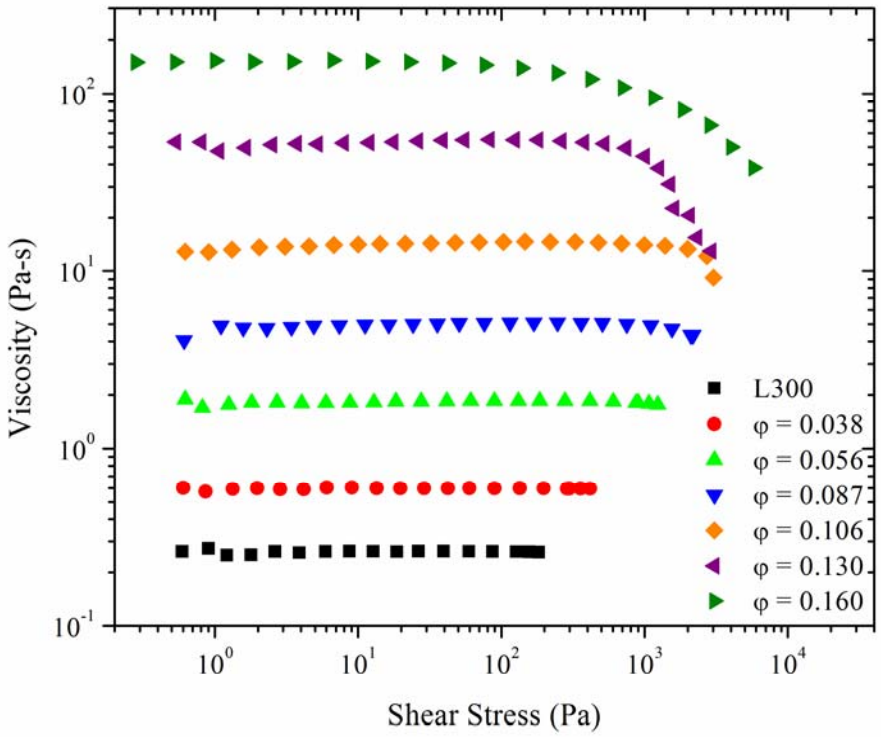

Figure 2.12 Flow curves for L300-based NIMs at various core volume fractions. Plotted is the viscosity of the sample as a function of applied shear stress.

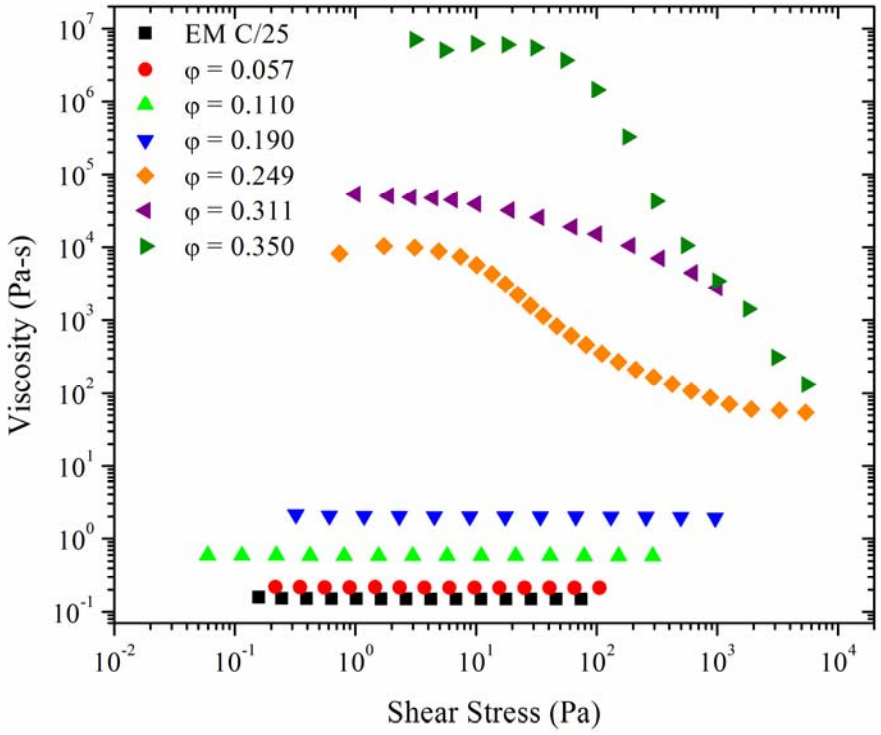

Figure 2.13 Flow curves for EM C/25-based NIMs at various core volume fractions. Plotted is the viscosity of the sample as a function of applied shear stress.

Figure 2.14 Figure explaining the viscosity increase of a fluid by the presence of a particle. On the left is a flow field for a fluid flowing through a cylinder. On the right, a particle is present and reduces the velocity profile of the flowing fluid.

thinning is also quite weak. It may be possible that shear thinning does exist for samples with lower core volume fractions at much higher shear rates than those obtainable using a standard rotational rheometer. For NIMs based on both of these linear amines, non-Newtonian effects in the viscosity only seem to manifest near core volume fractions where the material transitions into a solid and cannot be measured in the rheometer. $\varphi = 0.19$ seems to be a critical volume fraction for these linear amine-based NIMs where the system rapidly transitions into a solid.

Figure 2.13 shows different characteristics for materials based on the EM C/25 canopy. These materials are completely Newtonian for core volume fractions below $\varphi = 0.19$ unlike NIMs based on the linear amines, where shear thinning is observed at similar concentrations. In addition, the differences in the magnitude of the viscosity are also significantly different. For example, at $\varphi = 0.19$, the M2070-based sample has a zero shear viscosity of $\eta_\circ = 3.1\times10^4$Pa-s whereas the EM C/25-based sample has a value of $\eta_\circ = 2.03$Pa-s, a difference of four orders of magnitude. The range of accessible core volume fractions between the linear and tertiary amine-based NIMs is also different. For the linear amine-based NIMs, core volume fractions higher than about $\varphi = 0.19$ lead to very rigid solids which cannot be loaded onto a rheometer. Once formed, these samples remain as solids and do not flow even when heated to

temperatures of 45°C for several weeks. In contrast, NIMs based on tertiary amine canopies can access higher core volume fractions before solidifying. We find that NIMs based on tertiary amines are workable for core volume fractions up to $\varphi = 0.35$, above this concentration, solid materials which do not flow are formed. Figure 2.13 shows that systems based on the tertiary amine are non-Newtonian at core volume fractions greater than $\varphi = 0.19$, with samples showing large zero-shear viscosities and strong shear thinning. $\varphi = 0.19$ seems to be a critical volume fraction for NIMs based on either amine architecture where above this concentration materials are either solids (linear amine-based NIMs) or are non-Newtonian (tertiary amine-based NIMs). In addition, EM C/25-based NIMs show much more non-Newtonian effects than the linear amines. This again may be a consequence of the architecture and chemistry of the EM C/25 molecule. It is possible that the different hydrophobic and hydrophilic components are playing a dominant role in how the particles can flow during deformation as was shown in Figure 2.6. These results then show that the key component which is controlling NIMs rheology is the choice of canopy. All amines used are Newtonian without the addition of the cores, upon inclusion of the cores though, the architecture of the different amines will ultimately determine the observed flow characteristics.

The flow curves do not seem to show any features that can be associated with the NIMs transition which have values of $\varphi_{M2070} = 0.162$, $\varphi_{L300} = 0.104$, and $\varphi_{EM\ C/25} = 0.303$. It could be argued that near the NIMs transition for the linear based amines non-Newtonian rheology sets in as seen by the weak shear thinning. The same case cannot be made for the tertiary amine-based systems where there is no real clear change in flow behavior at or near the NIMs transition. The NIMs transition is dependent on the molecular weight of the canopy and the core size. From the

oscillatory shear rheology and the flow curves presented it turns out that flow behavior of NIMs is determined by the organization and dynamics of the canopy.

The Effects of Core Volume Fraction

The effects of core volume fraction on the viscosity of NIMs is more clearly presented in Figure 2.15 which shows plots of the reduced viscosity, $\eta_\circ/\mu$, as a function of core volume fraction for NIMs based M2070, L300, and EM C/25 canopies. The reduced viscosity is defined as the ratio of the Newtonian viscosity, $\eta_\circ$, (where the viscosity is independent of shear rate) and the viscosity of the canopy, which has values of μ_{M2070} = 0.294Pa-s, μ_{L300} = 0.261Pa-s, and $\mu_{EM\ C/25}$ = 0.149Pa-s.

All NIMs samples studied appear to diverge at core volume fractions lower than expected for a colloidal suspension of hard spheres[10, 12, 43, 92]. Although there is still no consensus as to the value of maximum packing fraction which should be used in spheres, some typical values are φ_m = 0.494, which is the liquid volume fraction of colloids at the phase boundary[93], or φ_m = 0.58, which is the glass tranistion[94], or φ_m = 0.636, which is random close packing for spheres[95].

The plots of reduced viscosity for NIMs based on the linear amines (M2070 and L300) appear almost identical. They both follow a very similar trend as the core concentration is increased with very similar values of reduced viscosity at each given core volume fraction. This trend is not too surprising considering the molecular weight difference between the two amines is not large. It is quite possible that there will be significant differences as the molecular weight is increased to larger values on the order of 10^3-10^5g/mol. The trend for EM C/25 NIMs, however, is different from what is observed in the linear amines. First, the maximum volume fraction for the linear amine systems is φ_m = 0.19, while for the tertiary amine it is φ_m = 0.35. The second is the amount by which the reduced viscosity increases with volume fraction. The tertiary amine NIMs seem to rise more slowly than those based on the primary

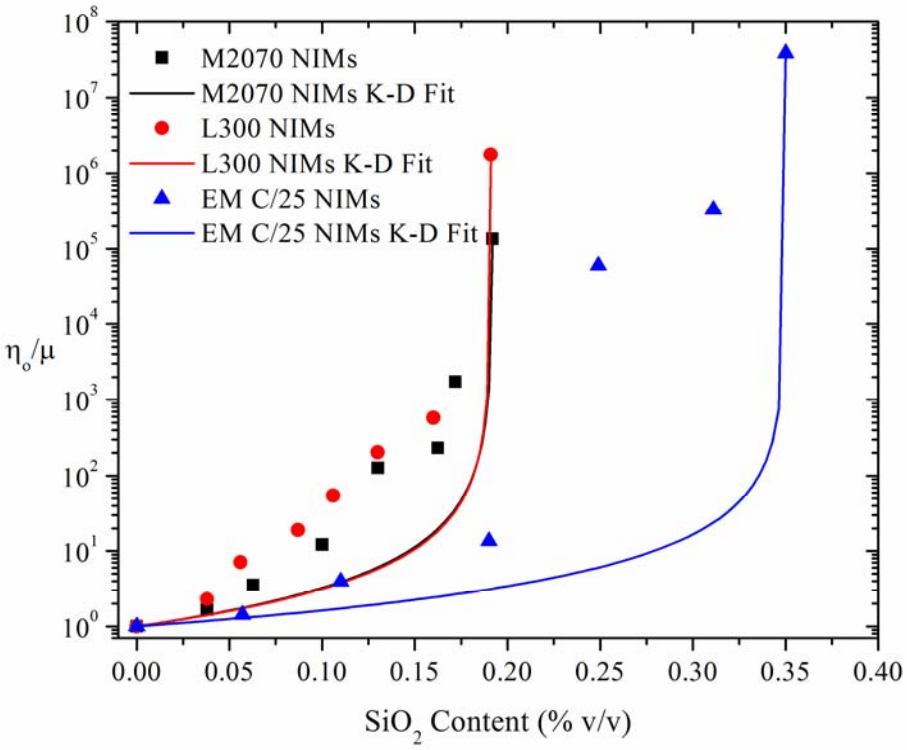

Figure 2.15 Plot of reduced viscosity (ratio of zero-shear viscosity to canopy viscosity) as a function of hard core volume fraction. Plotted are reduced viscosities for NIMs based on the M2070 canopy (■), the L300 canopy (●), and they EM C/25 canopy (▲). The lines are fits of the Krieger-Dougherty equation.

amines. This was also observed in the flow curves, where at the equivalent core volume fractions tertiary amine-based NIMs had a viscosity which was four orders of magnitude smaller than for the M2070 NIMs. Again, this difference is more likely due to the shape and chemistry of the EM C/25 canopy than the molecular weight. The different hydrophobic and hydrophilic groups present on the EM C/25 amine may be creating an extra lubrication layer around each particle which allows it to flow with much greater ease than the primary amine which may just be packing as tightly as possible around each core. Again, Figure 2.15 does not seem to show any features which can be attributed to the NIMs transition since all curves show a gradual increase with core volume fraction with no distinct transitions in the curves.

Plotting the reduced viscosity as a function of core volume fraction may not be the correct way to present this data. If it is assumed that during flow the core and attached corona move in sea of canopy molecules, then the filler volume fraction should include contributions from both components. To probe the effects of an extra layer of material around each particle, the data in Figure 2.15 was fit with the modified Krieger-Dougherty equation[43, 96, 97],

$$\eta_\circ/\mu = (1 - \varphi_{\text{eff}}/\varphi_{\text{m}})^{-[\eta]\varphi_{\text{m}}} \tag{2.14}$$

$$\varphi_{\text{eff}} = \varphi(1 + \delta/a)^3 \tag{2.15}$$

where $\eta_r=\eta_\circ/\mu$ is the reduced viscosity, a is the radius of the core, φ_m is the maximum packing fraction, and δ is the thickness of the shell layer surrounding the particle. This form for the Krieger-Dougherty equation has proven useful in describing plots of reduced viscosity for particles with an extra layer material surrounding the cores. This layer thickness must be taken into account when applying the Krieger-Dougherty equation because the core particles will appear effectively larger while in the NIMS

state. All values reported for the volume fraction are of the hard core volume fraction, without taking into account extra layers present from the corona. Assuming that the core nanoparticles and the attached corona are flowing in a fluid of canopy molecules during deformation, then the hard core volume fraction must be multiplied by the constant $(1+\delta/a)^3$ as shown in equation (2.15). Using a value of a = 8.9nm for the core radius (obtained from TEM image analysis), and assuming the thickness of the corona layer around the particle has a value of δ = 0.5nm, yields $(1+\delta/a)^3 = 1.18$. The effective volume fraction for the cores in NIMs which takes into account the corona layer is then equal to $\varphi_{eff} = 1.18\varphi$ based on these assumptions.

Fitting the data in Figure 2.15 with the Krieger-Dougherty and varying the constant $(1+\delta/a)^3$ will then give an experimental value for the layer thickness around the cores. The intrinsic viscosity was fixed and set to $[\eta] = 2.5$ which is the Einstein value for spheres, while φ_m and $(1+\delta/a)^3$ were varied until the best fit was achieved. Table 2.1 lists the parameters obtained from the fits of the model to the experimental data. The model underestimates the rise in reduced viscosity for M2070 NIMs (black squares and black line), but it does capture the divergence point of the curve. Surprisingly, the maximum volume fraction obtained from the model was $\varphi_m = 0.638$, very close to random close packing for spheres. The fit also yielded $(1+\delta/a)^3 = 3.331$, which is almost three times larger than the theoretical estimates. This parameter then yields a layer thickness around each core of δ = 4.392nm giving an effective core radius of 13.292nm. The Krieger-Dougherty fits for L300 and EM C/25-based NIMs also underestimate the rise in reduced viscosity but do capture the divergence point. The results of fitting the Krieger-Dougherty equation to the L300 and EM C/25 samples yield effective radii of 13.292nm (δ = 4.167nm) and 10.862nm (δ = 1.962nm), respectively. These values are larger than would be expected if it were only the core and corona contributing to the effective volume fraction, indicating that the

Table 2.1 List of parameters obtained from fitting the data in Figure 2.15 with the Krieger-Dougherty equation. The intrinsic viscosity was set to the expected value of spheres, [η] = 2.5.

Canopy	φ_m	$(1+\delta/a)^3$	δ (nm)	R_{eff} (nm)
M2070	0.638	3.324	4.382	13.282
L300	0.637	3.331	4.392	13.292
EM C/25	0.647	1.798	1.922	10.822

contribution from the canopy must also be taken into account in the calculation of the effective volume fraction.

This analysis leads to the conclusion that the core, corona, and canopy all flow together during deformation. The values of layer thickness around each core and the size of the canopy can be used to roughly calculate the amount of canopy that wraps around each nanoparticle. Calculations of the canopy size will be based on the end-to-end distance of a fully extended chain which is given by

$$L = Nl \tag{2.16}$$

where N is the number of repeat units and l is the length of each repeat unit. This can then be used to calculate the radius of gyration of the amine molecules using the expression for a freely jointed chain

$$R_g = \frac{\sqrt{N}l}{\sqrt{6}} \tag{2.17}$$

Once the radius of gyration of the amine is calculated, it can then be used to find the geometric radius of the molecule. The relationship between the radius of gyration and geometric radius can be calculated by assuming that the amine will take the shape of a sphere:

$$R_g^2 = \frac{\int r^2(\rho(r) - \rho_s)d^3r}{\int(\rho(r) - \rho_s)d^3r}$$

(2.18)

$$R_g^2 = \frac{\int r^2 r^2 dr}{\int r^2 dr}$$

$$R_g^2 = \frac{3}{5}R^2$$

where it is assumed that $\rho(r)$ is uniform and equal to a constant. The conversion from radius of gyration to geometric radius requires multiplying the radius of gyration by a constant value of 1.30.

The calculation of the radius of gyration of the M2070, L300, and EM C/25 amines will assume that the repeat unit for each of these molecules is ethylene oxide. A rough estimate for the repeat unit length gives a value of l = 0.36nm which will be used to calculate the extended chain length for each of the canopies used in this study. These numbers yield the following values for the radii of the canopies: R_{M2070} = 1.215nm, R_{L300} = 1.541nm, and $R_{EM\ C/25}$ = 0.735nm, values which are consistent with molecular dynamics simulations of poly(ethylene) oxide and poly(ethylene) glycol polymers of similar molecular weights[98]. To calculate the effective radius of each particle which contain contributions from the core, corona, and canopy require the following equation

$$R_{eff} = R_{core} + l_{corona} + d_{canopy} \quad (2.19)$$

where R_{core} = 8.9nm is the core radius, l_{corona} = 0.5nm is the length of the corona layer around each particle, and $d_{canopy} = 2R_{canopy}$ is the diameter of each canopy.

Using equation (2.19) the calculated effective radii for NIMs based on each canopy are $R_{eff,M2070}$ = 11.83nm, $R_{eff,L300}$ = 12.482nm, and $R_{eff,EM\ C/25}$ = 10.87nm. Comparing the calculated values for the effective radius with the experimental ones, it turns out that the calculated values are less than what is measured from the Krieger-Dougherty fits except for NIMs based on EM C/25. These numbers indicate that there are about 1-2 layers of canopy molecules surrounding each core particle. It is difficult to know what the conformation of the canopy molecules will be when surrounding each particle but a possibility is that it may lie somewhere in between the two extremes of either being completely coiled up into sphere or fully extended. Based on entropy arguments, it is more likely that the canopy molecules more closely reside on the end resembling a sphere. In this case, the confirmation of NIMs may consist of a core particle surrounded by a corona, then further surrounded by spheres of canopy molecules as depicted in Figure 2.16a. Steric hindrances will prevent all the canopy molecules that were required to fully react with the corona groups to tightly pack around the core. To accommodate all of the canopy molecules, they must then reside in layers around each particle, as shown in Figure 2.16b. A consequence of this organization is that the outer layers will be weakly bound to the inner corona groups. If the strength of the electrostatic attraction has the form shown in equation (2.2), then the strength of the attraction between the corona and canopy groups will significantly drop off with increasing separation and will strongly depend on the dielectric constant of the amine. This weaker interaction between the outer layers of canopy and the core will then allow for the canopy molecules to be quite mobile and may be able to hop from core to core. Recent Nuclear Magnetic Resonance (NMR) measurements by Jeserpsen et. al. do confirm these assumptions. Using NMR relaxation and pulse-field

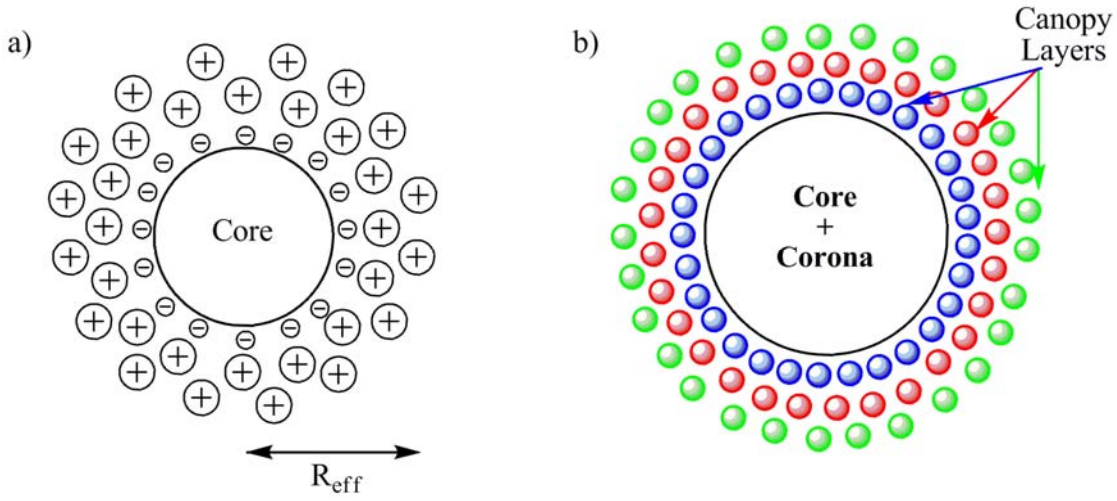

Figure 2.16 Model of NIMs unit. a) The canopy molecules can be thought of as spheres (positive symbols) surrounding the core and corona (negative symbols). b) Because of steric hindrances, the canopy molecules reside in layers around the core and corona, with the inner layers more strongly bound to the core.

gradient diffusion experiments, it was reported that the diffusion of the canopy does not seem to be hindered by the presence of the core particles[99]. In their experiments, Jespersen et. al. find that the canopy undergoes exchange between nanoparticles. These observations support this model where the outer layers of canopy molecules are more weakly bound and can diffuse with greater freedom as opposed to the inner layers which are strongly bound to the corona. Based on this model it is assumed that during deformation the core, corona, and inner canopy layer flow together. The outer canopy layers may serve as an extra fluidization medium which is in constant flux. It may be possible that the outer layers "peel" off the cores during flow and "reform" while at rest. This model also supports the results presented on the oscillatory shear rheology and the flow curves. The oscillatory shear rheology and flow curves show that the dynamical behavior of NIMs does not seem to change by inclusion of the cores. The curves all retain the same type of behavior, but only show increasing moduli and viscosity. As the number of layers gets reduced due to increasing core volume fraction, it is possible that the particles may not be as lubricated, resulting in

increases in viscosity and moduli. Also, the lack of observed structure in the strain sweeps points to a different reason for the increases in moduli. It is quite plausible that this dynamic exchange of canopy molecules in addition to the canopy organization are controlling the rheology of NIMs.

The fits of the Krieger-Dougherty equation to the experimental data of Figure 2.17 does underestimate the experimental data and is mainly due to the choice of value for the intrinsic viscosity, $[\eta] = 2.5$. Information on the layer thickness around each core is mainly extracted through the maximum packing fraction which fits the data best. To attempt at better fit to the experimental data, the value of the intrinsic viscosity was also varied with the results presented in Figure 2.17 and Table 2.2 listing the parameters of each fit. Comparing with the values of φ_m and $(1+\delta/a)^3$ obtained by fixing $[\eta]$, it is found that the variation of $[\eta]$ did not affect those values. The resulting changes in δ were also small, which in turn does not change the value of measured effective radius, R_{eff}, for each NIMs system based on the three different amines. Figure 2.17 also shows that varying $[\eta]$ does significantly improve the fits of the model to the data as can be seen by the lines following the experimental data. For NIMs based on the M2070 and L300 amines, the fits yielded values of $[\eta]_{M2070} = 6.2$ and $[\eta]_{L300} = 6.5$ while fits to the EM C/25 NIMs yielded a value of $[\eta]_{EM\ C/25} = 7.7$, a value a bit larger than that obtained for the linear amines. These numbers are not physically meaningful if the entire NIMs unit is considered to have the shape of a sphere. The two possible explanations for this discrepancy are either that the rheological behavior of NIMs cannot be explained by the Krieger-Dougherty equation or it is not correct to assume that the shape of the NIMs unit is a sphere. Since the associated canopy molecules are rapidly detaching and reattaching, it is possible that the NIMs unit will not have the shape of a sphere during flow.

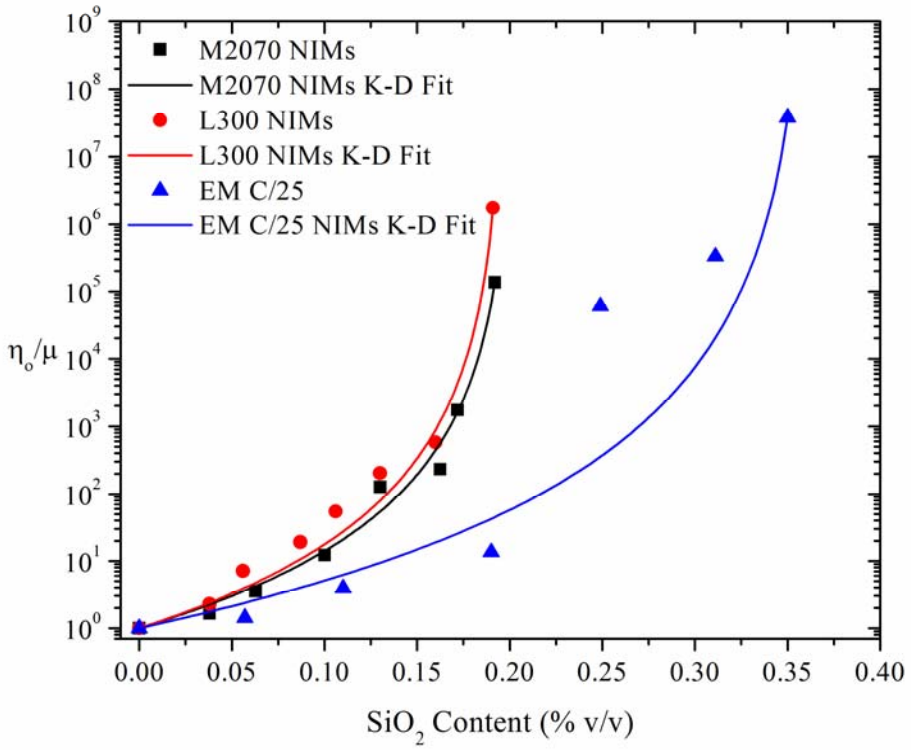

Figure 2.17 Plot of reduced viscosity (ratio of zero-shear viscosity to canopy viscosity) as a function of hard core volume fraction. Plotted are reduced viscosities for NIMs based on the M2070 canopy (■), the L300 canopy (●), and they EM C/25 canopy (▲). The lines are fits of the Krieger-Dougherty equation with the intrinsic viscosity ([η]) varied to achieve the best fit.

Table 2.2 Parameters obtained from fitting the Krieger-Dougherty equation to the data in Figure 2.17.

Canopy	φ_m	$[\eta]$	$(1+\delta/a)^3$	δ (nm)	R_{eff} (nm)
M2070	0.622	6.182	3.093	4.067	12.967
L300	0.622	6.492	3.165	4.167	13.067
EM C/25	0.657	7.653	1.818	1.962	10.862

Several reports have shown that the intrinsic viscosity of dispersions is strongly dependent on the shape and aspect ratio of the particles[100-104]. In a study using rods and platelets as particles in suspension, Kwon et. al. measured intrinsic viscosities with values of $[\eta]$ = 12-125, showing that a wide range of intrinsic viscosities is possible[101]. If NIMs take on the shape of an ellipsoid, it is possible to use the following expression to calculate the aspect ratio of the NIMs unit based on the fit values of $[\eta]$[100]:

(2.20) $$[\eta] = 2.5 + 0.4075\,(p-1)^{1.508}$$

This expression shows that the anisotropic shape of the particles requires an additional term to the standard intrinsic viscosity of spheres ($[\eta]$ = 2.5). The expression is plotted in Figure 2.18 to show how the intrinsic viscosity varies with the particle aspect ratio. Assuming equation (2.20) can be used to calculate the aspect ratio of NIMs, for linear amine-based NIMs it yields values which vary between $5.2 < p < 5.5$, while for the tertiary amine-based NIMs p = 6.4. Since the cre and corona are both rigid, the only shape change that can arise would be due to the deformation of the canopy layer around the cores. It was shown previously that the effective radius of the core obtained from fits of the Krieger-Dougherty equation were a bit larger than the

theoretical values assuming a single monolayer of canopy molecules around each core. This led to a hypothesis that the canopy molecules reside in layers around the cores, a consequence of the steric hindrances associated with trying to pack the amines around the core. It may be possible that these outer layers of the canopy are deforming during flow, leading to a non-spherical shape for the unit and may explain why the measured intrinsic viscosity is larger than what is expected for spheres. This hypothesis does still require further experimental evidence since a single fit to obtain the intrinsic viscosity is certainly not enough proof. One method by which this theory can be verified is through small-angle neutron scattering measurements during shear. Because neutrons interact with the nuclei of atoms, they can be used to directly probe the canopy and measure if the size and shape of the NIMs unit changes during shear. Since the cores are effectively larger, plotting the reduced viscosity as a function of core volume fraction does not provide an accurate picture of the volume fraction dependence on the reduced viscosity. Figure 2.19 shows the results of the reduced viscosity as a function of effective core volume fraction, which is calculated by using equation (2.15). Once scaled, the reduced viscosity data for the M2070 and L300 NIMs overlap throughout the entire measured range, while EM C/25 NIMs appear to yield larger values of the reduced viscosity. Also plotted in this Figure 2.19 is Brady's expression for the asymptotic prediction of hard sphere colloid behavior[10]

$$\eta_\circ/\mu = 1.3\left(1 - \varphi/\varphi_m\right)^{-2}. \tag{2.21}$$

The reduced viscosity of NIMs does rise faster than what is expected for hard sphere colloidal behavior but both systems do seem to show reduced viscosities which diverge at random close packing for spheres, $\varphi_m = 0.63$. The results indicate that it is

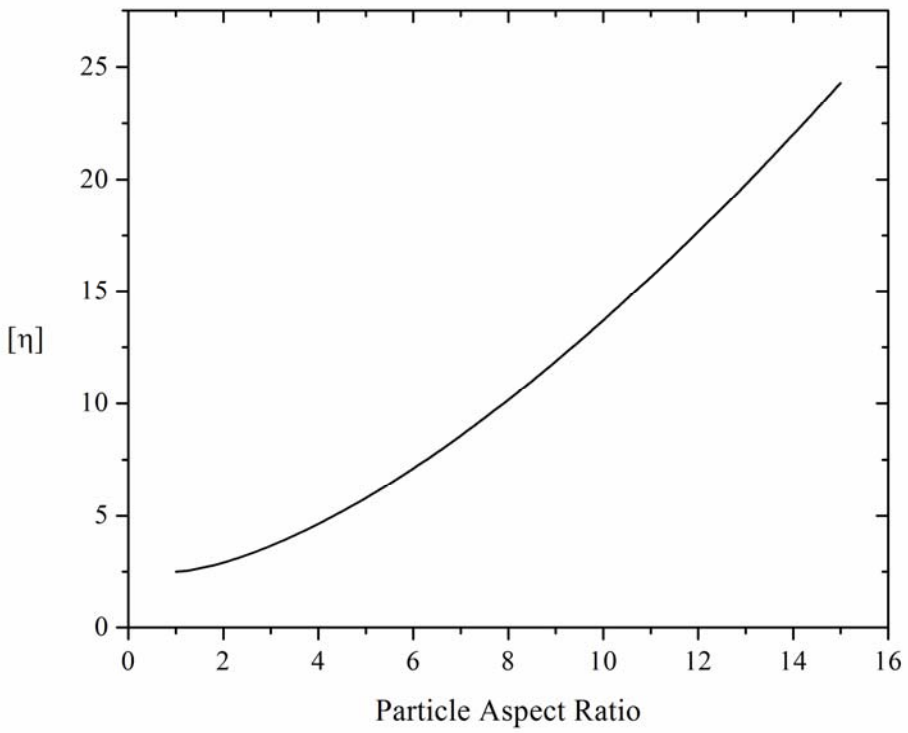

Figure 2.18 Plot of intrinsic viscosity as a function of particle aspect ratio for ellipsoid particles. The line is a representation of equation (2.20).

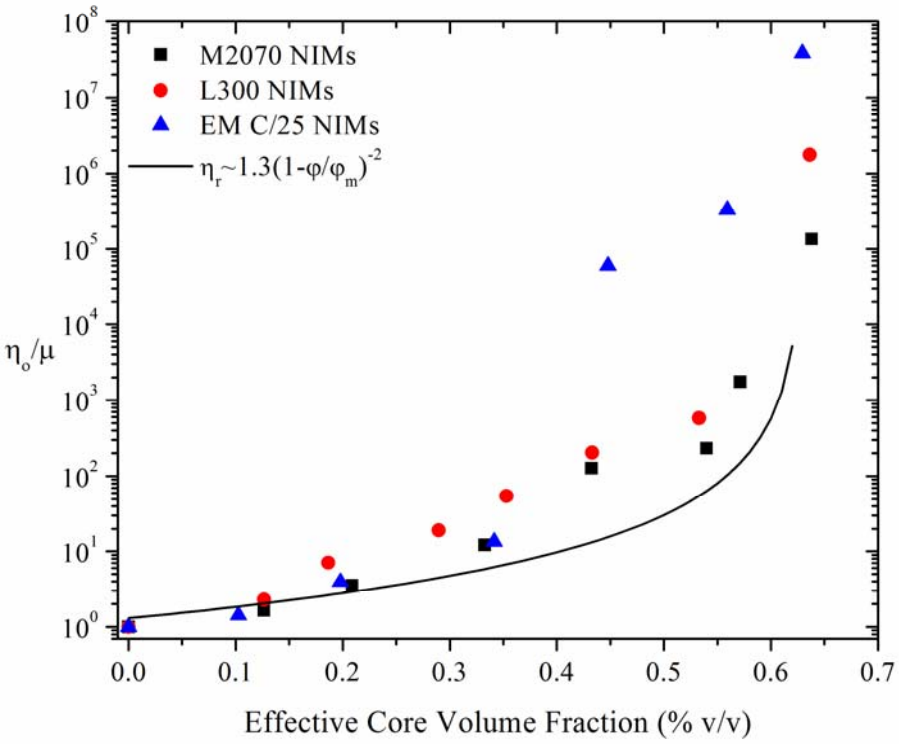

Figure 2.19 Plot of reduced viscosity (ratio of zero-shear viscosity to canopy viscosity) as a function of effective core volume fraction. The effective core volume fraction is defined as $\varphi(1+\delta/a)$.[3] Plotted are reduced viscosities for NIMs based on the M2070 canopy (■), the L300 canopy (●), and they EM C/25 canopy (▲). The lines is Brady's expression for the asymptotic prediction of hard sphere colloid behavior[10].

possible for the NIMs unit to have the shape of a sphere while at rest since η_o/μ diverges at $\varphi_m = 0.63$ but may take on a different shape during flow.

Normal Stress Differences

Normal stress differences are typically observed in elastic polymers where the diagonal components of the stress tensor have non-zero values. Normal stress differences are the usual culprits in polymer phenomena such as rod climbing, die swell, and the pressure drop in capillary flow entrance. Normal stress differences such as the first normal stress difference, N_1, and the second normal stress difference, N_2 are usually only observed in elastic materials, so Newtonian fluids which have a constant viscosity are expected to have $N_1 = N_2 = 0$. This is because Newtonian fluids have a shear rate independent viscosity and are purely liquid in nature. It is because of this that normal stress differences are unique to polymers and fluids which contain rods, or other anisotropic fillers where N_1 arises from the flow alignment and stretching of these fillers when subjected to a deformation. Typically, the first normal stress difference, N_1, is reported in the literature since it is easier to measure than the second normal stress difference. It has been reported in the literature that the addition of fillers to a polymer leads to a reduction of N_1[56, 63, 67, 69, 77, 105, 106]. One explanation for this effect has to do with filler-filler and filler-polymer interactions. When small fillers such as spherical nanoparticles are introduced into the polymer matrix, a synergistic interaction between the particle surface and polymer chain forms. As the concentration of fillers is increased, the filler-polymer interaction will further reduce the mobility of the polymer chains, leading to increased rigidity and hence a decrease of the first normal stress difference. Only anisotropic fillers, such as rods or fibers, can lead to increases in N_1 since they are caused by non-Newtonian stresses which arise from the microstructure of the suspension [106, 107]. There have been theoretical predictions of normal stress differences in colloidal suspensions where numerical

work has shown that N_1 is expected to be positive at very low Peclet numbers, but shifts to negative values at larger Peclet numbers[14]. It was shown numerically that because hard spheres do not deform or have a preferred flow direction, normal stress differences can only result from the spatial arrangements of the particles themselves. Because of the difficulty in measuring normal stress differences, there are very few reports of N_1 and N_2 for colloidal suspensions. In one such article, it was reported that in a shear thickening Boger fluid (a fluid composed of low concentrations of high molecular weight polymer dissolved in a viscous liquid), a suspension of micron sized polystyrene spheres did show a measurable N_1 which decreased with increasing core volume fraction[105]. In another report[76], it was shown that for non-Brownian suspensions both N_1 and N_2 were reported as being negative, with $|N_2| > |N_1|$, agreeing with numerical work[14].

In contrast with the reported literature on polymer nanocomposites and colloidal suspensions, NIMS show a positive N_1 which increases with core volume fraction. The manifestation of N_1 seemed to coincide with the onset of the non-Newtonian shear thinning observed in the flow curves. Figure 2.20, Figure 2.21, and Figure 2.22 show plots of N_1 as a function of shear stress for NIMS based on the M2070, L300, and EM C/25 canopies, respectively. In order to determine whether the measured N_1 was due to the inclusion of the cores or is a property of the canopy material itself, steady shear tests for rates up to $600s^{-1}$ were performed on the canopy. Even at these extremely high shear rates, the viscosity of the canopy material was Newtonian and showed no nonlinear shear effects such as shear thinning or shear thickening, indicating that the canopy shows pure liquid behavior with no normal stress differences. Hence, the measured N_1 is entirely due to the inclusion of the cores and seems to be a property unique to NIMs. This uniqueness is in part because N_1 results from inclusion of the cores, as opposed to polymer nanocomposites where N_1

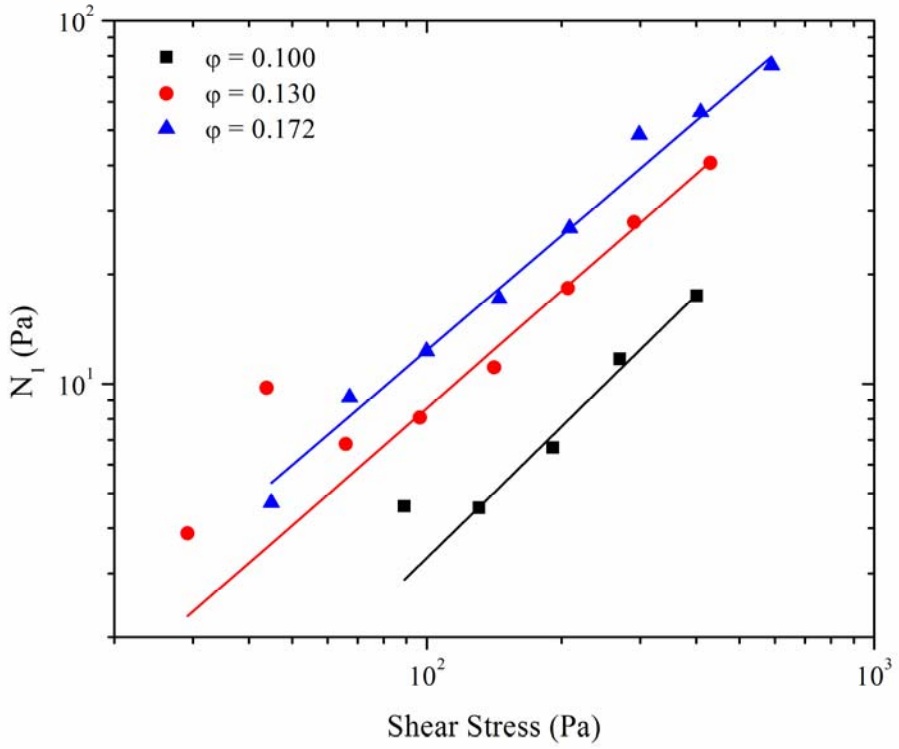

Figure 2.20 Plots of the first normal stress difference (N_1) as a function of applied shear stress for M2070-based NIMs. The lines are fit of equation (2.22).

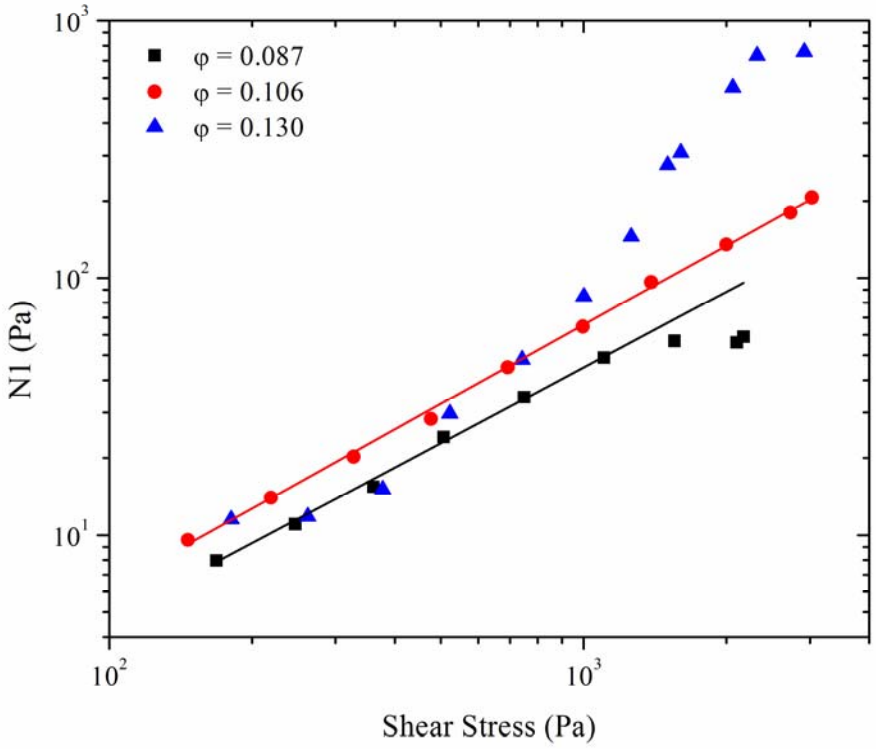

Figure 2.21 Plots of the first normal stress difference (N_1) as a function of applied shear stress for L300-based NIMs. The lines are fit of equation (2.22).

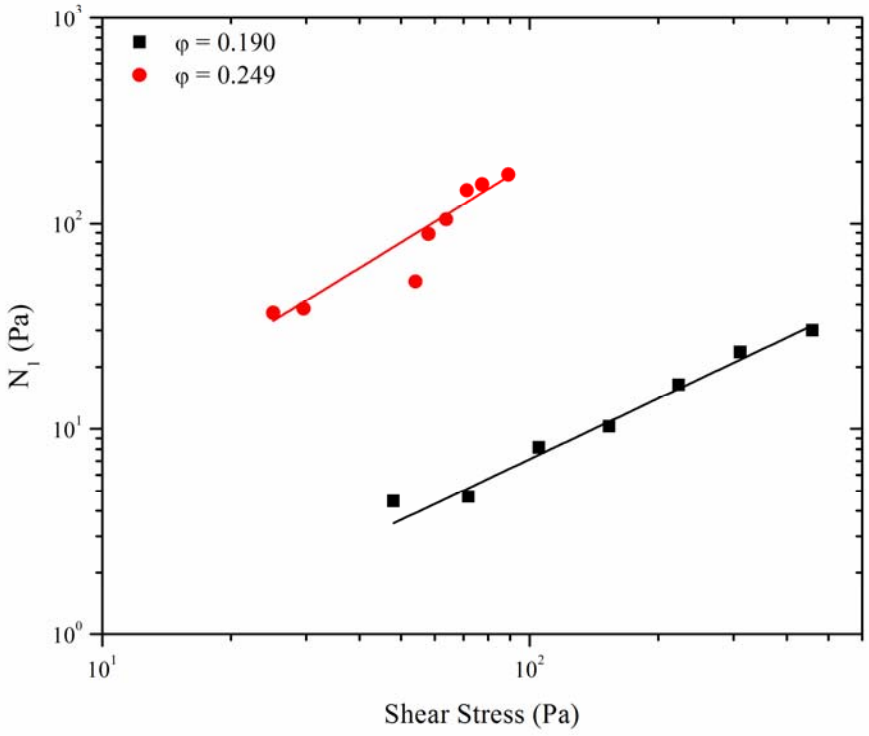

Figure 2.22 Plots of the first normal stress difference (N_1) as a function of applied shear stress for EM C/25-based NIMs. The lines are fit of equation (2.22).

weakens with the inclusion of filler. All the plots show that N_1 is positive and increases as the volume fraction of the cores is increased. The effect is stronger in M2070 and EM C/25-based NIMs where increases in core volume fraction show a clear increase in N_1 while in L300 NIMs, Figure 2.21 shows that N_1 does increase with core content, but seems to reach a maximum value at $\varphi = 0.13$. The magnitude and behavior of observed normal stress differences may be strongly dependent on the canopy molecular weight and chemistry. It is quite possible that the manifestation of normal stress differences is due to several factors. It could be due to the layering organization of the canopy molecules around the core particles, where the inner layers are strongly bound. As the particles are deformed during flow, these inner layers may be dragged along with the cores and may result in chain extension of the canopy molecules leading to the onset of N_1 due to the elasticity that will result from this extension. As was mentioned in the previous section, based on fits of $[\eta]$ it was found that the NIMs particles (core + canopy) may deform during flow resulting in a non-spherical shape. The onset of N_1 may also be due to the possible anisotropy in the NIMs particles and is consistent with previous literature showing that the inclusion of anisotropic fillers into polymer actually leads to increases of normal stress differences. Nevertheless, NIMs tend to show normal stress differences which strengthen with the inclusion of the cores, opposite of what is observed in polymer nanocomposites where N_1 is usually entirely due to the polymer matrix and addition of spherical fillers into the matrix leads to an overall reduction of the N_1. It is also inconsistent with colloidal suspensions, where at reasonable Peclet numbers N_1 is expected to be quite small and negative. N_1 was only measurable for systems with core volume fractions greater than $\varphi = 0.087$ where some non-Newtonian effects begin to manifest. Below these concentrations , all NIMs samples studied were completely Newtonian and displayed no elasticity.

Table 2.3 Parameters obtained from fitting equation (2.22) to the data in Figure 2.20, Figure 2.21, and Figure 2.22.

Sample	A(φ)	n
M2070: $\varphi = 0.100$	0.013	1.203
M2070: $\varphi = 0.130$	0.061	1.073
M2070: $\varphi = 0.172$	0.098	1.050
L300: $\varphi = 0.087$	0.053	0.977
L300: $\varphi = 0.106$	0.057	1.022
EM C/25: $\varphi = 0.190$	0.078	0.98
EM C/25: $\varphi = 0.249$	0.354	1.284

One way to quantify the strength of N_1 is to fit the data with a power law function of the form[63, 69]

$$N_1 = A(\varphi)\sigma^n \tag{2.22}$$

where $A(\varphi)$ is a core volume fraction dependent constant, σ is the applied shear stress, and n is a power law exponent which should be independent of core volume fraction. Table 2.3 lists the results of fitting equation (2.22) to the experimental data. The fits do show that $A(\varphi)$ does depend on the core volume fraction. In fact, for all the samples, $A(\varphi)$ increases with core volume fraction as expected from the form of equation (2.22). The effects of molecular weight can also be noted by comparing the value of $A(\varphi)$ for the M2070 $\varphi = 0.10$ and the L300 $\varphi = 0.106$ samples. Despite having very similar core concentrations, the L300-based NIMs samples yields an $A(\varphi)$ which is about four times larger than the M2070-based NIMs. The power law exponent from all fits also does not change by much for all samples studied, with

values in the range of $0.977 < n < 1.3$ obtained from the fits. These fits do help quantify the differences that arise from the molecular weights of the M2070 and L300 amines. The similarity of the power law exponent may point towards a universal range of expected values, with a power law very close to $n \sim 1$. EM C/25 NIMs seem to show a stronger increase in N_1 with increasing core volume fraction as observed from Figure 2.22, showing that the canopy architecture also seems to play a major role in this phenomenon. Table 2.3 also shows that $A(\varphi)$ increases much more than observed for the linear-based NIMs, but this can be argued by comparing the larger range of accessible volume fractions in the EM C/25-based systems. No definite theories as to why normal stress differences arise in NIMs yet exist, but this phenomena is interesting and warrants further investigations since it is possibly related to the NIMs model based on the layering and mobility of the canopy molecules.

Conclusions

In this chapter the rheological properties for NIMS based on three different canopy materials were presented. Oscillatory shear tests showed that NIMs show a gradual transition from simple liquid behavior to gel-like as the core volume fraction was increased. The range of dynamic behavior was found to strongly depend on the canopy architecture, with linear and tertiary amines showing different material characteristics at similar core volume fractions. Steady shear tests were also presented to study how NIMs respond to deformation. It was found that NIMs samples based on both the linear amines were quite Newtonian up to core volume fractions near the maximum packing density for NIMs ($\varphi_m \sim 0.19$ for the linear amines). No significant differences were observed in NIMs based on the linear amines especially since the molecular weight difference was not so large. NIMs based on the EM C/25 tertiary amine on the other hand showed characteristics not observed in the linear amines. For

example, at the maximum core volume fraction of $\varphi_m \sim 0.19$ where the viscosity of the linear amines diverges, NIMs based on EM C/25 were Newtonian and had a viscosity about four orders of magnitude smaller for equivalent core concentrations. The effects of core volume fraction were further probed by plotting the reduced viscosity as a function of core volume fraction. The data was then fit with the modified Krieger-Dougherty equation. From the results of the fit it was determined that the cores are effectively larger, containing contributions from both the corona and canopy. Upon further analysis which takes into account the size of the canopy, it was determined that the amine molecules are too large to pack tightly around the core particles, resulting in the canopy molecules residing in layers around the cores, with the inner layers more strongly bound then the outer ones. Finally, normal stress differences were measured in NIMs and increased in magnitude with increasing volume fraction, a trend which is opposite to what is observed in polymer nanocomposites. It also contrasts with colloidal suspensions where N_1 has been calculated and measured to be negative. Although no theories yet exist to explain the appearance of N_1, it may have to do with layering of the canopy around the cores.

The work presented in this chapter is only a small fraction of the rich science that exists in NIMs. The theories presented here are all based on observed experimental results, but future numerical work will be crucial to verify these interpretations of the data. The trends observed in the steady shear rheology presented in this chapter can hopefully serve as a reference point to predict the properties of future materials. Because of the hybrid nature of NIMs, they have a great potential for use in many important applications. As with any material, it is important to fully understand the fundamental properties of NIMs before any such use.

REFERENCES

[1] B. J. Ackerson, N. A. Clark, *Physical Review A* **1984**, *30*, 906.

[2] Z. Adamczyk, B. Jachimska, M. Kolasinska, *J. Colloid Interface Sci.* **2004**, *273*, 668.

[3] B. K. Aral, D. M. Kalyon, *J. Rheol.* **1997**, *41*, 599.

[4] Batchelo.Gk, *J. Fluid Mech.* **1970**, *41*, 545.

[5] G. K. Batchelor, *J. Fluid Mech.* **1977**, *83*, 97.

[6] J. W. Bender, N. J. Wagner, *J. Colloid Interface Sci.* **1995**, *172*, 171.

[7] B. Beresfordsmith, D. Y. C. Chan, *Faraday Discussions* **1983**, 65.

[8] J. Bergenholtz, J. F. Brady, M. Vicic, *J. Fluid Mech.* **2002**, *456*, 239.

[9] G. Bossis, J. F. Brady, *Journal of Chemical Physics* **1989**, *91*, 1866.

[10] J. F. Brady, *Journal of Chemical Physics* **1993**, *99*, 567.

[11] J. F. Brady, *Journal of Chemical Physics* **1993**, *98*, 3335.

[12] J. F. Brady, *Curr. Opin. Colloid Interface Sci.* **1996**, *1*, 472.

[13] J. F. Brady, A. S. Khair, M. Swaroop, *J. Fluid Mech.* **2006**, *554*, 109.

[14] J. F. Brady, M. Vicic, *J. Rheol.* **1995**, *39*, 545.

[15] R. Buscall, *Journal of the Chemical Society-Faraday Transactions* **1991**, *87*, 1365.

[16] R. Buscall, J. I. Mcgowan, A. J. Mortonjones, *J. Rheol.* **1993**, *37*, 621.

[17] B. Cabane, K. Wong, P. Lindner, F. Lafuma, *J. Rheol.* **1997**, *41*, 531.

[18] L. B. Chen, B. J. Ackerson, C. F. Zukoski, *J. Rheol.* **1994**, *38*, 193.

[19] L. B. Chen, M. K. Chow, B. J. Ackerson, C. F. Zukoski, *Langmuir* **1994**, *10*, 2817.

[20] M. Chen, W. B. Russel, *J. Colloid Interface Sci.* **1991**, *141*, 564.

[21] E. G. D. Cohen, R. Verberg, I. M. de Schepper, *Physica a-Statistical Mechanics and Its Applications* **1998**, *251*, 251.

[22] J. K. G. Dhont, G. Nagele, *Phys. Rev. E* **1998**, *58*, 7710.

[23] M. E. Fagan, C. F. Zukoski, *J. Rheol.* **1997**, *41*, 373.

[24] D. R. Foss, J. F. Brady, *J. Fluid Mech.* **2000**, *407*, 167.

[25] A. Imhof, A. Vanblaaderen, J. K. G. Dhont, *Langmuir* **1994**, *10*, 3477.

[26] R. B. Jones, P. N. Pusey, *Annual Review of Physical Chemistry* **1991**, *42*, 137.

[27] H. M. Lindsay, P. M. Chaikin, *Journal of Chemical Physics* **1982**, *76*, 3774.

[28] R. A. Lionberger, W. B. Russel, *J. Rheol.* **1994**, *38*, 1885.

[29] R. A. Lionberger, W. B. Russel, *J. Rheol.* **1997**, *41*, 399.

[30] J. Mellema, C. G. Dekruif, C. Blom, A. Vrij, *Rheologica Acta* **1987**, *26*, 40.

[31] A. Mourchid, A. Delville, J. Lambard, E. Lecolier, P. Levitz, *Langmuir* **1995**, *11*, 1942.

[32] G. Nagele, *Physics Reports-Review Section of Physics Letters* **1996**, *272*, 216.

[33] S. E. Phan, W. B. Russel, Z. D. Cheng, J. X. Zhu, P. M. Chaikin, J. H. Dunsmuir, R. H. Ottewill, *Phys. Rev. E* **1996**, *54*, 6633.

[34] T. N. Phung, J. F. Brady, G. Bossis, *J. Fluid Mech.* **1996**, *313*, 181.

[35] P. N. Pusey, P. N. Segre, O. P. Behrend, S. P. Meeker, W. C. K. Poon, *Physica A* **1997**, *235*, 1.

[36] W. B. Russel, *J. Fluid Mech.* **1978**, *85*, 209.

[37] W. B. Russel, *Annual Review of Fluid Mechanics* **1981**, *13*, 425.

[38] W. B. Russel, A. P. Gast, *Journal of Chemical Physics* **1986**, *84*, 1815.

[39] P. N. Segre, S. P. Meeker, P. N. Pusey, W. C. K. Poon, *Phys. Rev. Lett.* **1995**, *75*, 958.

[40] T. Shikata, D. S. Pearson, *J. Rheol.* **1994**, *38*, 601.

[41] J. J. Stickel, R. L. Powell, *Annual Review of Fluid Mechanics* **2005**, *37*, 129.

[42] B. Vandervorst, D. Vandenende, J. Mellema, *J. Rheol.* **1995**, *39*, 1183.

[43] J. C. Vanderwerff, C. G. Dekruif, *J. Rheol.* **1989**, *33*, 421.

[44] J. C. Vanderwerff, C. G. Dekruif, C. Blom, J. Mellema, *Physical Review A* **1989**, *39*, 795.

[45] H. Watanabe, M. L. Yao, K. Osaki, T. Shikata, H. Niwa, Y. Morishima, *Rheologica Acta* **1997**, *36*, 524.

[46] H. Watanabe, M. L. Yao, K. Osaki, T. Shikata, H. Niwa, Y. Morishima, *Rheologica Acta* **1999**, *38*, 2.

[47] H. Watanabe, M. L. Yao, K. Osaki, T. Shikata, H. Niwa, Y. Morishima, N. P. Balsara, H. Wang, *Rheologica Acta* **1998**, *37*, 1.

[48] H. Watanabe, M. L. Yao, A. Yamagishi, K. Osaki, T. Shitata, H. Niwa, Y. Morishima, *Rheologica Acta* **1996**, *35*, 433.

[49] D. R. Foss, J. F. Brady, *J. Rheol.* **2000**, *44*, 629.

[50] J.-P. Hansen, I. R. McDonald, *Theory of Simple Liquids*, Academic Press, New York **2006**.

[51] F. M. Du, R. C. Scogna, W. Zhou, S. Brand, J. E. Fischer, K. I. Winey, *Macromolecules* **2004**, *37*, 9048.

[52] V. Ganesan, V. Pryamitsyn, M. Surve, B. Narayanan, *J. Chem. Phys.* **2006**, *124*, 4.

[53] E. P. Giannelis, *Adv. Mater.* **1996**, *8*, 29.

[54] G. Havet, A. I. Isayev, *Rheol. Acta* **2001**, *40*, 570.

[55] G. Havet, A. I. Isayev, *Rheol. Acta* **2003**, *42*, 47.

[56] Y. H. Hyun, S. T. Lim, H. J. Choi, M. S. Jhon, *Macromolecules* **2001**, *34*, 8084.

[57] Y. W. Inn, S. Q. Wang, *Phys. Rev. Lett.* **1996**, *76*, 467.

[58] T. Kairn, P. J. Daivis, I. Ivanov, S. N. Bhattacharya, *J. Chem. Phys.* **2005**, *123*, 7.

[59] T. Kitano, T. Kataoka, T. Shirota, *Rheol. Acta* **1981**, *20*, 207.

[60] R. Krishnamoorti, E. P. Giannelis, *Macromolecules* **1997**, *30*, 4097.

[61] J. M. Kropka, K. W. Putz, V. Pryamitsyn, V. Ganesan, P. F. Green, *Macromolecules* **2007**, *40*, 5424.

[62] M. E. Mackay, T. T. Dao, A. Tuteja, D. L. Ho, B. Van Horn, H. C. Kim, C. J. Hawker, *Nat. Mater.* **2003**, *2*, 762.

[63] S. E. Mall-Gleissle, W. Gleissle, G. H. McKinley, H. Buggisch, *Rheol. Acta* **2002**, *41*, 61.

[64] A. B. Metzner, *J. Rheol.* **1985**, *29*, 739.

[65] N. Ohl, W. Gleissle, *J. Rheol.* **1993**, *37*, 381.

[66] M. A. Osman, A. Atallah, T. Schweizer, H. C. Ottinger, *J. Rheol.* **2004**, *48*, 1167.

[67] A. J. Poslinski, M. E. Ryan, R. K. Gupta, S. G. Seshadri, F. J. Frechette, *J. Rheol.* **1988**, *32*, 703.

[68] A. J. Poslinski, M. E. Ryan, R. K. Gupta, S. G. Seshadri, F. J. Frechette, *J. Rheol.* **1988**, *32*, 751.

[69] V. Pryamitsyn, V. Ganesan, *J. Rheol.* **2006**, *50*, 655.

[70] V. Pryamitsyn, V. Ganesan, *Macromolecules* **2006**, *39*, 844.

[71] J. S. Smith, D. Bedrov, G. D. Smith, *Compos. Sci. Technol.* **2003**, *63*, 1599.

[72] F. W. Starr, J. F. Douglas, S. C. Glotzer, *J. Chem. Phys.* **2003**, *119*, 1777.

[73] M. Surve, V. Pryamitsyn, V. Ganesan, *J. Chem. Phys.* **2006**, *125*, 12.

[74] M. Surve, V. Pryamitsyn, V. Ganesan, *Langmuir* **2006**, *22*, 969.

[75] A. Tuteja, M. E. Mackay, C. J. Hawker, B. Van Horn, *Macromolecules* **2005**, *38*, 8000.

[76] I. E. Zarraga, D. A. Hill, D. T. Leighton, *J. Rheol.* **2000**, *44*, 185.

[77] I. E. Zarraga, D. A. Hill, D. T. Leighton, *J. Rheol.* **2001**, *45*, 1065.

[78] Q. Zhang, L. A. Archer, *Langmuir* **2002**, *18*, 10435.

[79] E. P. Giannelis, *Appl. Organomet. Chem.* **1998**, *12*, 675.

[80] S. N. Bhattacharya, M. R. Kamal, R. K. Gupta, *Polymeric nanocomposites: theory and practice*, Carl Hanser Verlag, Munich **2008**.

[81] R. Gangopadhyay, A. De, *Chem. Mat.* **2000**, *12*, 608.

[82] F. Hussain, M. Hojjati, M. Okamoto, R. E. Gorga, *J. Compos Mater.* **2006**, *40*, 1511.

[83] J. Jordan, K. I. Jacob, R. Tannenbaum, M. A. Sharaf, I. Jasiuk, *Mater. Sci. Eng. A-Struct. Mater. Prop. Microstruct. Process.* **2005**, *393*, 1.

[84] R. Krishnamoorti, R. A. Vaia, E. P. Giannelis, *Chem. Mat.* **1996**, *8*, 1728.

[85] E. Manias, A. Touny, L. Wu, K. Strawhecker, B. Lu, T. C. Chung, *Chem. Mat.* **2001**, *13*, 3516.

[86] S. S. Ray, M. Okamoto, *Prog. Polym. Sci.* **2003**, *28*, 1539.

[87] K. Park, R. A. Vaia, *Adv. Mater.* **2008**, *20*, 3882.

[88] J. W. Gilman, *Applied Clay Science* **1999**, *15*, 31.

[89] J. W. Gilman, C. L. Jackson, A. B. Morgan, R. Harris, E. Manias, E. P. Giannelis, M. Wuthenow, D. Hilton, S. H. Phillips, *Chem. Mat.* **2000**, *12*, 1866.

[90] B. Serge, B. Michel Le, D. François, W. G. Jeffrey, K. Takashi, *Fire and Materials* **2000**, *24*, 201.

[91] P. C. Hiemenz, R. Rajagopalan, *Principles of colloid and surface chemistry*, Marcel Dekker, Inc, New York **1997**.

[92] L. N. Krishnamurthy, E. C. Weigert, N. J. Wagner, D. C. Boris, *J. Colloid Interface Sci.* **2004**, *280*, 264.

[93] Z. D. Cheng, J. X. Zhu, P. M. Chaikin, S. E. Phan, W. B. Russel, *Phys. Rev. E* **2002**, *65*.

[94] G. D. Scott, D. M. Kilgour, *J. Phys. D-Appl. Phys.* **1969**, *2*, 863.

[95] P. N. Pusey, W. Vanmegen, *Phys. Rev. Lett.* **1987**, *59*, 2083.

[96] P. F. Luckham, M. A. Ukeje, *J. Colloid Interface Sci.* **1999**, *220*, 347.

[97] R. G. Larson, *The Structure and Rheology of Complex Fluids*, Oxford University Press, New York **1999**.

[98] H. Lee, R. M. Venable, A. D. MacKerell, R. W. Pastor, *Biophys. J.* **2008**, *95*, 1590.

[99] M. L. Jespersen, P. A. Mirau, E. vonMeerwall, R. Rodriguez, E. P. Giannelis, R. A. Vaia, *ACS Nano* **2009 (In Preparation)**.

[100] C. El Moujahid, J. C. Ravey, V. Schmitt, M. J. Stebe, *Colloid Surf. A-Physicochem. Eng. Asp.* **1998**, *136*, 289.

[101] T. M. Kwon, M. S. Jhon, H. J. Choi, *J. Mol. Liq.* **1998**, *75*, 115.

[102] A. M. Wierenga, T. A. J. Lenstra, A. P. Philipse, *Colloid Surf. A-Physicochem. Eng. Asp.* **1998**, *134*, 359.

[103] A. M. Wierenga, A. P. Philipse, *Colloid Surf. A-Physicochem. Eng. Asp.* **1998**, *137*, 355.

[104] A. M. Wierenga, A. P. Philipse, *J. Colloid Interface Sci.* **1996**, *180*, 360.

[105] R. Scirocco, J. Vermant, J. Mewis, *J. Rheol.* **2005**, *49*, 551.

[106] S. A. Khan, R. K. Prudhomme, R. G. Larson, *Rheol. Acta* **1987**, *26*, 144.

[107] C. L. Tucker, P. Moldenaers, *Annu. Rev. Fluid Mech.* **2002**, *34*, 177.

CHAPTER 3: NIMS SCATTERING STUDIES

Introduction

The scattering of x-rays, neutrons, and light by matter is a widely used method to study the structure of materials[1-39]. This technique can probe several different length scales of a structure by simply varying the wavelength of the scattered radiation. For example, Figure 3.1 shows the range of length scales which are accessible from different types of scattering experiments such as small-angle x-ray and neutron scattering, ultra small-angle x-ray and neutron scattering, and conventional elastic light scattering[40]. By combining several different scattering techniques, it is possible to determine the structure or organization of particles dispersed in a solvent. This technique is so powerful and versatile that it has found uses in various fields of study such as biology, polymer science, and condensed matter physics[1, 5, 11, 22, 24, 25, 29, 32, 41].

The structure of materials at large length scales is fundamentally different than those on the atomic scale. At the atomic scale (sizes on the order of an *Å*), structures tend to have very high degrees of order. A simple example is salt which is an ionic crystal composed of Na^+ and Cl^- ions forming a regular, simple cubic lattice. X-ray scattering studies of salt would then yield a pattern with very sharp diffraction peaks

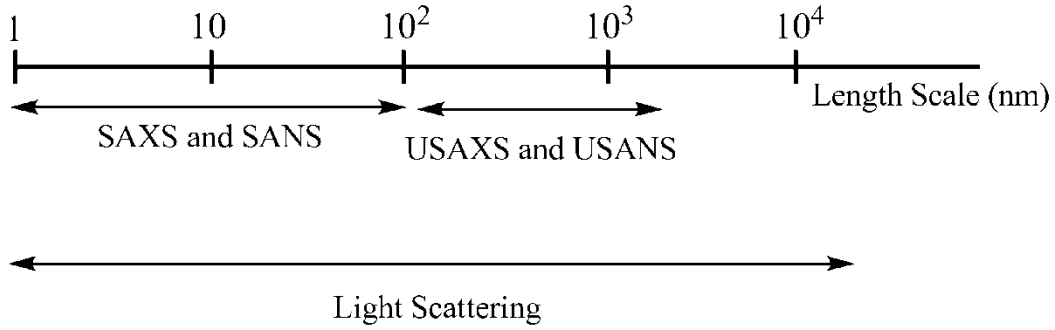

Figure 3.1 Range of length scales accessible from standard scattering techniques.

corresponding to the regular lattice formed by the ions in the crystal. On the other hand, matter is rarely well organized on larger length scales (sizes greater than 1nm). At such sizes the building blocks of any material can be quite complex and of different shapes. Another example could be a suspension of particles dispersed in a solvent. Individually, each particle may have a slightly different size and shape when compared to its neighbors. This irregularity will affect how the particles can pack together and how they will organize. Scattering studies of such systems would then yield a diffuse pattern with no sharp peaks due to the irregularity of the structure that is formed. The shape of this intensity pattern can be used to extract a great deal of information about the particles in solution[4, 6, 9, 11, 13, 18, 37, 38]. For example, one can measure the size and shape of the particles scattering the radiation, as well as information on the longer length scale microstructure amongst the particles themselves[1-3, 7-9, 12, 16, 19, 20, 22, 23, 26-29, 31, 32, 36]. Small-angle scattering is therefore a powerful technique to study the organization of matter on long length scales and use this information to get an idea as to the types and strength of interactions in a material[25, 27, 28, 32].

One of the most thoroughly studied systems using small-angle scattering is colloidal suspensions since they are considered as model systems in condensed matter physics[10, 14, 26-28, 34] and have even been considered to act as "big atoms"[24]. Just as important as answering basic science questions, colloids are critical in various applications that are important in everyday life. A few examples include uses in drugs, foods such as milk, everyday products such as toothpaste and paints[42]. For particles to be useful in any application colloid stability must be understood and it is determined by the interactions that exist in the system. Small-angle scattering is a very powerful technique to directly measure these interactions[25, 27, 28, 32, 36].

Small-angle Scattering from Colloids

The scattering of radiation from a suspension is strongly dependent on the scattering length difference between the solvent and particle and is determeined by the type of radiation used.[11, 14, 15, 19-21, 26-28, 34, 36, 38]. The scattering intensity from a suspension of particles, *I(q)* is given by[23, 27]:

$$I(q) = \varphi\,(\rho_c - \rho_s)^2\, V_c^2\, P(q)\, S(q) \tag{3.1}$$

where $q = (4\pi/\lambda)\sin\theta$ is the scattering vector, φ is the core volume fraction, ρ_c and ρ_s are the scattering length densities of the core and solvent, respectively, V_c is the volume of the core, *P(q)* is the particle form factor, and *S(q)* is the structure factor. The scattering length densities are strongly dependent on the type of radiation used, since x-rays and neutrons interact with matter differently. X-rays scatter from electrons while neutrons interact with the nuclei of atoms. The choice of scattering method then depends on the chemistry of the particles being studied. If one were studying a suspension of polymeric particles, neutron scattering would be the technique of choice while particles composed of silica would more strongly scatter x-rays because of its larger electron density. Equation (3.1) also shows that the scattering intensity depends on the concentration of scattering media as well as two other important parameters. *P(q)* is called the form factor and depends entirely on the size, shape, and polydispersity of the particle. The final term in equation (3.1) is called the structure factor, *S(q)*. The structure factor depends on the microstructure of the system which is in turn related to the interactions between particles. $S(q)$ is a direct measure of the types and strength of interactions that exist between particles. Scattering studies therefore provide a powerful platform to directly study the interactions in a system.

Since the cores used in the synthesis of NIMs are spherical nanoparticles, the analysis presented in this chapter will focus on scattering from spheres. The form factor for spherical particles is given by the following relation[41]

$$P(qR) = \left\{\frac{3[\sin qR - qR\cos qR]}{(qR)^3}\right\}^2. \tag{3.2}$$

Equation (3.2) assumes monodisperse particles which in reality is rarely true. The black line in Figure 3.2 is a plot of the form factor for a suspension of monodisperse spheres with a radius of gyration of 6.8nm. The plot shows an intensity pattern with very sharp valleys and well defined peaks, features which arise from the difference between the trigonometric functions in equation (3.2). The form factor must be modified to include polydispersity in order to model realistic suspensions. The red curve in Figure 3.2 shows the difference in the intensity patterns once polydispersity is included in the calculation. For this curve, a Gaussian size distribution was included in the calculation,

$$f(R) = \frac{1}{\sigma\sqrt{2\pi}}\exp\left[-\frac{1}{2\sigma^2}\left(R - R_{avg}\right)^2\right], \tag{3.3}$$

where R is the particle radius, σ is the polydispersity of spheres, and R_{avg} is the average core radius. To take into account the core polydispersity the scattered intensity must be averaged over all particle sizes present[15],

$$I(q) = \varphi\,(\rho_c - \rho_s)^2\,V_c^2\int_0^\infty P^2(qR)\,f(R)\,R^6\,dR. \tag{3.4}$$

The red curve in Figure 3.2 is calculated using equation (3.4) and shows that the polydispersity has the effect of smearing the sharp valleys and peaks in the intensity

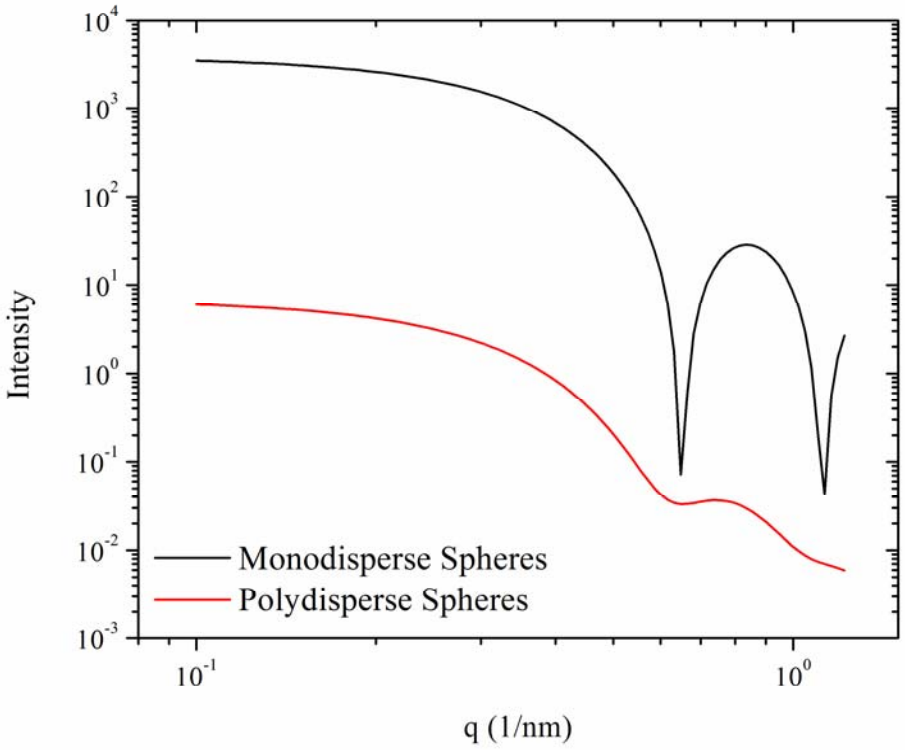

Figure 3.2 Plots of the form factor for spheres with a radius of gyration of R_g = 6.8nm. The black curve is the expected scattering pattern for monodisperse spheres, while the red curve is for the same spheres with a 14% polydispersity in the size distribution included in equations (3.3-4). Introducing polydispersity into a system has the effect of broadening the peaks and removing the sharp valleys of the form factor.

pattern. By measuring the scattering intensity pattern of a dilute dispersion of particles, one can actually measure the average size and polydispersity by fitting the curve with equation (3.4).

Equation (3.1) shows that the final term which determines the intensity pattern is the structure factor, *S(q)*. The structure factor arises from the core microstructure (how the particles are organized amongst themselves) and is a direct result of the interparticle interactions. *S(q)* tends to be stronger at higher core volume fractions which lead to stronger interactions while at very dilute concentrations *S(q)* can be small enough to become negligible in equation (3.1). The structure factor can be measured experimentally by taking the scattering pattern of suspensions at various core volume fractions ranging from very dilute where there are no interparticle interactions to the concentrated regime where *S(q)* will dominate the intensity pattern. Its presence is typically noted by the appearance of a peak in the intensity pattern. The structure factor can be extracted from experimental data by using[43],

$$S(q) = \frac{I(q)}{P(q)} \frac{\varphi_{P(q)}}{\varphi_{I(q)}} \tag{3.5}$$

where *I(q)* is the intensity pattern at high core volume fractions, P(q) is the measured form factor at very low core concentrations, $\varphi_{P(q)}$ is the volume fraction of the suspension with very low core concentrations, and $\varphi_{I(q)}$ is the volume fraction of the system with a higher concentration of cores. Once the structure factor is known it can be used to gain some insight into the types of interactions present in the system. The structure factor can be derived theoretically by taking the Fourier transform of the radial distribution, $g(r)$ which in turn is derived by solving the Ornstein-Zernike equation[17]. The radial distribution function is defined as the probability of finding a

particle *i* at a distance *r* from a second particle labeled *j*. The structure factor is defined as[44]

$$S(q) = 1 + \rho \int [g(r) - 1] e^{-i\boldsymbol{q}\cdot\boldsymbol{r}} d\boldsymbol{r}. \tag{3.6}$$

The difficulty of using equation (3.6) to calculate *S(q)* is finding *g(r)*. Calculation of *g(r)* requires knowledge of u*(r)*, the pair potential. There are several methods to perform this task which include direct simulation, a Virial expansion, or using an integral equation such as the Ornstein-Zernike equation (OZ)[13]

$$g(r) - 1 = c(r) + \rho \int c(|\boldsymbol{r} - \boldsymbol{x}|) h(\boldsymbol{x}) d\boldsymbol{x}. \tag{3.7}$$

where $h(r) = g(r) - 1$ is the total correlation function which is a measure of the total influence that one particle may have on another particle when the two are separated by a distance *r*, and $c(|\boldsymbol{r} - \boldsymbol{x}|)$ is the direct correlation function which is related to the direct interactions between particles. From the Ornstein-Zernike equation we see that the total correlation function is divided into two parts. The direct part is given by the direct correlation function *c(r)* which is due to two particles interacting directly. The indirect part is given by the integral term, where particle 1 may influence particle 3, which in turn may have an effect on particle 2. That is, particle 1 and particle 2 interact indirectly via particle 3. A "closure" relation is required to relate the *h* and *c* functions and the most commonly used relation is the Percus-Yevick equation. A complete derivation can be found in reference [45], but the basic idea is that $\rho g(r)$ is considered as the single particle density at the position $\boldsymbol{r}$ in the fluid when there is a particle of the system located at the origin, $\boldsymbol{r} = 0$. This assumes that the system is spatially uniform in the absence of the field. Once the field due to the particle at the

origin is turned on (this is the interaction potential), then it can be regarded as a perturbation and therefore able to use Taylor series expansions.

This derivation of the Percus-Yevick (PY) equation is based on the physical interpretation of the OZ equation[17, 44]. The OZ equation is a relation between *h(r)* and *c(r)*. If *c(r)* can be expressed in terms of *g(r)* or *h(r)* and substituted into the OZ equation, then this should give a closed integral equation for *h(r)*. Since the direct correlation function represents the direct interaction between two particles, it can be written as

$$c(r) = g_{total}(r) - g_{indirect}(r), \tag{3.8}$$

where $g_{total}(r)$ is the radial distribution function ($g(r) = \exp[-w(r)/kT]$, where $w(r)$ is the potential of mean force), and $g_{indirect}(r) = \exp[-(w(r)-u(r))/kt]$ is the radial distribution function with the direct interaction subtracted. Next the cavity distribution function $y(r)$ is defined as

$$y(r) = g(r)e^{-u(r)/kT}, \tag{3.9}$$

where $y(r)$ is a more slowly varying function than $g(r)$. Using the above relations, the direct correlation function may be written as

$$\begin{aligned} c(r) &= e^{-\frac{w(r)}{kT}} - e^{-\frac{w(r)}{kT}} e^{\frac{u(r)}{kT}} \\ &= g(r) - g(r)e^{\frac{u(r)}{kT}} \\ &= g(r) - y(r) \\ &= y(r)e^{-\frac{u(r)}{kT}} - y(r) \\ &= f(r)y(r) \end{aligned} \tag{3.10}$$

Plugging this into the OZ equation, and using the fact that $h(r) = g(r) - 1 = y(r)\exp(-u(r)/kT) - 1$ then gives the Percus-Yevick equation,

$$y(r) = 1 + \rho \int f(|\boldsymbol{r} - \boldsymbol{x}|) y(|\boldsymbol{r} - \boldsymbol{x}|) h(\boldsymbol{x}) d\boldsymbol{x}. \tag{3.11}$$

Assuming that $u(r)$ has the form of a hard sphere potential,

$$u(r) = \begin{cases} \infty, & r < d \\ 0, & r > d \end{cases} \tag{3.12}$$

where d is the particle diameter, then equation (3.11) can be solved analytically using Laplace transforms to give:

$$c(r) = \begin{cases} \dfrac{1}{(1-\varphi)^4}\left[\dfrac{3\varphi}{2}(2+\varphi)\dfrac{2r}{d} - (1+2\varphi)\left(1 + \dfrac{1}{2}\varphi\left(\dfrac{r}{d}\right)^3\right)\right], & r < d \\ 0, & r \geq 0 \end{cases} \tag{3.13}$$

Equation (3.13) shows that $c(r)$ only depends on the particle radius and the core volume fraction for hard spheres. To calculate the structure factor for a suspension of hard spheres, the Fourier transform of equation (3.13) must be taken,

$$c(q) = -4\pi \int c(r) r^2 \frac{\sin qr}{qr} dr. \tag{3.14}$$

Once $c(q)$ has been calculated the structure factor can be derived from the relation $S(q) = [1 - c(q)]^{-1}$. Figure 3.3 shows a plot of the structure factor for hard spheres at different sphere volume fractions. General features that can be observed in Figure 3.3 are that the peak in the structure factor moves to higher qR values and becomes stronger as the sphere volume fraction is increased. The first peak is related to the amount of local ordering present in the sample and the stronger it is, the more ordered

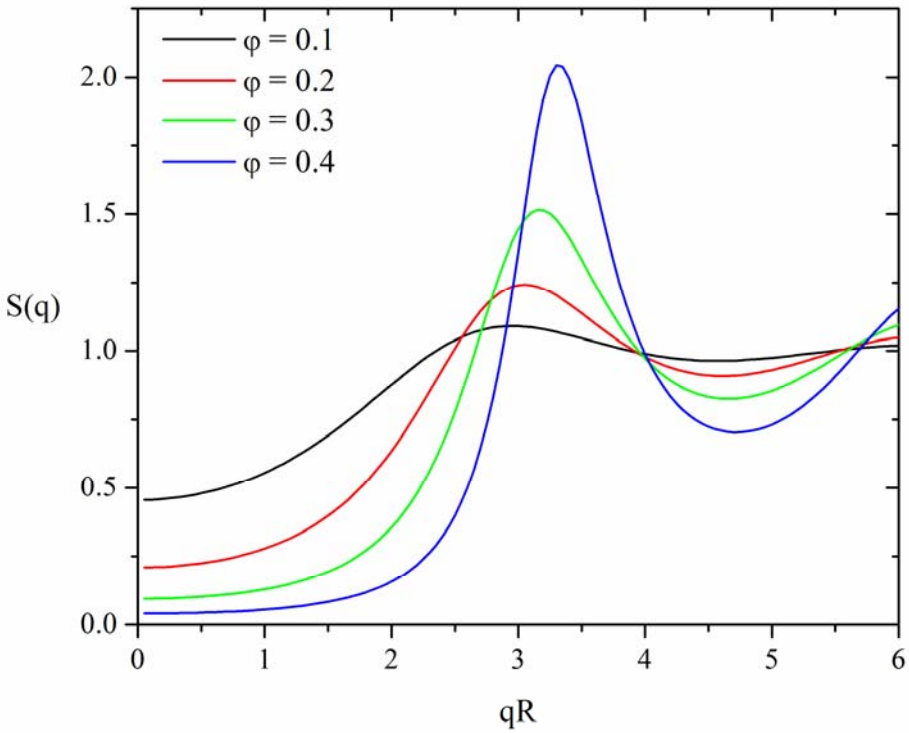

Figure 3.3 Calculated structure factors for hard sphere colloidal particles at different volume fractions. The functions are calculated using equation (3.14) and using the relation that $S(q) = [1 - c(q)]^{-1}$.

the sample. The plot of *S(q)* shows that as the packing fraction for hard spheres is increased, entropy drives the spheres to order into a lattice structure to maximize the free volume. From the rheological characterizations presented in the previous chapter it was shown that NIMs could be fairly well described by the Krieger-Dougherty equation with an extended layer thickness describing the effective radius of the particles. This chapter will extend theories developed for scattering studies of colloidal particles to study the interactions that exist in NIMs. The analysis in this chapter will focus on two models, the Gaussian model shown in equation (3.4) and the polydisperse Hard Sphere model derived in equations (3.6-14).

Experimental

Small-Angle X-Ray Scattering Studies

All samples were dried in vacuum for 24h at 35°C before x-ray scattering measurements. SAXS measurements were taken at the Cornell High Energy Synchrotron Source (CHESS, D-Line) by loading the samples into a plate with a hole cut out. The diameter of the hole was about 0.2mm and a schematic is shown in Figure 3.4. One side of the hole was covered with kapton tape and the sample was loaded into the hole then covered with more kapton tape to keep the sample from leaking out. The plate was loaded onto the sample holder and aligned with the center of the beam. The sample to detector distance was set to 1.8m and exposure times varied between 0.5-1s, depending on the degree of scattering. The scattering images were integrated using Fit2D to extract the raw intensity versus wavenumber data. The data was then fit with various models using a small-angle scattering package put together by the National Center for Neutron Research (NCNR)[15].

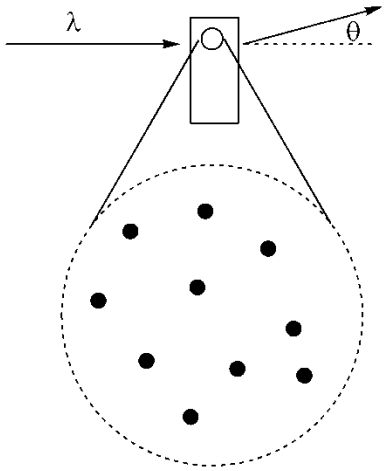

Figure 3.4 Schematic of experimental setup used in SAXS studies.

Results and Discussion

NIMs Scattering Results

Figure 3.5, Figure 3.6, and Figure 3.7 show the intensity data for NIMs based on the M2070, L300, and EM C/25 amines. All the data are shifted vertically for simpler viewing. Focusing first on NIMs based on the M2070 canopy shows that the shape of the intensity pattern does not seem to change with increasing core concentration. For the lowest concentration measured, $\varphi = 0.012$, the pattern appears just like that for a dilute dispersions of spheres[11, 13, 18-20, 23, 27, 36]. Increasing the core concentration does not seem to significantly alter the shape of the curve for the low q range, but the peak at the higher q range ($q \sim 0.65\text{nm}^{-1}$) appears to get stronger with concentration. For L300-based NIMs, Figure 3.6 shows that the slight increase in the canopy molecular weight does appear to have an effect on the pattern. The intensity patterns for $\varphi < 0.192$ has the appearance of a dilute dispersion of particles just as was observed for M2070-based NIMs. For core concentrations with $\varphi > 0.293$, L300 NIMs start to show deviations from dilute dispersion and although weak, begin to show the effects of the structure factor while M2070 NIMs still retain the appearance

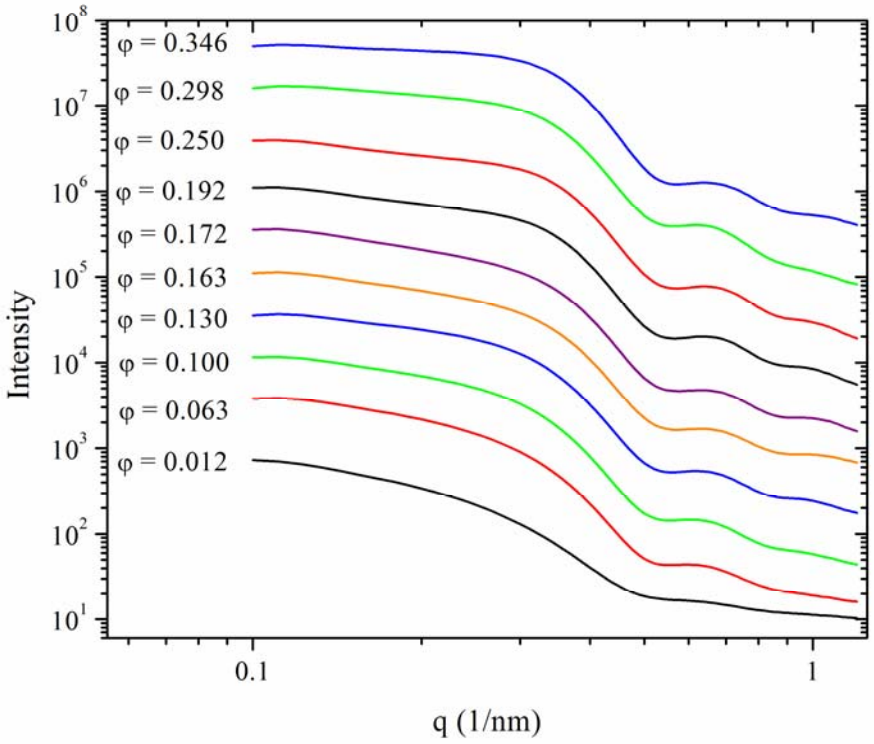

Figure 3.5 SAXS intensity patterns for M2070-based NIMs. The curves have been shifted vertically for easier viewing.

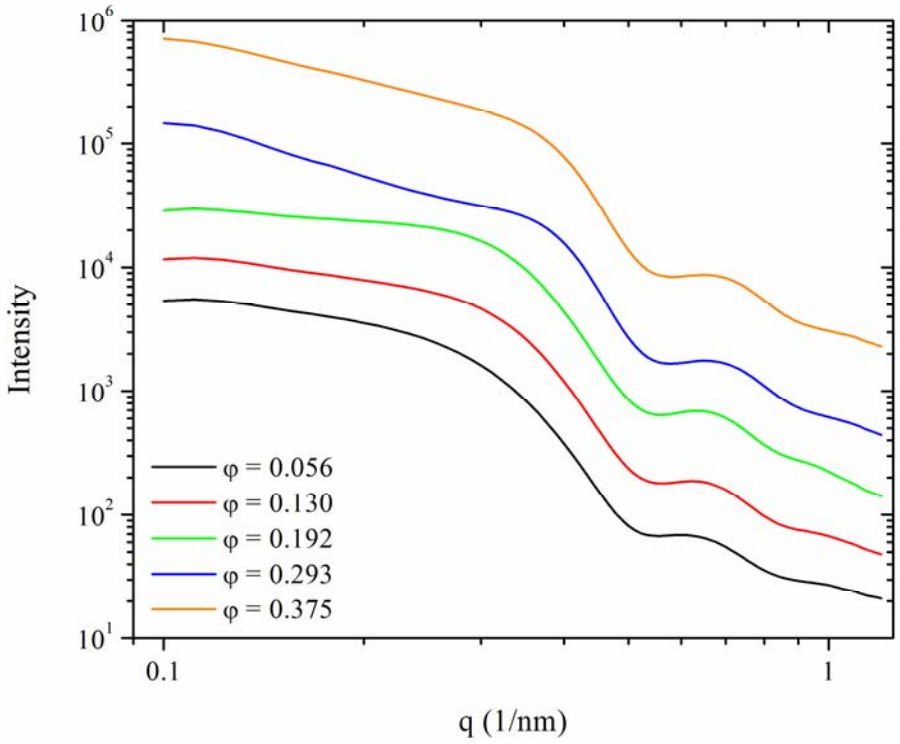

Figure 3.6 SAXS intensity patterns for L300-based NIMs. The curves have been shifted vertically for easier viewing.

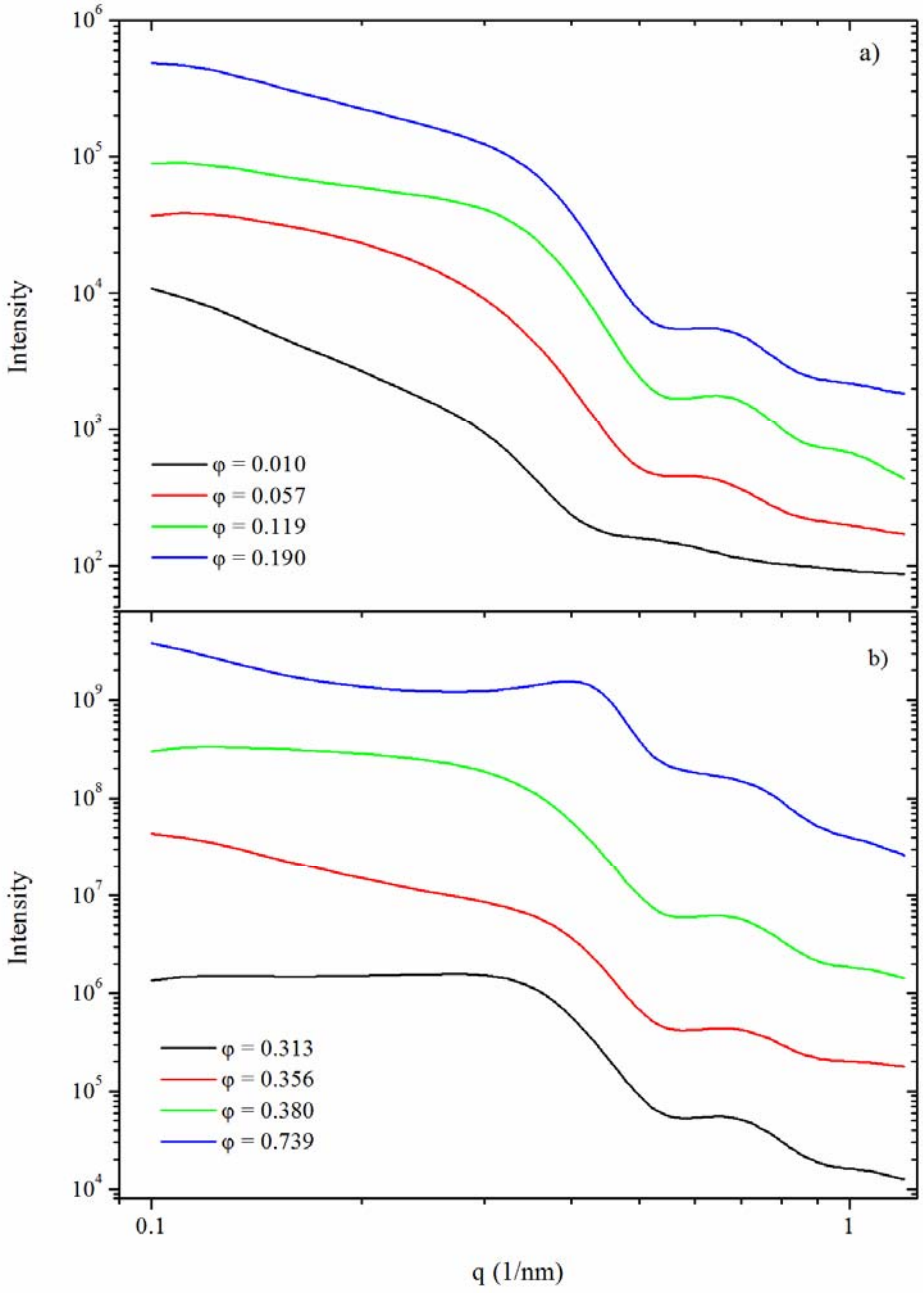

Figure 3.7 SAXS intensity patterns for EM C/25-based NIMs. The curves have been shifted vertically for easier viewing.

of dilute spheres. Above these concentrations the interactions between the particles start to slightly affect the observed microstructure. It is surprising that NIMs scattering patterns for the linear amines have the appearance of dilute suspensions of spheres at $\varphi \sim 0.19$ while the rheology shows a system with a viscosity that diverges, indicating that the microstructure does not control the rheology. Figure 3.7 shows that EM C/25-based NIMs also show similar behavior as the L300 NIMs. For core concentrations below $\varphi = 0.19$, EM C/25 NIMs also have the shape due to a dilute dispersion of spheres. Above this core concentration the effects of the structure factor begin to set in. From these results and the rheology presented in Chapther 2, $\varphi \sim 0.19$ seems to be a critical concentration for NIMs, both structurally and rheologically despite having no correlation with the stoichiometric NIMs transition.

As was stated in the previous section, x-ray scattering studies can be used to extract information on the shape and size of the cores. At very low scattering angles x-ray scattering data can be plotted and analyzed using the Guinier equation:

$$I(q) = I(0)\exp(-q^2 R_g^2/3) \tag{3.15}$$

where R_g is the radius of gyration of the particles. The accuracy of this equation requires data at very low q values ($q \rightarrow 0$). Interparticle interactions may also significantly affect the accuracy of the data at low q, so only samples with very dilute concentrations of particles can be analyzed with this equation[41]. Any polydispersity in the particle size distribution can also significantly affect the Guinier plot and can be observed if several of the points in the low q range deviate from a straight line[41]. Taking the natural logarithm of both sides of equation (3.15) gives

$$\ln I(q) = I(0) - q^2 R_g^2/3. \tag{3.16}$$

Plotting the ln[$I(q)$] versus q^2 should therefore yield a straight line, the slope of which gives the radius of gyration for the particles. The geometric radius of a sphere can be calculated using equation (2.18) once the radius of gyration is known.

Figure 3.8 is a Guinier plot for the $\varphi = 0.012$ M2070 and $\varphi = 0.010$ EM C/25 samples. Fitting the M2070 NIMs sample with a straight line yields a radius of gyration of $R_g = 7.6$nm which translates to a geometric radius of $R = 9.8$nm. A similar fit to the EM C/25 NIMs sample yields $R_g = 7.9$nm and a geometric radius of $R = 10.2$nm. Since x-rays scatter from matter with large electron densities, this means that the x-rays are seeing not only the core but the corona as well since the sulfonic acid groups are just as electron rich as the silica core. This can explain why the geometric radius extracted from the Guinier plots is larger than the bare core radius of $R_{core} = 8.9$nm obtained from transmission electron microscopy. Estimates of the corona thickness around each core is about 0.5nm in thickness, adding this to the core radius yields an effective x-ray core radius of $R_{SAXS} = 9.4$nm. Although this value is close to what is extracted from the Guinier plots, the geometric radius is still smaller. As was mentioned before the accuracy of any radii values extracted is strongly dependent on the q range accessible, and these experiments may not have accessed a low enough range for an accurate measurement. The particle polydispersity and interparticle interactions also appear to be affecting the Guinier plot as can be noted by the deviation of the data from the linear fit for q^2 range below 0.025nm^{-2}. These fits show that the contribution of the corona to the effective particle radius must be taken into account when performing x-ray scattering analysis. To prove that the corona is also contributing to the scattering and hence yielding a larger core size, the intensity pattern for a dilute dispersion of unfunctionalized silica particles in water was measured. Figure 3.9 shows a Guinier plot of the bare silica cores along with a linear fit. The fit yields a radius of gyration of $R_g = 6.9$nm, which gives a geometric radius

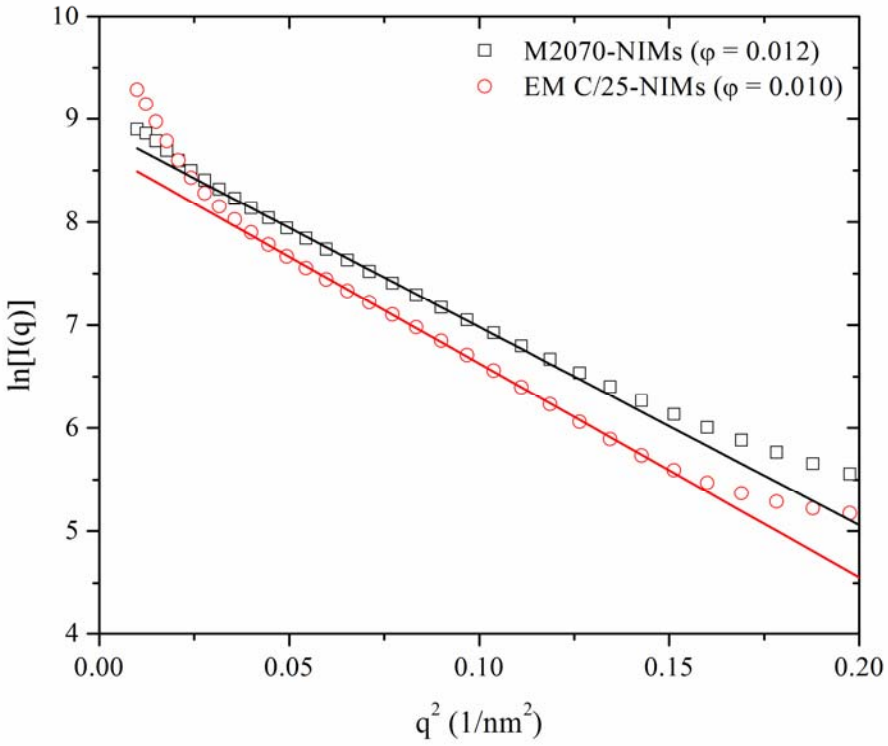

Figure 3.8 Guinier plots for the lowest core volume fraction NIMs samples based on the M2070 and EM C/25 canopies. The lines are least-squares fits used to extract the radius of gyration using equation (3.16).

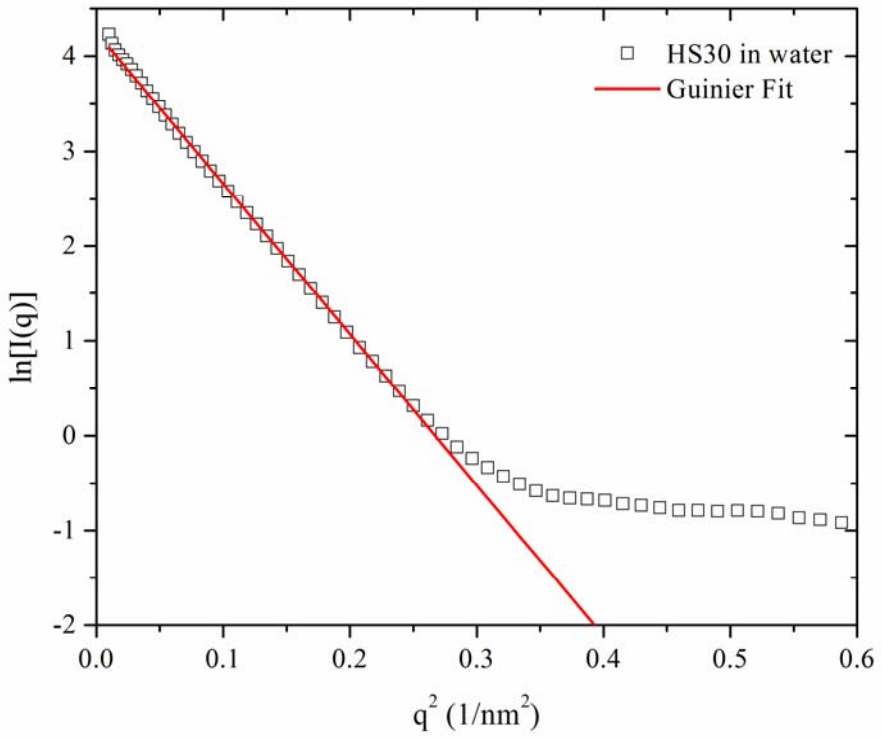

Figure 3.9 Guinier plots for the bare, unmodified silica particles dispersed in water at a concentration of $\varphi = 0.02$. The lines are least-squares fits used to extract the radius of gyration using equation (3.16).

of R = 8.9nm, an identical value to what was obtained from TEM analysis. This proves that during the scattering tests, both the core and corona are scattering x-rays as a single unit and hence an effective volume fraction must be calculated to include the corona thickness. Further evidence comes from the difference in scattering length densities between the silica cores and sulfonic acid silane, which is $\Delta\rho \sim 0.05\times10^{-5}$Å^{-2}. This value is so small that the core and corona cannot be distinguished using x-rays. The effective x-ray scattering unit in these tests is the core and corona. The next two sections will present the fitting results for the experimental scattering data with two models that lie at opposite extremes with respect to interparticle interactions. The first model presented is a Gaussian sphere model (no interactions) and the second is a polydisperse Hard Sphere model (Hard Sphere interactions).

Gaussian Model Fits

The first model used to fit the experimental scattering data was based on a polydisperse suspension of spheres with a Gaussian size distribution. The model is based on equations (3.3-4) and is fit by a scattering analysis program provided by the NCNR[15]. This model assumes no other interactions between particles and thus lies at the extreme where particles do not see each other in suspension. Figure 3.10, Figure 3.11, and Figure 3.12 show the intensity plots for M2070, L300, and EM C/25 NIMs along with fits of the Gaussian model (black lines). This model used the effective volume fraction which includes the contribution from the corona thickness.

In Figure 3.10 the experimental SAXS data for NIMs based on the M2070 canopy is plotted along with fits of the Gaussian model. The model does appear to adequately fit the φ = 0.012 data throughout the entire q range measured. At such a low concentration of cores it is expected that there be no significant interactions between the cores. The excess amine therefore serves as an extra fluidization medium

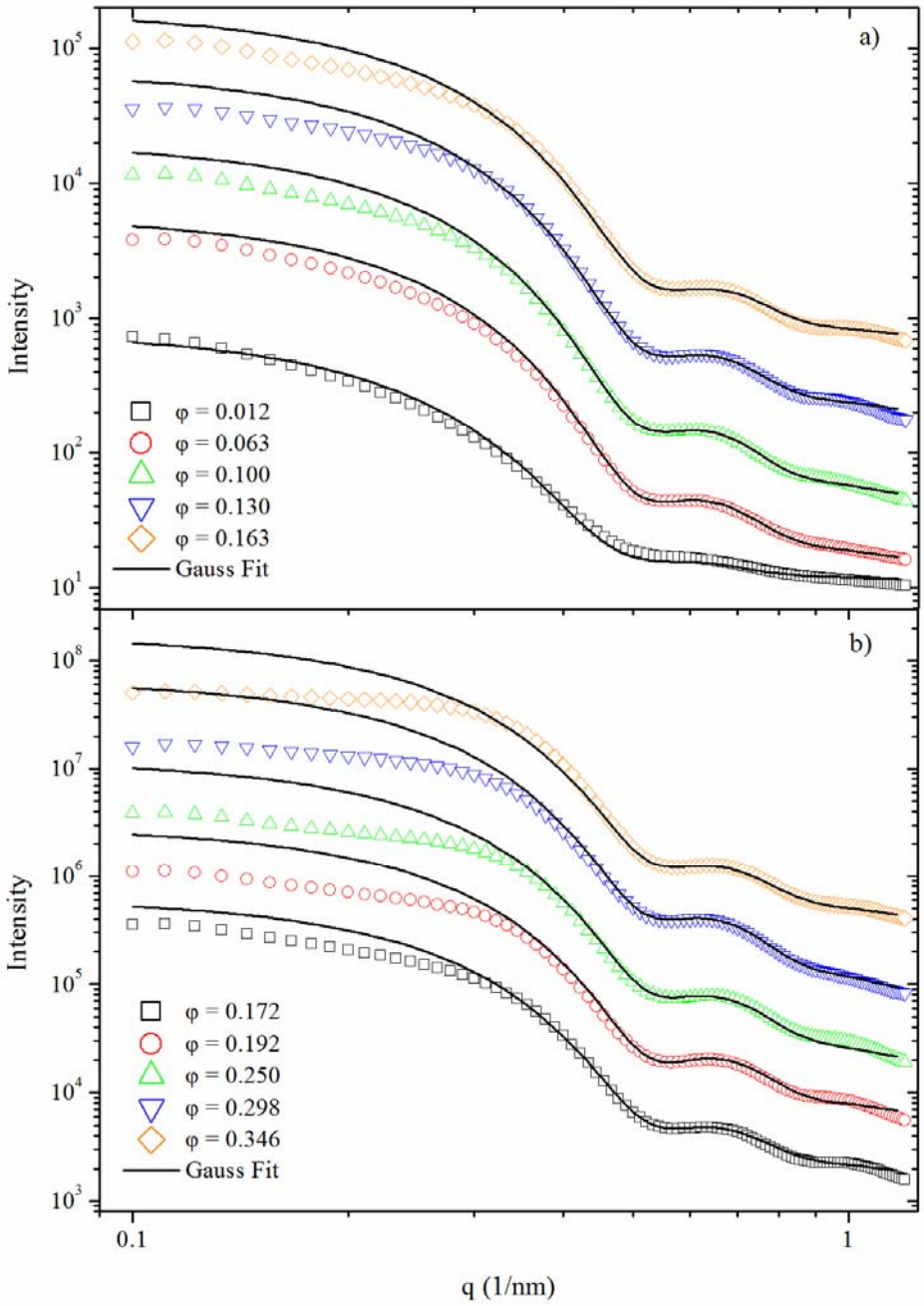

Figure 3.10 Plots of the scattered intensity for M2070-based NIMs. The lines are fits of a Gaussian model which assumes no interparticle interactions and only depends on the core shape and polydispsersity.

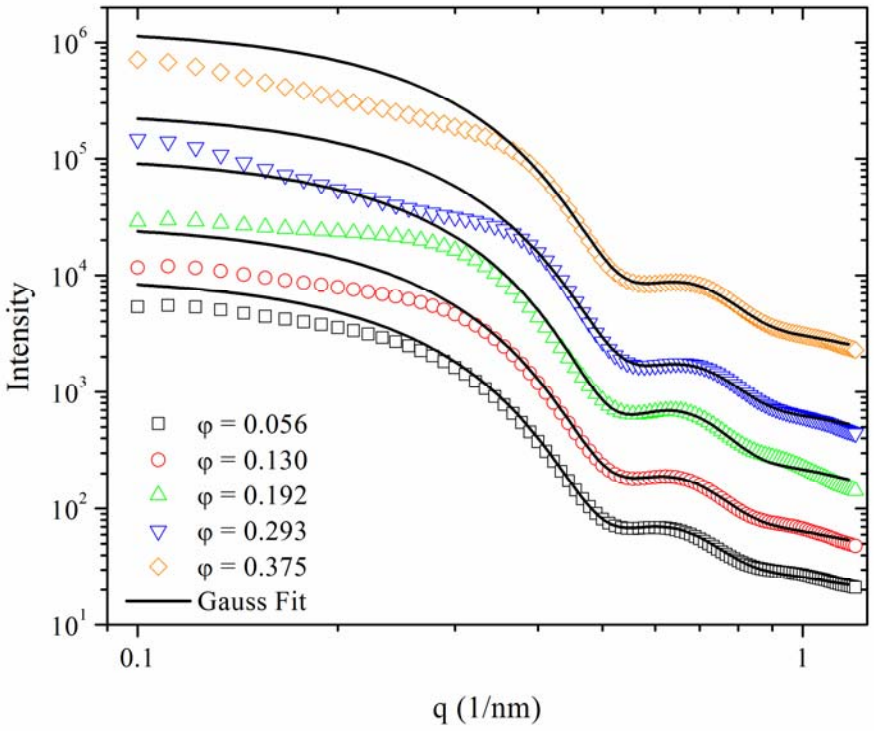

Figure 3.11 Plots of the scattered intensity for L300-based NIMs. The lines are fits of a Gaussian model which assumes no interparticle interactions and only depends on the core shape and polydispsersity.

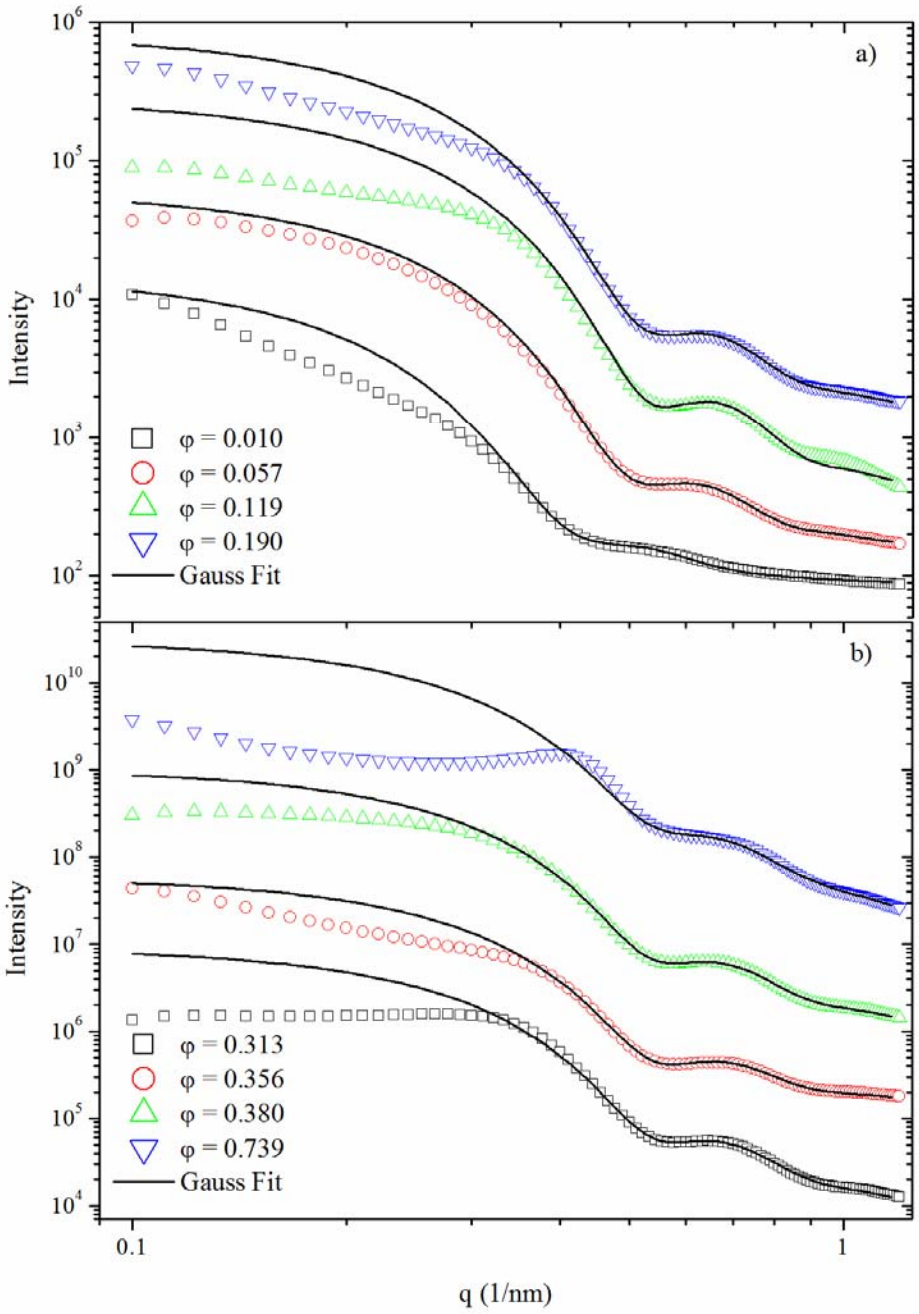

Figure 3.12 Plots of the scattered intensity for EM C/25-based NIMs. The lines are fits of a Gaussian model which assumes no interparticle interactions and only depends on the core shape and polydispsersity.

Table 3.1 Parameters used to fit the Gaussian model to M2070-based NIMs shown in Figure 3.10. R_g is the radius of gyration of the core and corona, R the geometric radius calculated using equation (2.18), and Δ is the polydispersity of the particles.

φ	R_{geff} (nm)	R_{eff} (nm)	Δ
0.012	8.2	10. 6	0.17
0.063	8.24	10.6	0.15
0.100	8.25	10.7	0.15
0.130	8.13	10.5	0.15
0.163	7.95	10. 3	0.15
0.172	7.95	10. 3	0.15
0.192	8.1	10.5	0.14
0.250	7.99	10.3	0.15
0.298	8.12	10.5	0.15
0.346	7.92	10.2	0.15

which results in greater particle separations. The model starts to deviate slightly for the next sample with a core volume fraction of $\varphi = 0.063$. Here, the model does fit the high q range, which contains information on the core size and polydispersity but begins to deviate slightly in the low q range where interparticle interactions become significant. Figure 3.10 shows that the fits for consecutively higher core volume fractions appear to deviate much more as the interparticle interactions become stronger. For all the data fit, the Gaussian model does capture the information from the size of the cores and polydispersity. This can be seen by the success of the model to fit the high q data at ranges $q > 0.35\text{nm}^{-1}$. Calculation of the length scale at this q range yields a value of about 18nm, indicating that there are interactions for distances greater than the size of the particles. The parameters varied during the fit are the radius of gyration of the core and corona, $R_{g,eff}$, and the polydispersity of the cores, Δ. Table 3.1 lists the results of the parameters obtained from the fits of the data in Figure

Table 3.2 Parameters used to fit the Gaussian model to L300-based NIMs shown in Figure 3.11. R_g is the radius of gyration of the core and corona, R the geometric radius calculated using equation (2.18), and Δ is the polydispersity of the particles.

φ	R_{geff} (nm)	R_{eff} (nm)	Δ
0.056	8.28	10.7	0.15
0.130	8.13	10.5	0.15
0.192	8.16	10.5	0.14
0.293	7.78	10.0	0.15
0.375	7.81	10.0	0.15

3.10. Listed in Table 3.1 are the core volume fraction, φ, the effective radius of gyration, $R_{g,eff}$, the effective radius, R_{eff}, and the polydispersity of the cores, Δ. Because the electron scattering length difference between the core and corona are so small ($\Delta\rho \sim 0.05\times10^{-5}$Å^{-2}) there is not enough contrast difference to distinguish between these two components. In SAXS studies the effective unit which scatters x-rays is the core and surrounding corona layer, so the extracted radius of gyration will be due to the sums of the core and corona. Table 3.1 shows that the measured polydispersity of the core particles has a value of $\Delta = 0.15$, quite close to what is measured from dynamic light scattering and TEM studies. The fits also yield an average radius of 10.2nm, values which are close to the value obtained from the Guinier plots shown previously.

In Figure 3.11 the intensity patterns and Gaussian model fits for L300-based NIMs are shown. This figure shows similar trends as displayed by the M2070 NIMs where the model does adequately fit the high q range which contains information on the polydispersity and size of the cores. In the range $q < 0.35$nm^{-1}, the model deviates from the experimental data, with the deviation getting stronger as the core volume geometric core radii which are very close to each other, having an average value of

Table 3.3 Parameters used to fit the Gaussian model to EM C/25-based NIMs shown in Figure 3.12. R_g is the radius of gyration of the core and corona, R the geometric radius calculated using equation (2.18), and Δ is the polydispersity of the particles.

φ	R_{geff} (nm)	R_{eff} (nm)	Δ
0.010	9.64	12.4	0.18
0.057	8.38	10.8	0.15
0.119	8.02	10. 4	0.14
0.190	8.06	10.4	0.15
0.313	7.83	10.1	0.15
0.356	7.82	10.1	0.14
0.380	7.86	10.1	0.15
0.604	7.65	10.0	0.178

$R_{M2070\text{-}NIMs}$ = 10.5nm. The Guinier plots in the previous section yielded radii of 9.8nm fraction is increased. This again is due to the fact that the model does not take into account interparticle interactions. Table 3.2 lists the fit parameters obtained from Figure 3.11. Taking the average of the radius from the Gaussian fits of the L300-NIMs gives a value of $R_{L300\text{-}NIMs}$ = 10.4nm which is close to the $R_{M2070\text{-}NIMs}$ = 10.5 value obtained from the M2070-NIMs fits. In Figure 3.12 the scattering data is plotted for EM C/25 NIMs along with the Gaussian fits and Table 3.3 lists the fitting parameters. Unlike the low concentration M2070-NIMs sample, the Gaussian model does not completely fit the low concentration EM C/25 sample (φ = 0.010). The scattering studies, just like the rheology, seem to show a fairly strong dependence on the canopy architecture which may have a strong influence on the interparticle interactions. As was observed for the M2070 and L300-based NIMs, the Gaussian model does not fit the low q range of the EM C/25 NIMs samples where interparticle interactions tend to dominate. The model does capture the core size and

polydispersity as seen by the success of the model in the high q range. Again, analyzing the average size of the scattering particles shown in Table 3.3 yields an average of $R_{EM\ C/25\text{-}NIMs}$ = 10.6nm which is also close to the values obtained from fits of the M2070 and L300-based NIMs.

Fits of the Gaussian model do capture the size features of the scattering particles. Analyzing of the size and taking into account the scattering length densities of the core and corona shows that both components are contributing to the x-ray scattering pattern. Since the model assumes no interparticle interactions it does not capture the intensity pattern features in the low q range which indicates the presence of other interparticle interactions between the cores in NIMs.

Polydisperse Hard Sphere Model Fits

The only other model which offers an exact solution is the hard sphere model presented previously in this chapter. Equation (3.12) presents the hard sphere potential where no interactions between particles exist except on contact where an infinite repulsion sets in. This model may more accurately describe the dynamics in NIMs if the model of the NIMs unit presented in the previous chapter which consists of the core particle, corona layer, and the monolayer of canopy molecules surrounding the core is considered. The surrounding layer will then serve as a brush which prevents aggregation of the particles. The only complication arises from the outer canopy molecules which are not strongly bound to the corona layer. It is possible that the dynamic exchange that exists between these outer canopy molecules may also contribute to the interparticle interactions. The model used in this analysis was part of an analysis package provided by the NCNR and is an exact, multicomponent solution using the Percus-Yevick closure, equation (3.11).

In Figure 3.13 the scattered intensity curves for M2070-NIMs are plotted along with the results of fitting the polydisperse hard sphere model and Table 3.4 lists the parameters obtained from the fits. The polydisperse hard sphere (PHS) model does satisfactorily fit the experimental data for low core concentrations, $\varphi < 0.063$. At these low concentrations there is an excess of amine molecules present and the system may exhibit behavior close to what is expected for a suspension of hard spheres. If the model based on the rheological results of the previous section is correct, then the NIMs unit which consists of the core, corona, and inner layer of canopy molecules are all floating in a sea of excess canopy. The NIMs unit then behaves as a hard sphere when it comes into contact with other units at these low concentrations. At core concentrations $\varphi > 0.100$ the PHS model begins to underestimate the experimental data, indicating that at larger concentrations hard sphere dynamics no longer apply. As the concentration of the cores is increased for M2070-based NIMs, the intensity pattern does not seem to change much, retaining its appearance of a dilute dispersion of spheres. At volume fractions $\varphi > 0.192$, the PHS model predicts the onset of a structure factor peak which shifts to lower q values. NIMs do not appear to follow this pattern since no structure peak appears with increasing φ. Table 3.4 also shows that the values of the effective core radius obtained from the fits is very similar to the value obtained from the Gaussian model, $R_{M2070\text{-}NIMs}(PHS) = 10.6$nm.

In Figure 3.14 plots for L300-based NIMs are shown along with fits of the PHS model, and Table 3.5 lists the fit parameters obtained from the model. Just like the M2070-based NIMs the PHS model does fit L300-based NIMs at low core concentrations. The fits are satisfactory up to $\varphi = 0.192$ where the model underestimates the experimental data and begins to predict a structure factor peak. At

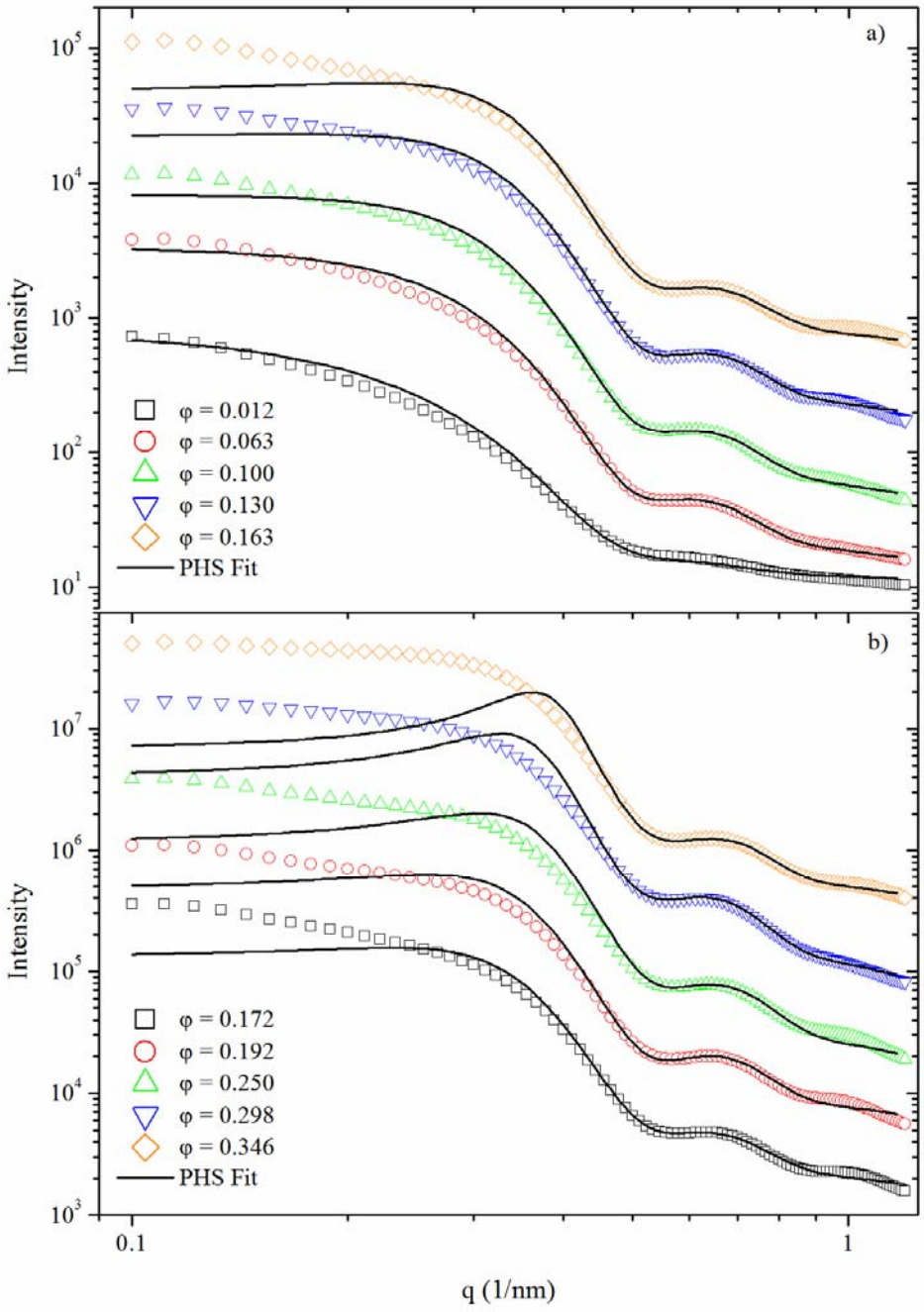

Figure 3.13 Plots of the scattered intensity for M2070-based NIMs. The lines are fits of a polydisperse hard sphere model based on the potential in equation (3.11). This model assumes no interactions except for an infinite potential repulsion on contact.

Table 3.4 Parameters used to fit the polydiserse Hard Sphere model to M2070-based NIMs shown in Figure 3.13. R_g is the radius of gyration of the core and corona, R the geometric radius calculated using equation (2.18), and Δ is the polydispersity of the particles.

φ	R_{geff} (nm)	R_{eff} (nm)	Δ
0.012	8.15	10.5	0.180
0.063	8.43	10.9	0.145
0.100	8.34	10.8	0.145
0.130	8.24	10.6	0.140
0.163	8.14	10.5	0.145
0.172	8.12	10.5	0.150
0.192	8.18	10.6	0.133
0.250	8.11	10.5	0.138
0.298	8.37	10.8	0.140
0.346	8.16	10.5	0.140

the highest core concentration of $\varphi = 0.375$ the PHS model predicts a well defined structure factor peak which does not appear in the experimental data. Instead the data appears to continue increasing as $q \rightarrow 0$, indicating the presence of other interparticle interactions. This model, like the Gaussian model, does capture the high q range which is due to scattering from the core. Figure 3.15 is a plot of the tertiary amine-based NIMs, the PHS model fails to fit the low q range for higher core volume fractions. The model also predicts a structure factor peak which does not exist in the scattering patterns except at the highest core concentration measured, $\varphi = 0.739$.

Comparison of the Gaussian and Polydisperse Hard Sphere Models

The results of fitting both models to the experimental scattering results are presented in this section. Plotted in Figure 3.16, Figure 3.17, and Figure 3.18 are the

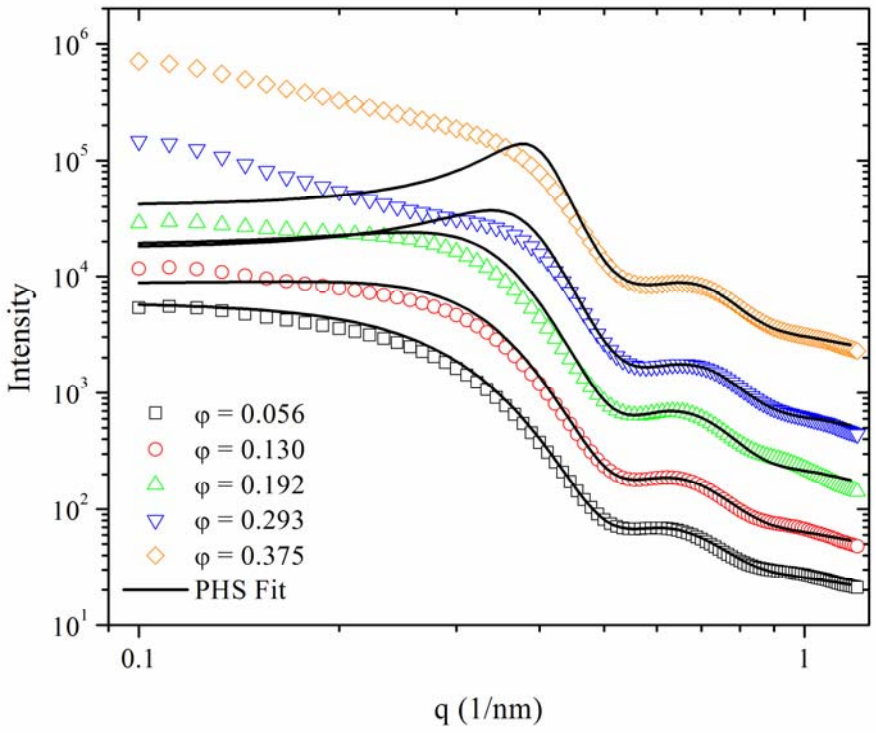

Figure 3.14 Plots of the scattered intensity for L300-based NIMs. The lines are fits of a polydisperse hard sphere model based on the potential in equation (3.11). This model assumes no interactions except for an infinite potential repulsion on contact.

Table 3.5 Parameters used to fit the polydiserse Hard Sphere model to L300-based NIMs shown in Figure 3.14. R_g is the radius of gyration of the core and corona, R the geometric radius calculated using equation (2.18), and Δ is the polydispersity of the particles.

φ	R_{geff} (nm)	R_{eff} (nm)	Δ
0.056	8.37	10.8	0.144
0.130	8.26	10.7	0.140
0.192	8.26	10.7	0.134
0.293	7.03	10.4	0.137
0.375	8.17	10.5	0.140

scattering curves for M2070, L300, and EM C/25-based NIMs at select core concentrations along with both the Gaussian (solid lines) and PHS fits (dashed lines). As was noted in the previous sections, the Gaussian model does satisfactorily fit the scattering curves at the lowest core concentrations. For such large excesses of canopy molecules the particles do not "see" each other and will not experience interparticle interactions. The scattering pattern will only have contributions from the particle form factor which is due to the shape and size distribution of the core and corona components. As the core concentration increases, both models fail to fit the experimental data in the low q range where the scattering curve is dominated by interparticle interactions. The deviations begin at length scales consistent with the diameter of the cores, 18nm. Both models do capture the high q range for all samples studied, but as was stated earlier, this part of the curve is due to the shape and polydispersity of the core and corona. From all the fits, it was found that the average effective radius of the core and corona was $R_{core+corona}$ = 10.5nm, about 1.1nm larger than the original estimated effective radius calculated in the previous chapter. From the radius of the core obtained from both TEM and SAXS measurements (R_{core} = 8.9nm) this value suggests that the corona has a thickness of about δ_{corona} = 1.6nm,

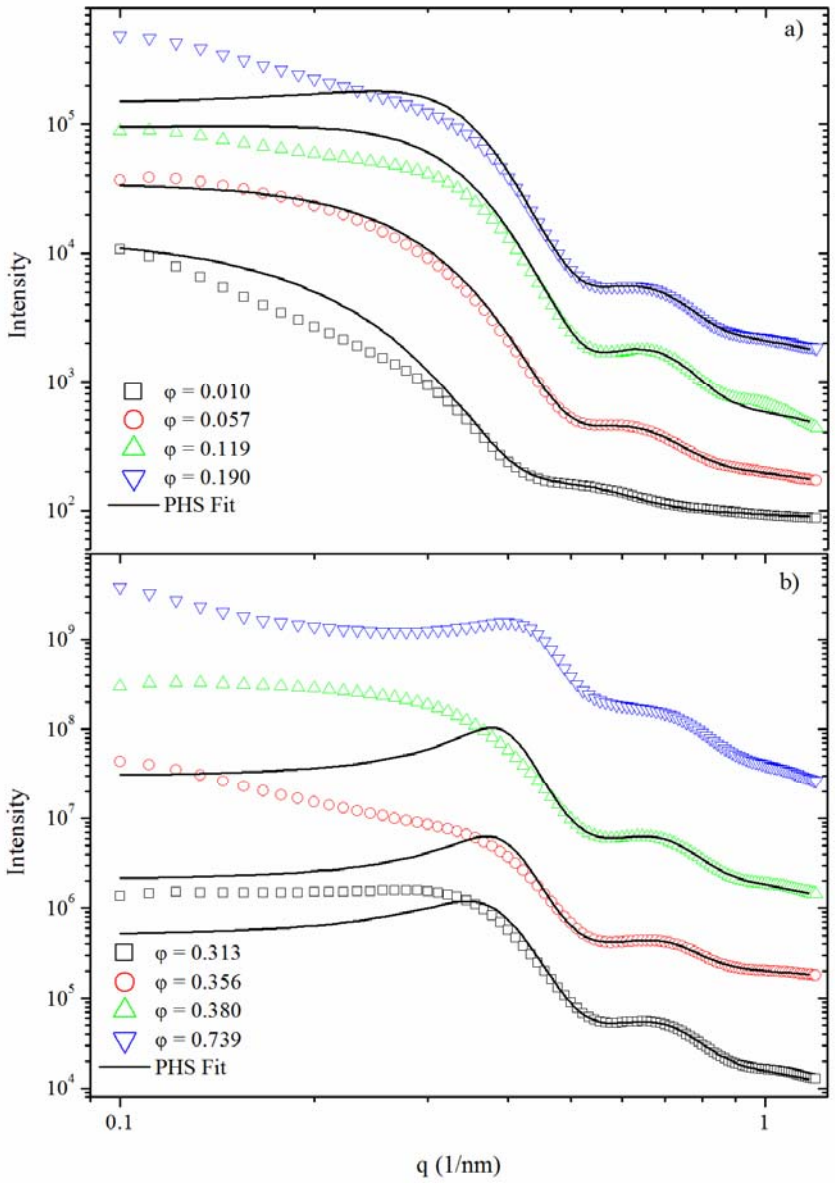

Figure 3.15 Plots of the scattered intensity for EM C/25-based NIMs. The lines are fits of a polydisperse hard sphere model based on the potential in equation (3.11). This model assumes no interactions except for an infinite potential repulsion on contact.

Table 3.6 Parameters used to fit the polydiserse Hard Sphere model to EM C/25-based NIMs shown in Figure 3.15. R_g is the radius of gyration of the core and corona, R the geometric radius calculated using equation (2.18), and Δ is the polydispersity of the particles.

φ	R_{geff} (nm)	R_{eff} (nm)	Δ
0.010	9.64	12.4	0.18
0.057	8.38	10.8	0.15
0.119	8.02	10. 4	0.14
0.190	8.06	10.4	0.15
0.313	7.83	10.1	0.15
0.356	7.82	10.1	0.14
0.380	7.86	10.1	0.15
0.604	7.65	9.9	0.178

about three times the original estimates based on the size of the corona molecule. The corona thickness can be estimated by measuring the average particle size through dynamic light scattering (DLS). Shown in Figure 3.19 are size measurements on core silica particles modified with the propyl silane corona. The three different batches (based on three different synthesis experiments to show the reproducibility of the surface funcationalization method) measured all gave similar effective core diameters of $d_{eff,DLS}$ = 19.6nm, which gives an average effective radius of $R_{eff,DLS}$ = 9.8nm. Since the core radius is 8.9nm, this effective DLS radius gives a corona thickness of $\delta_{corona,DLS}$ = 0.9nm, almost half of what is measured from the x-ray studies. It is difficult to get an accurate value for the corona thickness at such small length scales but it does seem safe to assume that the thickness of the corona layer may lie in the range between 0.5-1.6nm, a spread which may be due to polydispersity.

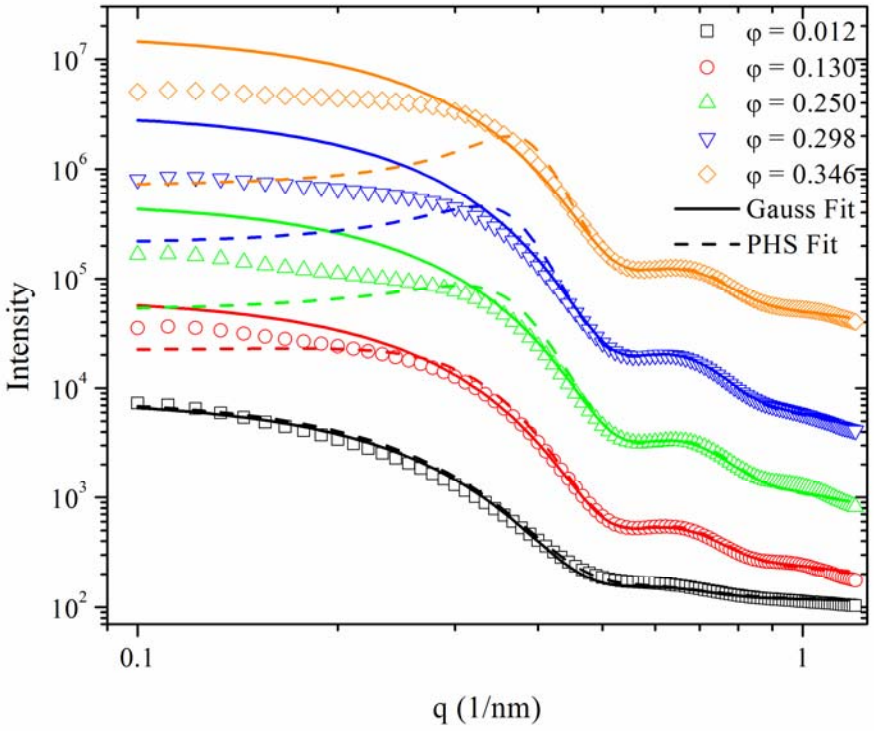

Figure 3.16 Plot of scattered intensity for M2070-based NIMs. Also plotted are fits of the Gaussian model (solid lines) and polydisperse Hard Sphere model (dashed lines).

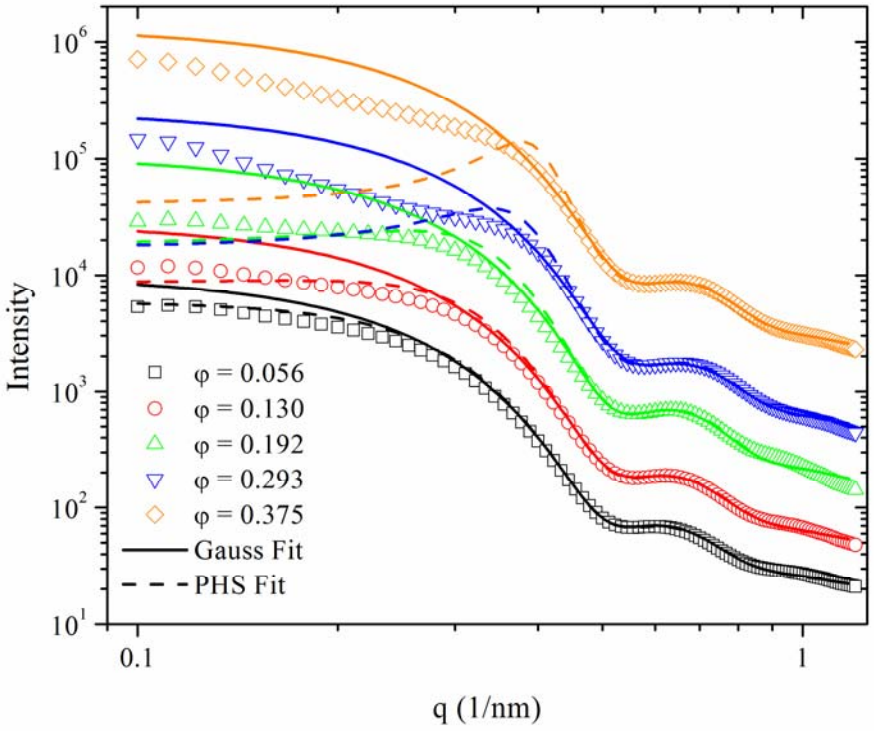

Figure 3.17 Plot of scattered intensity for L300-based NIMs. Also plotted are fits of the Gaussian model (solid lines) and polydisperse Hard Sphere model (dashed lines).

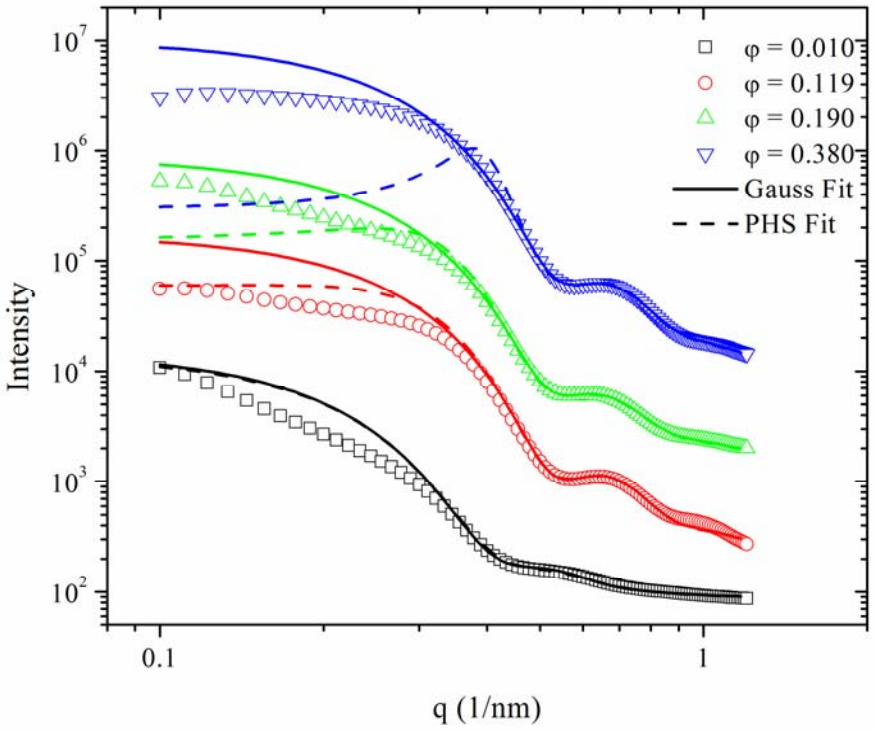

Figure 3.18 Plot of scattered intensity for EM C/25-based NIMs. Also plotted are fits of the Gaussian model (solid lines) and polydisperse Hard Sphere model (dashed lines).

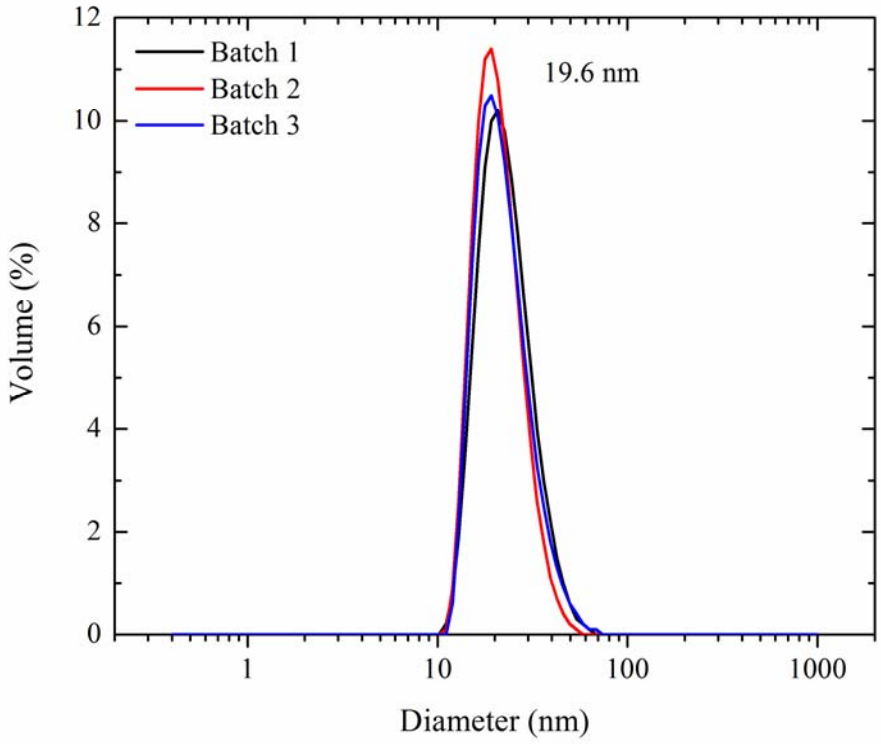

Figure 3.19 Dynamic light scattering results showing the effective diameter of core silica particles modified with the sulfonic acid corona. The particles have an average effective radius of $R_{eff,DLS}$ = 9.8nm.

Both models fail to fit the low q range scattering data for all samples from the semi-dilute up to the concentrated range. Since the Gaussian model does not take into account interactions between the particles, it just assumes that the shape of the curve will be that of a suspension of spheres. Increasing the core volume fraction that was input into the model only shifts the plot vertically and does not change the shape as can be seen from the fits. All the experimental data taken seem to have an intensity which falls below what the Gaussian model predicts. On the other hand, the second model which was fit to the scattering curves was that of a polydisperse suspension of particles with hard sphere interactions, where the interaction potential is given by equation (3.12) and assumes no interactions between the particles except upon contact where an infinite potential exists, preventing the particles from aggregating. This model was selected because it is one of the only colloid models which can be solved analytically and used to fit experimental data. From the plots (dashed lines), the PHS model underestimates the experimental data. Additionally, the PHS model predicts the appearance of structure factor peaks at the core concentrations studied, another feature which is not present in the NIMs systems. This indicates that the particles are not forming any detectable microstructure at the length scales probed in this study. It is noted that these length scales may be too short, being on the order of about ~ 60nm. Further experiments (such as USAXS and USANS) at longer length scales are required to fully probe the long-range order that may exists in NIMs. Nevertheless, at the length scales accessible from these measurements, NIMs do not appear to show any noticeable structure which can be used to fully explain the flow behavior of NIMs or extract viable structure factors because of the lack of a structure factor peak in the intensity data.

One curiosity though is where the experimental data lies with respect to the two models used in the fits. Upon closer inspection, the scattering results for NIMs

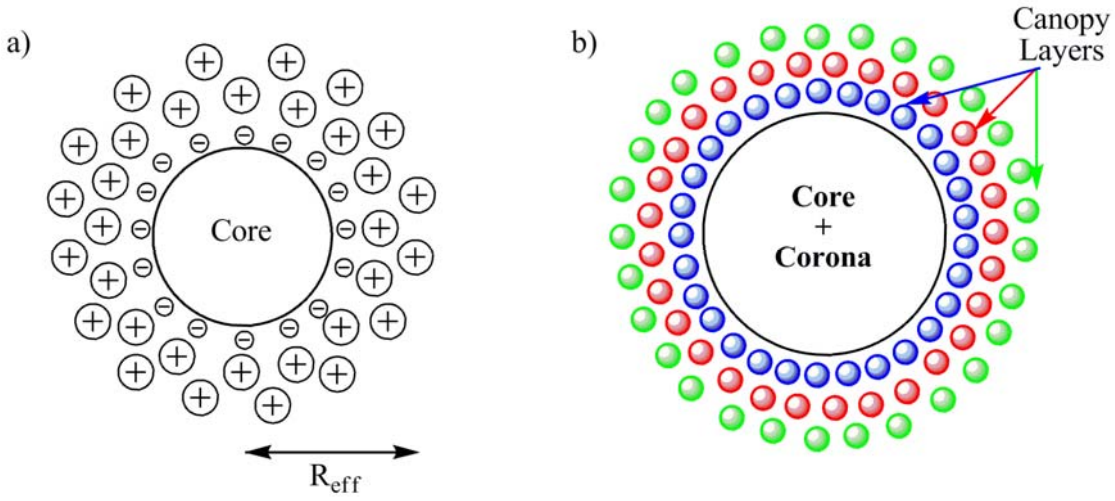

Figure 3.20 Working of model of NIMs unit. a) The canopy molecules can be thought of as spheres (positive symbols) surrounding the core and corona (negative symbols). b) Because of steric hindrances, the canopy molecules reside in layers around the core and corona, with the inner layers more strongly bound to the core.

fall right in the middle of what the two models predict. So the interactions that exist in NIMs are in between no interactions at all and no interactions until contact. Based on the rheological characterization presented, a working model of what the NIMs unit consists of was presented. This model was based on an analysis of the reduced viscosity of NIMs using the Krieger-Dougherty equation. This model is again presented in Figure 3.20 and shows that, based on experimental evidence, the NIMs unit consists of the core, corona, and an inner layer of canopy molecules which are strongly bound to the corona. This inner layer travels along with the core and corona during flow and the outer layers, which are more weakly bound, are free to diffuse from particle to particle. A recent study by Jespersen et. al. did in fact find that the canopy molecules are quite mobile, and can hop from core to core [46]. Figure 3.21 is a schematic representation of what is believed to be happening in the NIMs state. As the core particles approach each other, it is very possible for one of the outer canopy molecules to "hop" from a core to a neighboring core. The interactions between the core particles seem to be dominated by this hopping mechanism of the canopy

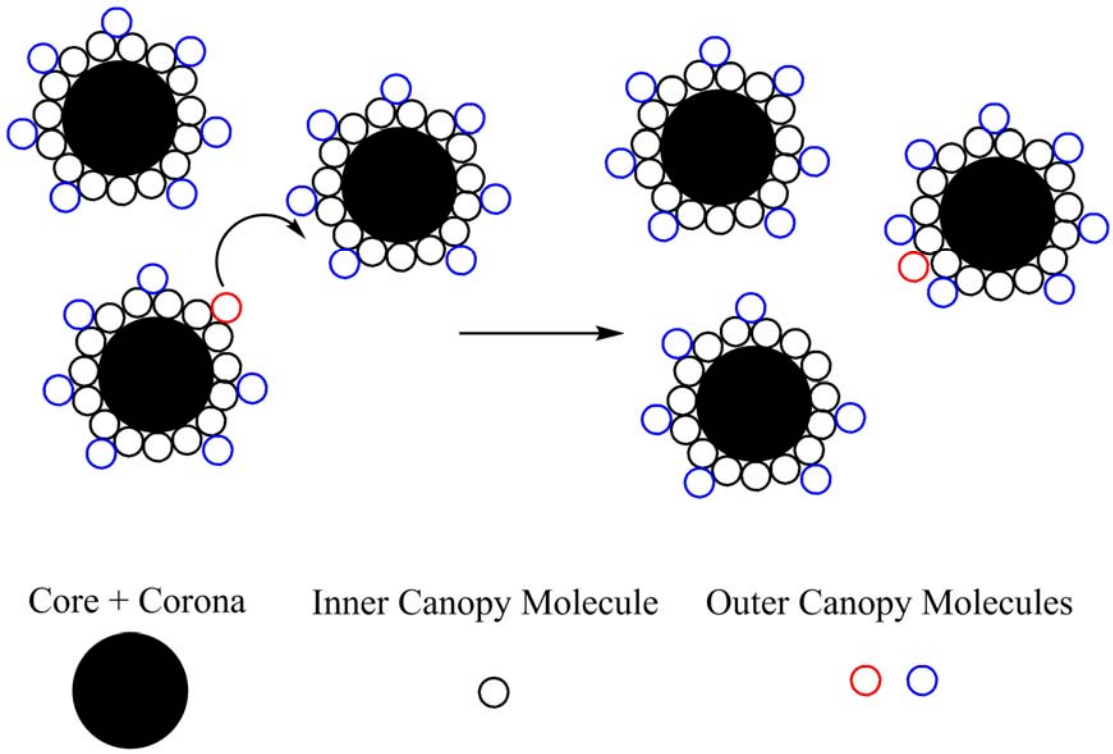

Figure 3.21 "Hopping" model for outer canopy molecules on NIMs unit. The solid spheres are meant to represent the core and corona, the black circles the inner canopy molecules, and the blue circles the weaker bound canopy molecules. In this diagram we show, using a red colored circle how an outer canopy molecule can "hop" from one core to another.

molecules. One could argue that this is the reason why all the scattering curves for NIMs systems seem to have the appearance of a dilute suspension of spheres, and why most of the samples show very Newtonian rheology. Since there is no core microstructure forming at the length scales studied, then one should expect Newtonian rheology, which is what was shown in Chapter 2. The reason for the viscosity increases may then be due to the thinning of the outer layer of canopy molecules. A simplified picture of NIMs may then consist of the inner core, corona, and canopy, surrounded by an outer layer of canopy molecules which may have the function of grease which helps the particles slide past one another without having to come into close contact. The original picture of NIMs carrying their own suspending medium still applies with this picture, but the suspending medium now needs to be considered as a dynamic medium with very complex behavior that determines the overall properties of NIMs. In essence, different NIMs units communicate with each other through the exchange of their outer canopy layers and it is possible that the size, shape, and chemistry of the canopy molecules will be the dominant factor controlling the rheological properties of NIMs.

Conclusion

In this chapter small-angle x-ray scattering studies of NIMs were presented. All scattering data was analyzed using known theories that have been successfully applied to describe colloidal particles which lie on two opposite extremes: no interparticle interactions (Gaussian Spheres) and hard sphere interactions (polydisperse Hard Spheres). During an analysis of the scattering curves it was found that the effective size of the scattering particle was larger than anticipated. This was due to the fact that the scattering length difference between the core and corona is so small that the two cannot be distinguished by x-rays. All the scattering patterns had

very similar shapes which appear just like those for dilute dispersions of spheres, even up to volume fractions of $\varphi = 0.19$. No microstructure was observed in any of the patterns indicating that it does not seem to be a significant parameter which controls NIMs rheology. Using Gaussian and polydisperse hard sphere models, only the high q range of the scattering curves were satisfactorily fit since at this range the curve is determined by shape and size distribution of the particles. The Gaussian model overestimates the data at the low q range, while the PHS model underestimates it at this same range. Surprisingly, the experimental data falls right in between what these two models predict indicating that the interactions between the cores in NIMs fall somewhere in the range between these two extremes.

Based on these observations, the rheological data in Chapter 2, and recent experiments by the Air Force Research Lab, a working model of NIMs was presented. It is found that the NIMs unit consists of the core, corona, and an inner layer of tightly bound canopy molecules. The strength of attraction between the corona and outer canopy molecules are then not as strong as that between the inner canopy molecules and corona. This allows for the outer canopy molecules to be quite mobile, "hopping" from core to core as was observed in recent NMR studies. The NIMs unit can be considered as the inner core, corona, and canopy molecules surrounded by weakly associated canopy molecules. These weakly associated canopies behave as a dynamic "grease", which travels with the NIMs unit and helps lubricate its motion. As the "grease" layers gets smaller, the core particles cannot slide past each other as easily, leading the dramatic viscosity increases reported in Chapter 2. The main interactions in NIMs are therefore dominated by this dynamic canopy motion, where the direct interparticle interactions do not seem to have a significant effect. This means it is not correct to try and categorize NIMs dynamics into any understood system and require further investigation to fully uncover their behavior.

REFERENCES

[1] B. J. Ackerson, N. A. Clark, *Phys. Rev. A* **1984**, *30*, 906.

[2] B. J. Ackerson, J. B. Hayter, N. A. Clark, L. Cotter, *J Chem Phys* **1986**, *84*, 2344.

[3] B. J. Ackerson, P. N. Pusey, *Phys Rev Lett* **1988**, *61*, 1033.

[4] Z. Adamczyk, B. Jachimska, M. Kolasinska, *J Colloid Interf Sci* **2004**, *273*, 668.

[5] N. W. Ashcroft, J. Lekner, *Phys Rev* **1966**, *145*, 83.

[6] M. Ballauff, *Curr Opin Colloid In* **2001**, *6*, 132.

[7] J. F. Brady, J. F. Morris, *J Fluid Mech* **1997**, *348*, 103.

[8] L. B. Chen, C. F. Zukoski, B. J. Ackerson, H. J. M. Hanley, G. C. Straty, J. Barker, C. J. Glinka, *Phys Rev Lett* **1992**, *69*, 688.

[9] M. Chen, W. B. Russel, *J Colloid Interf Sci* **1991**, *141*, 564.

[10] U. Gasser, E. R. Weeks, A. Schofield, P. N. Pusey, D. A. Weitz, *Science* **2001**, *292*, 258.

[11] W. L. Griffith, R. Triolo, A. L. Compere, *Phys. Rev. A* **1987**, *35*, 2200.

[12] M. D. Haw, W. C. K. Poon, P. N. Pusey, *Phys Rev E* **1998**, *57*, 6859.

[13] E. W. Kaler, *Modern Aspects of Small-Angle Scattering*, Kluwer Academic, Boston **1993**.

[14] W. K. Kegel, A. van Blaaderen, *Science* **2000**, *287*, 290.

[15] S. R. Kline, *J. Appl. Crystallogr.* **2006**, *39*, 895.

[16] H. M. Laun, R. Bung, S. Hess, W. Loose, O. Hess, K. Hahn, E. Hadicke, R. Hingmann, F. Schmidt, P. Lindner, *J Rheol* **1992**, *36*, 743.

[17] D. A. McQuarrie, *Statistical Mechanics*, Harper & Row, New York **1975**.

[18] M. Megens, C. M. vanKats, P. Bosecke, W. L. Vos, *Langmuir* **1997**, *13*, 6120.

[19] J. Moonen, C. Dekruif, A. Vrij, *Colloid Polym Sci* **1988**, *266*, 1068.

[20] J. Moonen, A. Vrij, *Colloid Polym Sci* **1988**, *266*, 1140.

[21] R. H. Ottewill, A. R. Rennie, G. D. W. Johnson, *Adv Colloid Interfac* **2003**, *100*, 585.

[22] R. H. Ottewill, R. A. Richardson, *Colloid Polym Sci* **1982**, *260*, 708.

[23] D. Pontoni, S. Finet, T. Narayanan, A. R. Rennie, *J Chem Phys* **2003**, *119*, 6157.

[24] W. Poon, *Science* **2004**, *304*, 830.

[25] P. N. Pusey, P. N. Segre, O. P. Behrend, S. P. Meeker, W. C. K. Poon, *Physica A* **1997**, *235*, 1.

[26] D. Qiu, T. Cosgrove, A. M. Howe, *Langmuir* **2006**, *22*, 6060.

[27] D. Qiu, T. Cosgrove, A. M. Howe, U. A. Dreiss, *Langmuir* **2006**, *22*, 546.

[28] D. Qiu, C. A. Dreiss, T. Cosgrove, A. M. Howe, *Langmuir* **2005**, *21*, 9964.

[29] S. K. Rhodes, J. A. Lewis, *J Am Ceram Soc* **2006**, *89*, 1840.

[30] D. O. Riese, G. H. Wegdam, W. L. Vos, R. Sprik, D. Fenistein, J. H. H. Bongaerts, G. Grubel, *Phys Rev Lett* **2000**, *85*, 5460.

[31] A. Sierou, J. F. Brady, *J Rheol* **2002**, *46*, 1031.

[32] E. B. Sirota, H. D. Ouyang, S. K. Sinha, P. M. Chaikin, J. D. Axe, Y. Fujii, *Phys Rev Lett* **1989**, *62*, 1524.

[33] P. Vanbeurten, A. Vrij, *J Chem Phys* **1981**, *74*, 2744.

[34] A. Vanblaaderen, P. Wiltzius, *Science* **1995**, *270*, 1177.

[35] W. Vanmegen, P. N. Pusey, *Phys. Rev. A* **1991**, *43*, 5429.

[36] N. J. Wagner, R. Krause, A. R. Rennie, B. D'Aguanno, J. Goodwin, *The Journal of Chemical Physics* **1991**, *95*, 494.

[37] A. Weiss, N. Dingenouts, M. Ballauff, H. Senff, W. Richtering, *Langmuir* **1998**, *14*, 5083.

[38] M. Zackrisson, A. Stradner, P. Schurtenberger, J. Bergenholtz, *Langmuir* **2005**, *21*, 10835.

[39] M. Zackrisson, A. Stradner, P. Schurtenberger, J. Bergenholtz, *Phys Rev E* **2006**, *73*, 8.

[40] *Neutron, X-Ray, and Light Scattering: Introduction to an Investigative Tool for Colloidal and Polymeric Systems*, North-Holland, New York **1991**.

[41] L. A. Feigin, D. I. Svergun, *Structure Analysis by Small-Angle X-Ray and Neutron Scattering*, Plenum Press, New York **1986**.

[42] P. C. Hiemenz, R. Rajagopalan, *Principles of colloid and surface chemistry*, Marcel Dekker, Inc, New York **1997**.

[43] C. G. Dekruif, W. J. Briels, R. P. May, A. Vrij, *Langmuir* **1988**, *4*, 668.

[44] J. P. Hansen, I. R. McDonald, *Theory of Simple Liquids*, Academic Press, New York **2006**.

[45] J. K. Percus, G. J. Yevick, *Physical Review* **1958**, *110*, 1.

[46] M. L. Jespersen, P. A. Mirau, E. vonMeerwall, R. Rodriguez, E. P. Giannelis, R. A. Vaia, *ACS Nano* **2009 (In Preparation)**.